Chapter 4

Gas-Phase Organic Oxidation Chemistry and Atmospheric Particles

Neil M. Donahue*, Wayne Chuang and Meredith Schervish
Departments of Chemistry,
Chemical Engineering, Engineering and Public Policy,
and Center for Atmospheric Particle Studies
Carnegie Mellon University
Pittsburgh, PA 15213, USA
**nmd@cmu.edu*

Organic aerosols comprise a rich mixture of compounds, many generated via nonselective radical oxidation. This produces a plethora of products, most unidentified, and mechanistic understanding has improved with instrumentation. Recent advances include recognition that some peroxy radicals undergo internal H-atom transfer reactions to produce highly oxygenated molecules and recognition that gas-phase association reactions can form higher molecular weight products capable of nucleation under atmospheric conditions. Particles also range from molecular clusters near 1 nm diameter containing a few molecules to coarse particles above 1 μm containing 1 billion or more molecules. A mixture of organics often drives growth of particles. We can describe this via detailed thermodynamics, and we can also describe the physics driving mixing between separate populations containing semi-volatile organics. Finally, fully size-resolved particle microphysics enables detailed comparisons between theory and observations in chamber experiments.

4.1. Introduction

Atmospheric fine particles have outsized effects on climate and human health. A particle mass concentration of $1\,\mu\mathrm{g\,m^{-3}}$ is a mass fraction of roughly 10 ppb, given that a standard cubic meter of air weighs roughly 1 kg. Furthermore, if a typical molar mass of (organic) constituents in the particle is 300 g/mole, the 10 ppb mass fraction corresponds to a mole fraction of about 1 ppb in air. In spite of this low concentration, particles represent a key uncertainty in climate forcing[1] and leading to premature deaths of roughly 4 million people worldwide each year.[2] The concentrated effect of being in a condensed phase greatly amplifies the effects of fine particles; for health effects, it focuses the dosage of toxicants on deposition sites in the lung, and for climate, it forms objects with sufficient size to directly scatter light and to influence the partial pressure of water during cloud droplet formation and thus to act as cloud condensation nuclei.

A 100-nm diameter particle comprising organic compounds with an average molar mass of 300 g/mole contains about 1.5 million molecules if its overall density is 1400 $\mathrm{kg/m^3}$. Under most circumstances in the atmosphere, the average oxygen to carbon ratio (O:C) of those compounds is roughly 0.8:1.[3,4] Recent discoveries addressed later in this article demonstrate that most of these molecules have never been synthesized.[5–7] The 100-nm particle probably contains several hundred thousand individual organic species, meaning that the most abundant species might constitute 100 or so of those 1.5 million molecules.[8,9] Organic particles are thus a quintessentially complex mixture; there is almost no chance that a given molecule will encounter another copy of itself while in the condensed phase.

The great diversity of compounds in the condensed phase, combined with the relative paucity of specifically identified molecules, motivated us to define a physiochemical space combining volatility (the tendency to be in the gas phase) with O:C (the degree of oxygenation, or alternately the carbon oxidation state, $\overline{\mathrm{OS}}_{\mathrm{C}}$). This is known as the volatility basis set (VBS), and it comes in two essential forms: a one-dimensional VBS (1D-VBS) tracking only volatility,[10–12] and a two-dimensional VBS (2D-VBS) tracking both volatility and oxidation.[13–17]

The concept of the VBS is to provide a framework defined by key properties (volatility and degree of oxidation — broadly thermodynamics and chemistry) that can inform the evolution of all compounds known and unknown within the framework, and thus the behavior and evolution of organic aerosols. By using volatility as the principal independent variable, the VBS focuses on the behavior of the organic material rather than the exact composition. However, the composition is obviously of interest, known compounds can be precisely located in the space, and the evolution of material from one location in the space to another as a result of chemical reactions can be informed by known chemical behavior, along with group-additivity or structure–activity relationships.

The original formulations of the VBS focused on equilibrium phase partitioning with respect to a bulk condensed phase (i.e., the bulk mass concentration of organic aerosol in an air volume, $\mu\text{g}\,\text{m}^{-3}$).[11,13] In addition, chemical reactions have been described for the most part as generational steps from one stable species to the next, in the form of "oxidation kernels" transforming a species from a reactant location ("bin") in the space to a distribution of product locations.[11,15,17,18] These implementations did not address particle dynamics (nucleation, size-dependent growth, etc.) nor did they explicitly address radical branching chemistry other than to allow the oxidation kernels to serve as normalized basis vectors that could be mixed by, e.g., modeled or inferred RO_2 branching chemistry that might be called "low–NOx" or "high–NOx".[19,20] More recently, we have begun to address particle microphysics for monodisperse particle populations.[17,21–23]

The standard VBS classifies organic compounds by their saturation concentration, C^{o}, in $\mu\text{g}\,\text{m}^{-3}$ and typically discretizes this space in volatility bins that are decadally spaced in a logarithmic space (one $\log_{10}$ unit) at a reference temperature (typically 300 K).[11] These bins (and their contents) then shift as temperature changes depending on their enthalpy of vaporization ($\Delta\,\text{H}_v$), which is in turn a function of (really the driver of) the volatility.[24] For $C^{\text{o}}(300) = \mu\text{g}\,\text{m}^{-3}$, a temperature change of 15–20 K will shift the bin by one decade.[13,24] For nonideal solutions, the activity coefficient can be incorporated into the empirical volatility, which is then identified as C^*.

We can also describe broad volatility classes based on behavior. The volatile organic compounds (VOCs) are the vast majority (by concentration) of organics in the atmosphere and reside almost entirely in the gas phase (the exception being highly water-soluble compounds). Intermediate volatility organic compounds (IVOCs) are much less volatile than VOCs, yet still reside largely in the gas phase under ambient conditions. Semi-volatile organic compounds (SVOCs) have significant mass fractions in both the gas and condensed phases under ambient conditions. Low-volatility organic compounds (LVOCs) reside largely in the condensed phase yet their vapor pressure matters to their behavior — for example, with a small fraction in the gas phase being subject to rapid oxidation chemistry[16] or suppressed condensation to the smallest particles due to the Kelvin (surface tension) effect.[23] Lastly, extremely low-volatility organic compounds (ELVOCs) will stay on essentially any condensed-phase surface they encounter, including the very smallest particles. We may need to invoke one final category, ultra low-volatility organic compounds (ULVOCs), which would be compounds that almost always stick to each other and thus drive new-particle formation.

While we have presented volatility ranges for these classes, generally spanning three to four decades in saturation concentration,[14,25,26] the definitions are more based on qualitative behavior. For example, SVOCs should have a saturation concentration within about one order of magnitude of the local organic aerosol concentration (C_{OA}), including temperature effects, so SVOCs in the planetary boundary layer might be quite different from SVOCs in the upper troposphere. Further, the putative ULVOCs would really depend on typical saturation ratios, which in turn would be governed by a balance of gas-phase production and condensational loss.[27] However, the shaded regions in most of the 2D-VBS figures below will show the limits of the typical ranges.

4.2. The Volatility Basis Set

To improve the integration of the VBS with gas-phase chemical oxidation mechanisms, we are developing a more explicit representation of radical branching chemistry. A specific motivation is to treat autooxidation chemistry,[6,7,28,29] but in general, our objective is to allow for more general radical propagation and termination and so provide a more realistic underpinning to VBS oxidation mechanisms. This has received most attention for oxidation of terpenes, and in this work we shall use the canonical system of α-pinene oxidation as the model. There is strong evidence that while most of the oxidation products from α-pinene oxidation follow the traditional oxidation sequence, with RO_2 reacting largely with NO or HO_2, or perhaps with other RO_2 to form either radical ($RO+RO+O_2$) or molecular ($ROH+R{=}O+O_2$) products,[30] an important subset of the RO_2 engages in unimolecular autooxidation,[7,28] and further, some of the RO_2 self-reaction products consist of peroxide dimers ($ROOR+O_2$).[7,28]

The previous incarnation of the VBS described formation of products via a set of stoichiometric carbon-yield "kernels", such as yields, y, for α-pinene ozonolysis:

$$\alpha\text{-pinene} + O_3 \rightarrow \{y^{\,\mathrm{low}-NO_x}\} \tag{4.1}$$

$$\alpha\text{-pinene} + O_3 \rightarrow \{y^{\mathrm{high}-\mathrm{NO_x}}\} \tag{4.2}$$

Where $\sum_i y^{\,\mathrm{low}-NO_x} = 1$, and production at intermediate NO_x was given by $\{y\} = \beta\{y^{\mathrm{high}-NO_x}\} + (1-\beta)\{y^{\mathrm{low}-NO_x}\}$, where β is roughly the fraction of RO_2 loss via RO_2 + NO (which can be estimated based on VOC:NO_x).[19]

We shall now describe the same process as a reaction sequence involving surrogate radical species:

$$\alpha\text{-pinene} + O_3 \rightarrow RO_2 \tag{4.3}$$

$$\rightarrow \mathrm{SVOC} \tag{4.4}$$

$$RO_2 + X \rightarrow \mathrm{SVOC} \tag{4.5}$$

$$RO_2 \rightarrow (\mathrm{Ox})_1RO_2 \tag{4.6}$$

$$(O_x)_1RO_2 \rightarrow (O_x)_2RO_2 \tag{4.7}$$

$$(O_x)_2RO_2 \rightarrow (O_x)_3RO_2 \tag{4.8}$$

$$(O_x)_nRO_2 \rightarrow \mathrm{LVOC} \tag{4.9}$$

$$(O_x)_nRO_2 + X \rightarrow \mathrm{LVOC} \tag{4.10}$$

$$(O_x)_nRO_2 + (O_x)_nRO_2 \rightarrow \mathrm{ELVOC} \tag{4.11}$$

$$\mathrm{SVOC} \xrightarrow{\mathrm{het}} \text{oligomer} \tag{4.12}$$

After the initiation Reaction 4.3 we include branching to molecular products such as pinonic acid and pinonaldehyde via Reaction 4.4 (i.e., via Criegee Intermediate stabilization[31,32]) and radical propagation through an initial RO_2 (possibly several) via Reaction 4.3. Subsequent reactions include radical termination and propagation steps, which we shall discuss in more detail below; however, the ansatz is that we can split this termination into three broad categories: more or less "traditional" termination with first-generation products containing one or two oxygenated functional groups; autooxidation followed by the same traditional termination; and, autooxidation followed by gas-phase association reactions (i.e., to ROOR). These processes are in competition and govern the product volatility distribution. Autooxidation is thought to be possible for only a (small) fraction of peroxy radicals[33]; it adds functional groups but still requires termination because it regenerates the peroxy moiety. Termination via association will effectively double the molecular weight of the products. The temperature dependence of the competition is especially interesting because the competition between autooxidation and termination pits a unimolecular process against bimolecular processes, almost certainly with very different activation energies.

Our goal is to represent the branching and termination processes within the VBS to capture these effects. Figure 4.1 shows a nominal carbon yield distribution from α-pinene ozonolysis separating the three categories. Here the traditional chemistry occurs 90% of the time, shown in green; termination to monomer products following autooxidation occurs 7% of the time, shown in salmon red; and termination to association products occurs 3% of the time, shown in gray. Each distribution is individually normalized and so we can easily account for the various subyields and add them.

It is very important to keep track of carbon yields (molar yield of each species multiplied by $n_C/10$ for the empirical formula $C_{10}H_{16}$) so that we can be sure that our full distribution conserves carbon. However, what we really need to know for VBS and microphysics calculations is the total condensing mass concentration, and thus mass yields, so the carbon yields need to be multiplied by the organic

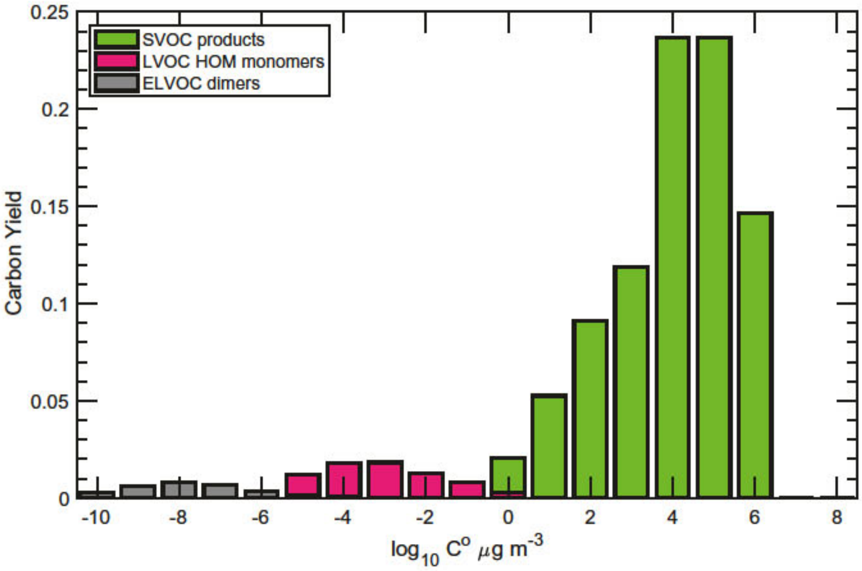

Fig. 4.1 One-dimensional representation of carbon yields from α-pinene + ozone in three broad classes of products: semi-volatile "traditional" oxidation products (green); low-volatility "autooxidation" products (salmon); and extremely low-volatility products from autooxidation followed by peroxy radical association (gray).

mass to organic carbon ratio (OM:OC) for each species (or bin). We scale the carbon yields in Fig. 4.1 by OM:OC (normalized to the OM:OC for α-pinene) to give mass yields shown in Fig. 4.2. The lower volatility products are somewhat enhanced because they are heavier, and the total sum is well over 1.0.

The distributions in Figs. 4.1 and 4.2 combine insight from traditional SOA mass yield experiments[19,34,35] with recent experiments revealing the importance of autooxidation to SOA formation[7] as well as new-particle formation and growth.[23,28] It is not obvious that a single product volatility distribution can simultaneously explain these results,[26] and so we anticipate the possibility that different chemical conditions (and perhaps different microphysics in the form of very different growth rates) may explain apparent contradictions in the experimental results.

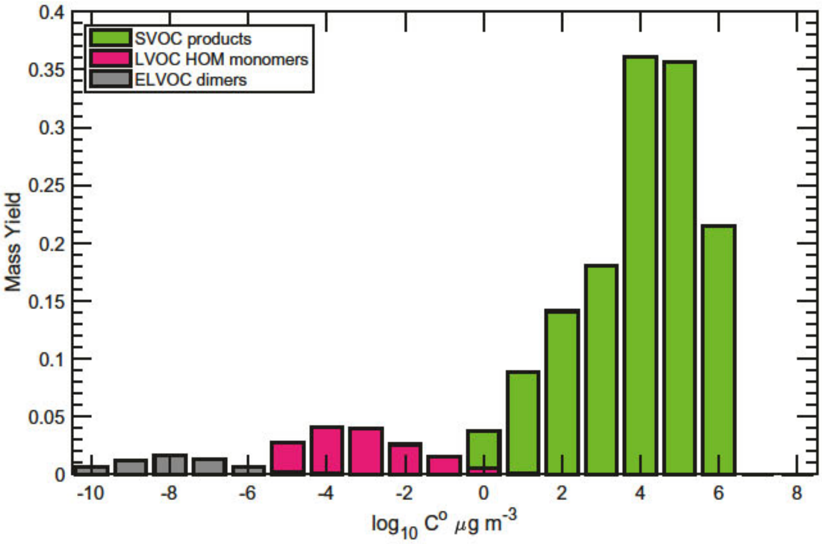

Fig. 4.2 One-dimensional representation of mass yields for same distribution as Fig. 4.1.

The 2D-VBS permits explicit calculation of OM:OC as well as provides a framework to describe multiple generations of oxidation where the specific chemical structures of the numerous products are unknown. The VBS does not require any specific knowledge about chemical structure, because the independent variables are the properties required to carry out microphysical calculations and compare with bulk observations (volatility and C:H:O). However, many observations constrain the composition of species (i.e., n_C, n_H, n_O) and also kernels for oxidation and aging can be informed by iso-lines of constant composition (i.e., C_{10}). The 2D-VBS can be paired with a simple composition–activity relationship relating volatility to composition[13] when there is a typical average composition of polar moieties in oxidized molecules. The original version is based on the assumption that oxidized organics in the atmosphere contain, on average, equal numbers of –OH and =O functional groups (including acid groups, which are one of each) and that these have a log-linear effect on volatility. In its simplest form, this can be reduced to a set of pairwise interaction terms (b_C and b_O between nonpolar groups

(–C–) and polar groups (–OH + =O), along with a reference carbon number, $n_{\mathrm{C}}^{\mathrm{o}}$, for species with $C^{\mathrm{o}} = 1\,\mu\mathrm{g\,m}^3$:

$$\log_{10} C^{\mathrm{o}} = (n_{\mathrm{C}}^{\mathrm{o}} - n_{\mathrm{C}})\, b_{\mathrm{C}} - n_{\mathrm{O}}\, b_{\mathrm{O}} - 2\,\frac{n_C\, n_O}{n_C + n_O}\, b_{\mathrm{CO}} \qquad (4.13)$$

The cross term b_{CO} describes nonideality (the excess free energy) favoring polar–polar interactions and accurately predicts e.g., the volatility of diacids.[36] The original values of the parameters are the following:

1. the carbon–carbon interaction term ($b_{\mathrm{C}} \simeq 0.475$),
2. the oxygen–oxygen interaction term ($b_{\mathrm{O}} \simeq 2.3$),
3. the carbon-oxygen nonideality ($b_{\mathrm{CO}} \simeq -0.3$), and
4. the carbon number of a $1\,\mu\mathrm{g\,m}^{-3}$ alkane ($n_{\mathrm{C}}^{\mathrm{o}} \simeq 25$).

With these parameters, oxygenation dramatically decreases volatility and, because "like attracts like", this rate of decrease gets higher with greater oxygenation (the carbon isolines curve over). Consequently, a C_{10} organic with O:C = 1 would have $C^{\mathrm{o}} \simeq 10^{-5}\,\mu\mathrm{gm}^{-3}$, in the ELVOC range.[13]

The original 2D-VBS composition-activity parameters predate the discovery that autooxidation controls formation of highly oxygenated molecules (HOMs) by adding a succession of peroxide functional groups (–OOH) to the carbon backbone.[7] HOMs are operationally defined as organic compounds formed via gas-phase peroxy radical autooxidation with six or more oxygen atoms. The extra oxygen in the HOM peroxides does little to lower volatility,[37] and furthermore, the relatively flexible functional groups enhance internal hydrogen bonding in the gas-phase monomer, which lowers the energetic advantage of being in the condensed phase and thus increases the saturation concentration.[36,38] For both of these reasons, the HOMs have much higher saturation concentrations than the original VBS composition–activity relationship would suggest.[23,38]

Shown in Fig. 4.3(top) is a 2D-VBS composition space with revised parameters giving contours that broadly agree with inferred

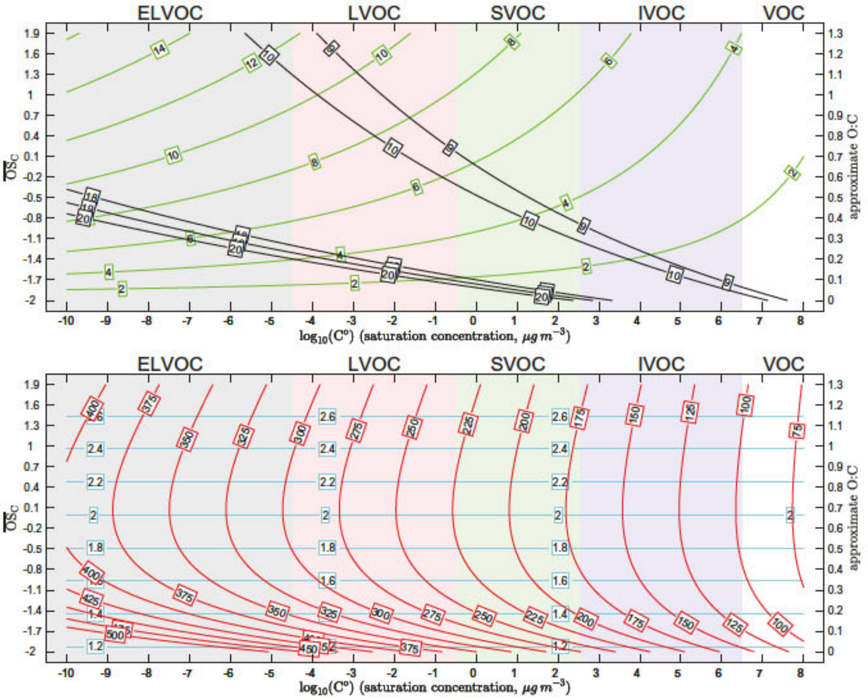

Fig. 4.3 Two-dimensional VBS with (top) carbon number (black) and oxygen number (green) isopleths and (bottom) molecular weight (red) and OM:OC (cyan). The y-axis is shown for both the average oxidation state of carbon ($\overline{OS}_{\mathrm{C}} = 2\mathrm{O}:\mathrm{C} - \mathrm{H}:\mathrm{C}$) and approximate O:C. Carbon number isopleths are relevant to oxidation of monoterpene (C_{10}) precursors, with predominant –OH functionality at low O:C giving way to –OOH functionality at higher O:C.

volatilities in Tröstl *et al.*[23] Specifically, we use "HOM" parameters for Eq. (4.13) of

1. a HOM oxygen–oxygen term ($b_{\mathrm{O}} \simeq 0.2$), and
2. a HOM carbon–oxygen nonideality ($b_{\mathrm{CO}} \simeq +0.9$).

These terms are empirical, but they describe a situation where –OH functionality dominates at low O:C (with some =O) but –OOH dominates at higher O:C (again with some =O). The parameters mean that added oxygen drops C^{o} by two decades at O:C = 0 but this falls off to just over one decade for O:C = 1. The positive nonideality would imply a negative excess free energy and thus negative activity coefficients in nonideal mixtures; this is almost certainly not physical and so the parameters should not be used to calculate activity coefficients.

The domain and range of Fig. 4.3 extend to lower C^{o} and higher O:C than earlier representations.[13,14] This is because the ELVOC range is significant to new-particle formation and the autooxidation process leads to higher degrees of oxygenation than originally anticipated. It is also important to note that the effective average oxidation state of carbon, $\overline{\mathrm{OS}}_{\mathrm{C}} = 2\mathrm{O{:}C} - \mathrm{H{:}C}$[9] is empirically defined as such (and remains usefully invariant upon dehydration of molecules). The "extra" oxygens in the –OOH functional groups do not oxidize carbon.

The net effect of the HOM parameters is that the carbon isopleths curve sharply upward instead of somewhat downward as oxygenation increases. The added functional groups are far less effective at reducing volatility than suggested by the original parameters, and thus HOMs are not necessarily ELVOCs. Figure 4.3 shows carbon isopleths near C_{10} and C_{20} to emphasize that the C_{10} products from monoterpene oxidation barely reach the ELVOC range even with 12 added oxygen atoms (though the range of volatility for probable $C_{10}O_{12}H_{12,14,16}$ structures is likely to be wide). It is unlikely that atmospheric processes would generate these LVOC products at a rate sufficient to form supersaturations leading to nucleation, though they could contribute to particle growth.[23] However, the C_{20} association products ("dimers") are much more likely candidates to participate in nucleation.[28]

As mentioned above, it is important to realize that composition $(n_{\mathrm{C}}, n_{\mathrm{O}}, n_{\mathrm{H}})$ is only a matter of interest in the 2D-VBS where the independent variables are C^{o} and O:C. This applies to the molecular weight of species in the 2D space as well — the VBS tracks carbon mass, and is less concerned with how many molecules comprise that carbon. To emphasize that, Fig. 4.3 (bottom) shows the molecular weight but also OM:OC in the 2D-VBS with the HOM parameters. While the molecular weight changes dramatically in the lower left-hand corner, OM:OC is (strictly in this case) only dependent on O:C.

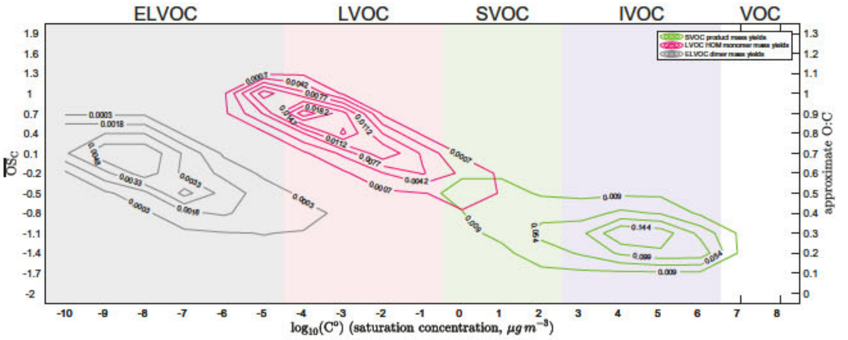

Fig. 4.4 Mass yields from α-pinene ozonolysis shown in Fig. 4.2 in the 2D-VBS. Autooxidation produces a tail of highly oxygenated molecules (HOMs) stretching to low volatility and hight O:C (red contours), while dimerization reactions produce a parallel tail with lower volatility (gray contours).

In reality, H:C is not a perfect function of O:C, but H is so light that this barely matters. Consequently, as long as we know carbon yields and OM:OC, the VBS will reliably track condensible carbon and organic mass.

With the 2D space in place, the mass yields from Tröstl *et al.* look something like those shown in Fig. 4.4. When these are added up along the columns (all O:C at constant C^o) they give the mass yields shown in Fig. 4.2. This reveals the chemical organization behind the observed products, and again the overall yields conserve carbon. First, the majority of products resolve along "traditional" lines shown with the green contours, via which ozonolysis generates products with volatilities between one and six orders of magnitude lower than the precursor (α-pinene) and with one to four added oxygens. These are the SVOC products with green contours. Second, a tail toward lower volatility and higher O:C is at least partly due to a small but nontrivial fraction of products that have undergone autooxidation to rapidly add significant oxygenated functionality with lowered volatility.[26] These are the LVOC HOM monomer products with reddish contours. Third, some products emerge with twice the carbon number and high O:C that is however lower than the O:C on average in the LVOC tail. These are the ELVOC dimer products with gray contours.

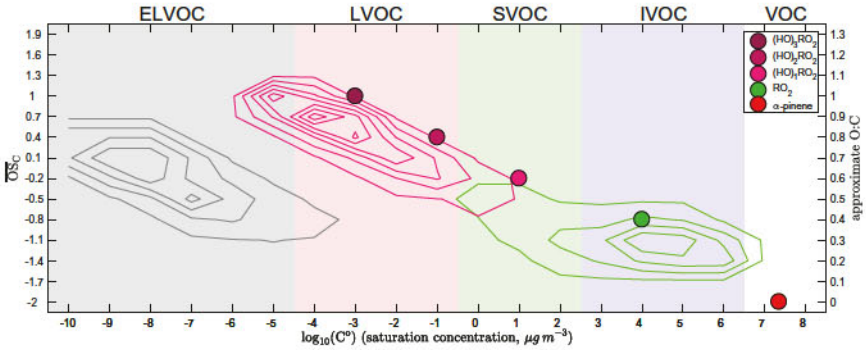

Fig. 4.5 Peroxy radicals important to α-pinene VBS products including an autooxidation sequence. Autooxidation produces a sequence of progressively more oxidized RO_2 radicals that resolve into molecular products.

4.2.1. *Mechanistic Representation*

Our objective is to set up a VBS framework that contains the sensitivity to conditions (temperatures, coreactants, etc.) that will influence condensible product yields in the real world. To do this, we shall cast the RO_2 radicals in Scheme 3 into the 2D-VBS. One of the potential fates of each RO_2 is autooxidation to a more highly oxygenated RO_2, designated $(O_x)_nRO_2$, where the root RO_2 can be thought of as $(O_x)_0RO_2$. We can assign the surrogate RO_2 species a nominal volatility, as shown in Fig. 4.5. This volatility is important for three reasons. First, the termination to molecular products is defined by a series of "kernels" anchored by the VBS properties of the RO_2 (C^o and O:C). Second, the RO_2 self-reactions may involve clustering that influences the overall reaction, and the cluster lifetime will be related to the RO_2 volatility. Third, typical RO_2 gas-phase lifetimes range from 1 to 1000 s in the atmosphere, and the collision frequency with particle surface area in the atmosphere ranges between 10^{-3} and $1\,s^{-1}$.[39] These are often correlated, but nonetheless there are many occasions where RO_2 radicals will encounter particle surfaces before reacting in the gas phase. This may be especially true in smog-chamber experiments with highly elevated condensation sinks. Consequently, heterogeneous reactions of RO_2 may well be important, and even if the radicals have relatively low intrinsic reactivity, their volatility may contribute to their behavior.

Each nominal reaction in Reactions 4.3–4.11 represents dozens of individual elementary reactions, including a number of terminating reaction partners X = HO_2, RO_2, NO, NO_2, OH, etc. For this sequence, the terms SVOC, LVOC, and ELVOC in Reactions 4.3–4.11 refer to the three classes of products already presented (conventional small hydrocarbon oxidation, autooxidation, and dimerization). However, each of the termination processes involving either a reaction partner X or unimolecular termination (as with Reaction 4.9) will form a distribution of products in the 2D-VBS with a range of volatility and oxidation state. This is partly because a single bimolecular reactive encounter may form multiple products, and partly because each surrogate RO_2 represents a group of similar radicals. Each of these termination processes can be described by a "kernel" giving a shift in volatility and oxidation state relative to a reference point (in this case, the nominal location of the RO_2 shown in Fig. 4.5). In the original 2D-VBS description, the true kernels describe changes to C^o and n_O (the oxygen number) with the change in O:C being given by the nominal carbon number in a given bin; here we are using C_{10} precursors (monoterpenes) as an example and

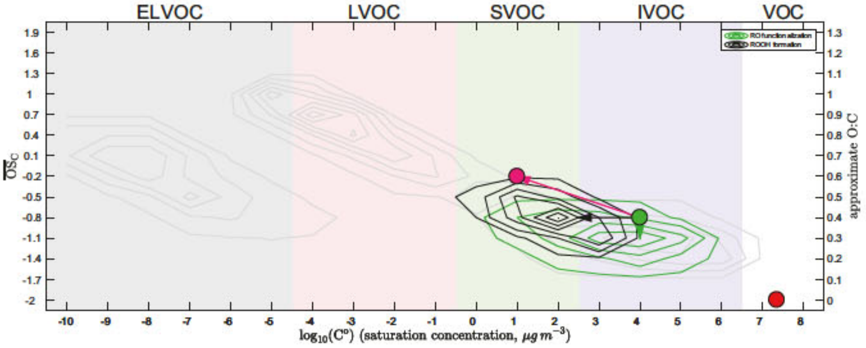

Fig. 4.6 Oxidation kernels important to RO_2 species. Propagation to RO radicals resolves into products shown with green contours, and formation of peroxides (ROOH) forms products shown with black contours. Finally, the RO_2 can undergo autooxidation to produce a more highly oxidized RO_2 (magenta circle).

a change $\delta n_{\mathrm{O}} = 1$ corresponds to δ O:C $= 0.1$, which happens to be exactly the usual spacing of the 2D-VBS grid.

The framework presented here is just that — a framework that may describe the essential features of autooxidation. Those features are as follows. Some fraction of the α-pinene will resolve to molecular products more or less immediately (possibly through Criegee Intermediates) while the rest will form first-generation peroxy radicals. Those peroxy radicals will probably all have broadly similar rate constants and products for reactions with HO_2 and NO,[30] but may have variable rate constants for reaction with each other as well as unimolecular autooxidation.[33] The RO_2 cross-reaction rate constants might be described by the geometric mean approximation put forward by Madronich.[40] In general, those cross-reactions become faster (with a lower activation energy) with the presence of electron-withdrawing functional groups near the peroxy moiety and slower (with a higher activation energy) with the presence of electron-donating functional groups near the peroxy moiety. For example, peroxy acyl radical self-reactions occur once in every 10 collisions whereas tert-butyl peroxy radical self-reactions occur less than once in every million collisions at room temperature.[41] The RO_2 cross-reactions also favor radical products $(RO + RO + O_2)$ when they are faster.[41,42]

At least for the moment, we are also assuming that formation of alkoxy radicals (RO) is a quasi-termination step, with resolution either to molecular products with the same carbon number (functionalization) or decomposition to smaller products (fragmentation).[43] Also, NO will react to form nitrates at a 25% yield with most of the rest of the RO following a fragmentation pathway. It is also likely that an important fraction of the $(O_x)_n\,RO_2$ are peroxy acyl radicals, in which case NO_2 will react to form peroxyacetyl nitrates (PANs). There is evidence in Ehn *et al.*[7] that upward of 1 ppbv of NO is required to strongly suppress autooxidation, suggesting a 5–10 s lifetime near 290 K. However, there is strong evidence in Frege *et al.*[29] that the extent of autooxidation is temperature dependent and evidence that the $(O_x)_n\,RO_2$ do terminate via bimolecular reactions.

4.3. Condensation Dynamics

One major reason to define the VBS oxidation kernels is to calculate the production rate of condensible organic compounds for equilibrium conditions, such as formation of secondary organic aerosol (SOA). However, the dynamics of aerosol condensation and evaporation are crucial to both new-particle formation and growth[44] and also to growth of freshly emitted nanoparticles,[39] controlling the probability that any nanoparticle will survive to a climate-relevant size (50–100 nm diameter).[45] Particles affect climate directly via light scattering once their circumference becomes similar to the wavelength of visible light (400–600 nm) and indirectly as cloud condensation nuclei (CCN) once they contain a sufficient number of moles of solute for Raoult's law to overcome the surface tension of a nucleating water droplet.[1]

Finally, organic aerosol properties are generally determined in experimental reactors — either chambers or flow reactors — and the relatively short timescales intrinsic to those chambers, compared to typical timescales encountered in the environment, means that consideration of aerosol dynamics is important. Before we turn to the overall dynamics governing a full aerosol size distribution, we shall first discuss condensation and evaporation in depth.

4.3.1. *Problem Setup*

We are interested in how chemical and physical processes change the concentration of organic aerosol, C_{OA}, measured in $\mu\mathrm{g\,m^{-3}}$. These processes include production (or loss), emission (or removal by dilution), changes in temperature, changes in humidity, and possibly others. However, even for highly controlled experiments, measurements to constrain these processes are often indirect. Most commonly, SOA production is inferred based on the observed loss of a precursor, ΔC_{prec}, and production of SOA, ΔC_{OA}, which in turn is based on observed changes in either particle volume, particle diameter, or the organic to seed mass ratio (O:S) of seed particles.

We shall consider a chemical species, i, with some total concentration, C_i^{tot}, in suspension in all phases (vapor, v; suspended particulate, s; aqueous liquid, l). Here the "species" will refer to an ensemble of compounds with similar volatility and perhaps oxidation state in a 1D- or 2D-VBS. We will designate different reservoirs with a superscript, and so the species, i, will have phase-specific concentrations C_i^v, C_i^s, C_i^l, with $C_i^{tot} = C_i^v + C_i^s + C_i^l$. For the most part in this discussion, we shall neglect the aqueous phase and focus on the vapor and particulate phases. We also shall keep in mind that there may be several suspended particulate phases, even within individual particles. Here any unique particles will be designated with a second subscript, p; these could be particles of a different size within a distribution, or particles with a different inorganic core. Absent the second subscript, we are referring to the ensemble, i.e., $C_i^s = \sum_p C_{i,p}^s$. The same nomenclature would apply to different "droplets" for aqueous particles, i.e., $C_{i,d}^l$. The potential distribution of a species within an individual particle (in distinct phases or in different locations for very viscous particles with low internal diffusivity) is a separate and important issue.$^{46-52}$

The problem of organic aerosol is fundamentally the problem of the relative abundance of species i in these different phases — both at equilibrium and dynamically, out of equilibrium — when equilibration timescales are not fast. A complication is that all experiments are conducted in containers — teflon, glass, or metal chambers or glass or metal flow reactors — and those containers have walls. This introduces several new reservoirs: the near-wall region (the base of the boundary layer), w; vapors adsorbed on the wall, a; particles deposited on the wall, d; and for permeable walls vapors absorbed in the near-surface layer of the (teflon) wall, t; and, potentially, vapors that have permeated more deeply into the walls, p. For a mass balance we should consider the total mass in each reservoir for a chamber with volume V and surface area S (and thus volume to surface–area ratio $V{:}S$): $M^{\mathrm{tot}} = M^v + M^s + M^l + M^w + M^a + M^d + M^t + M^p$. Concentrations in this work refer to mass per unit chamber volume, $C = M/V$, typically in $\mu\mathrm{g\,m^{-3}}$; most of the mass terms associated with the experiment walls are more naturally expressed as a surface-area concentration, i.e., $\mu\mathrm{g\,m^{-2}}$, and so $V{:}S$ ($\mathrm{m^3/m^2 = m}$) will often appear in expressions for those concentrations (or fluxes).

The microphysics is in large part governed by the fluxes between the various reservoirs, Φ, which we shall designate with a dual superscript. For example, the net flux from the vapor to the (ensemble) suspended-particle phase for species i is $\Phi_i^{v,s}$. When referring to a flux per unit chamber volume, we shall use the capital, Φ, while when referring to a flux per unit condensed-phase surface area we shall use the lower-case, ϕ. The sign convention will be a positive flux being from the reservoir expressed by the first superscript to the second, so in this case, a positive flux from the vapor phase to the suspended-particle phase is net condensation (particle growth), while a negative flux would be net evaporation (particle shrinkage). These again will be expressed as a mass flux per unit volume of air, or $\mu\mathrm{g\,m^{-3}\,s^{-1}}$. Furthermore, both in the atmosphere and in many chamber experiments, an hour is a more natural unit of time, as experiments often occur over several hours and changes in the atmosphere most often scale over hours (e.g., particle growth rates are often given in $\mathrm{nm\,h^{-1}}$). We shall thus often quote fluxes and rates using 1 h as the unit of time.

We shall further consider production (or emission) of compound i, P_i; as with the other fluxes this is *net* production (production – loss) and can also include net emissions (i.e., emission – dilution loss of vapors and particles). The net production can occur in any phase, so $P_i^{\mathrm{tot}} = P_i^v + P_i^s + \cdots$. When we represent an ensemble of binned species, e.g., within the VBS, we can make a distinction between transformation within the VBS, $T_{i,j}$, which constitutes loss of species i and production of species j, and production or loss "out of" the VBS.[14,15,17] Here we shall mostly focus on the microphysics and dynamics rather than chemical transformations, usually for a single species (or bin); so, for the most part, we shall not discuss these transformation or "aging" reactions.

Production often results from oxidation (loss) of a volatile precursor, L_{prec}, such as the α-pinene oxidation discussed above. Because we will relate precursor chemical loss to aerosol production, we do not lump terms into net production but specify them individually:

$$\frac{dC_{prec}}{dt} = -L_{\text{prec}} + (P_{\text{prec}} + E_{\text{prec}} - D_{\text{prec}}); P_i = y_i\, L_{\text{prec}} \qquad (4.14)$$

where y_i is the yield of species i. On a molar or carbon basis, for all products $\sum_i y_i = 1$, but often many product species are unknown and many observations constrain total mass. We thus typically consider mass yields with $\sum_i y_i > 1$; where possible (e.g., in the 2D-VBS) we track carbon, where $\sum_i y_{\text{C},i} = 1$, but this also requires that we know or can calculate $(\text{OM:OC})_i$. The terms in parentheses in Eq. (4.14) are often assumed to be negligible during experiments; then the observed change in precursor concentration ($\text{d}C_{\text{prec}}/\text{d}t$ or ΔC_{prec}) can be tied directly to production of the condensible species. However, this is not always valid; an especially vexing case is when the precursor is itself semi-volatile with a significant mass burden either in the suspended particles or the (teflon) chamber walls (an example is the first-generation α-pinene product pinanediol).[53–55] In that case, chemical depletion in the gas phase can be counterbalanced by evaporation to the gas phase from those condensed phases.

We are often interested in the fraction, f, of the production in Eq. (4.14) that ends up in the condensed phase. This can be applied to individual product molecules, f_i, and also to the overall process, f_{prec}. In the latter case, this is the aerosol mass yield of the process. In concept, the aerosol mass yield is straightforward:

$$y_M^s = \Delta C^s / \Delta C_{\text{prec}} \qquad (4.15)$$

However, this is also close to meaningless. The aerosol mass yield is a consequence of both thermodynamics (the equilibrium phase partitioning of organics in a complex mixture) and potentially dynamics (the fraction of products in the condensed phase at any given time regardless of their equilibrium propensity). Consequently, it is far more informative and useful to determine the yields of specific species (or groups of them) and then calculate the mass yields. Here our focus is on the dynamics of that process.

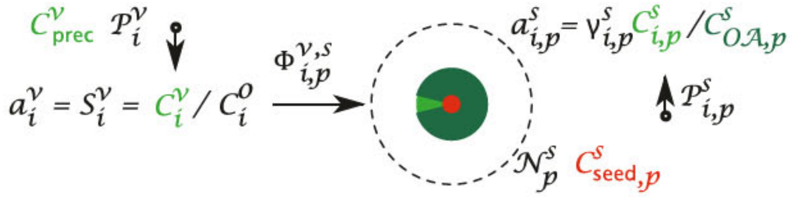

Fig. 4.7 Terms associated with an organic aerosol suspension with an organic species (i) in both vapor-phase (v) and suspended-phase (s) reservoirs (concentrations C_i^v and C_i^s), along with net production terms (P_i), expressions for activity in each phase (a_i^v, a_i^s), and the net condensation flux from the vapor to the suspended phase ($\Phi_{i,p}^{v,s}$). The particle population with total suspended number concentration N_p^s consists of a seed (red) and the organic species (light green) in a mixture with other organics (dark green) with the indicated activity coefficient $\gamma_{i,p}$. A nominal boundary layer with a scale length of one particle radius is indicated with a dashed circle; this is the scale length for any gas-phase concentration gradients near the particle.

4.3.2. *Condensation and Aerosol Suspensions*

We shall begin our discussion with an ideal aerosol suspension, depicted in Fig. 4.7. In this example, we shall consider only a vapor and a suspended-particle phase, with no walls or wall losses and no particle coagulation. While this imaginary wall-free world forms the basis of our intuition, we again emphasize that wall losses of vapors and particles can be very important in the real wall-filled world.[22,56–59]

In this ideal system, there are n_i different organic species or surrogates (bins) and n_p different particle populations. The suspended-particle number concentration of population p is N_p^s and the mass concentration of an inorganic seed in that population is $C^s_{\text{seed,p}}$. In many organic aerosol experiments, the seed consists of ammonium sulfate. The differential equations representing the system (with terms defined in the caption to Fig. 4.7) are

$$\begin{aligned} \mathrm{d}C_i^v/\mathrm{d}t &= P_i^v - \sum_p \Phi_{i,p}^{v,s} \\ \mathrm{d}C_{i,p}^s/\mathrm{d}t &= P_{i,p}^s + \Phi_{i,p}^{v,s} \end{aligned} \tag{4.16}$$

Thus, the total suspended concentrations are

$$C_i^s = \sum_p C_{i,p}^s \quad C_{\text{seed}}^s = \sum_p C_{\text{seed},p}^s \quad N^s = \sum_p N_p^s$$
$$C_{\text{OA},p}^s = \sum_i C_{i,p}^s \quad C_{\text{OA}}^s = \sum_i C_i^s = \sum_p C_{\text{OA},p}^s \tag{4.17}$$

In this formulation, the individual suspended-particle diameter d_p^s, surface area s_p^s, and volume v_p^s, as well as the total surface area $S_p^s = s_p^s N_p^s$ and volume $V_p^s = v_p^s N_p^s$ are all derived quantities depending on mass loading and density (in practice, we almost always assume a constant organic density $\rho_{i,p} = \rho_{\text{org}}$ and seldom consider varying density in the organic mixture, i.e., the p dependence):

$$v_p^s = \frac{1}{N_p^s}\left[\frac{C_{seed,p}^s}{\rho_{seed}} + \sum_i \frac{C_{i,p}^s}{\rho_{i,p}}\right]; \quad d_p^s = \sqrt[3]{\frac{6\, v_p^s}{\pi}} \tag{4.18}$$

This is the basis for a monodisperse[60,61] or a moving sectional[62] algorithm. It is not practical for simulation of particle size distributions where any of mixing, nucleation, or coagulation are important (discussed below), but it is much more straightforward than either sectional or modal formulations and thus better suited for consideration of the fundamental physics and chemistry. However, Eq. (4.17) and the following are readily formulated in terms of distributions (i.e., $n_N^{\circ,s} = dN^s/d\log_{10} d_p$).[63] In this section, we shall consider a monodisperse population N_p^s (the exception being mixing experiments with two particle populations), and so we shall focus on the net condensation alone for a wide range of condensible organic saturation concentrations. For the full aerosol microphysics presented in Section 4.4, we shall implement a moving sectional algorithm based on this same formulation as part of an operator splitting treatment.

4.3.2.1. *Vapor-particle Flux*

The net condensation flux $\Phi_{i,p}^{v,s}$ of a trace species with vapor concentration C_i^v and saturation concentration C_i° to a suspension of identical particles p with number concentration N_p^s and diameter d_p is

$$\Phi^{v,s}_{i,p} = N^s_p \underbrace{\left(\pi \, \frac{(d_p + d_i)^2}{4}\right)}_{\sigma_{i,p}} \; \underbrace{\alpha_{i,p} \, \bar{c}_{i,p} \, B_{i,p}}_{s'_{i,p}} \; \underbrace{\left[C^v_i - a^s_{i,p} \, C^\circ_i\right]}_{F^{v,s}_{i,p}} \qquad (4.19)$$

There are four elements to this equation: the suspended-particle number concentration (N^s_p, the number of particles per unit volume, e.g., m^{-3}); a particle–vapor collision cross section ($\sigma_{i,p} = \pi \, (d_p + d_i)^2/4$, with units of area, e.g., m^2); an effective deposition speed of vapors at the surface ($s'_{i,p} = \alpha_{i,p} \, \bar{c}_{i,p} \, B_{i,p}$, with units of length/time, e.g., $\mathrm{m\,s^{-1}}$); and a condensation driving force ($F^{v,s}_{i,p} = C^v_i - a^s_{i,p} \, C^\circ_i$, with units of concentration, e.g., $\mu\mathrm{g\,m^{-3}}$).

The commonly used units for these terms can be confusing. First, particles are classified by their diameter (not radius). Second, it is conventional to describe aerosols by a mass concentration in a (standard) cubic meter of air, $\mu\mathrm{g\,m^{-3}}$. This is because the standard method of measurement is to weigh a filter after drawing a known volume through it. Further, we often have a tighter constraint on the total mass of, e.g., organics than their molar concentration, as the molecular weights of unknown species are not known. Finally, particle number concentrations (along with the concentrations of gas-phase species) are typically reported in number per cm^3 of dry air.

We shall discuss the final three terms of Eq. (4.19) in order.

4.3.2.1.1. Cross Section

Collisions are described by a cross section and a speed, as shown in Fig. 4.8. In many ways, there are three limiting regimes for particle growth: a "collisional regime" in which both the particle and the interacting molecule are of comparable size and mass, a "kinetic regime" in which there is no gas-phase diffusion limitation to molecule–particle collisions yet the molecules are small and light compared to the particles, and a "continuum regime" in which diffusion to the particle surface is rate limiting. In the collisional regime, the collision cross section is the appropriate metric of a collision probability. At the hard-sphere limit for neutral species,

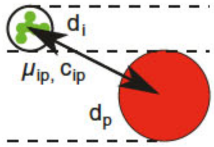

Fig. 4.8 Terms important to collisions between molecules and particles. A molecule with effective hard-sphere diameter d_i and mass m_i strikes a particle with a volume equivalent diameter d_p and mass m_p with a hard-sphere cross section $\pi(d_p + d_i)^2/4$ at a speed $c_{i,p}$ defined by a reduced mass $\mu_{i,p} = m_i m_p/(m_i + m_p)$.

this is given by $\sigma_{i,p} = \pi\,(d_p + d_i)^2/4$. The presence of the molecular effective diameter, d_i, in the expression is notable and important. More generally, $\sigma_{i,p}$ can be influenced by charge interactions (i.e., charge–charge, charge–dipole, dipole–dipole, etc.), especially for very small particles. Other than the like-charge repulsion, these interactions generally enhance the cross section, but here we shall consider only the hard-sphere limit.

The appropriate value of d_i is not obvious, as indicated in Fig. 4.8. One common choice is the diameter associated with the bulk specific volume of the pure substance[23,64]:

$$d_i = \sqrt[3]{\frac{6\,m_i}{\pi\,\rho_i}}. \tag{4.20}$$

A second choice is the physical hard-sphere size of the molecule. The definition of d_i ought to extend to monomer collisions forming dimers — the first step in particle nucleation. The equilibrium separation of molecules in a liquid is necessarily larger than the Van der Waals minimum in the pairwise interaction potential, and while a collision between two molecules at this distance will certainly result in significant deflection and thus be germane to the angular collisional cross section, it may or may not result in capture. Thus, while interactions at this distance could be described as collisions, the mass accommodation coefficient $\alpha_{i,p}$ would be much less than 1.0. In fact, in the collisional limit, the mass accommodation coefficient has no separate meaning; it is merely a scaling factor relating some effective target size to the actual target size for capture (condensation). In this context, an appropriate choice for d_i would be one that keeps the value of $\alpha_{i,p}$ roughly constant as a function of particle size, d_p. The appropriate interaction (capture) distance will also likely depend on the effective number of atoms (degrees of freedom) in the two colliding objects; as for small objects, the collision will be at the low-pressure limit, but for larger objects with more degrees of freedom, the interaction will likely be at the high-pressure limit.

One difference between particle microphysics formulations and typical derivations of the kinetic theory of gases is that it is conventional to consider vapor condensation to particles in terms of the particle surface area alone (rather than a cross section), with surface area, $s_p^s = \pi d_p^2$. There is often an implicit assumption that the vapors are light and small (effectively point sized), and the particles are heavy and large (effectively stationary) so that the interaction can be described in terms of the speed of the vapor molecule and the surface area of the particle alone. One objective here is to present a formulation that cleanly covers the full range of vapor and particle sizes important to the atmosphere, especially for the case of new-particle formation where "particles" are molecular clusters at or near the "critical cluster" free-energy maximum for nucleation.

We can recast Eq. (4.19) in terms of particle surface area by factoring out a "molecular size enhancement", $\epsilon_{i,p}$, to relate the (circular) cross section to the (spherical) surface area, given by

$$\epsilon_{i,p} = 4\,\frac{\sigma_{i,p}}{\pi\, d_p^2} = \frac{(d_p + d_i)^2}{d_p^2}. \tag{4.21}$$

Given that monomers are typically smaller than 1 nm in physical size ($d_i < 1$ nm), once particles reach 10 nm or so, the collision enhancement makes a difference of less than 10% to the flux. The factor of (1/4) is also conventionally associated with the "normal speed" of gas-surface collisions, $\bar{c}_{i,p}/4$.[63] Thus, when converting from a (circular) cross section to a spherical surface area, Eq. (4.19) becomes

$$\Phi_{i,p}^{s,v} = N_p^s\, s_p^s\, \phi_{i,p}^{s,v}; \quad \phi_{i,p}^{s,v} = \left(\epsilon_{i,p}\,\frac{\bar{c}_{i,p}}{4}\alpha_{i,p}\, B_{i,p}\right) F_{i,p} \tag{4.22}$$

where $\phi_{i,p}^{s,v}$ is the mass flux per unit surface area of the suspended-particle population p.

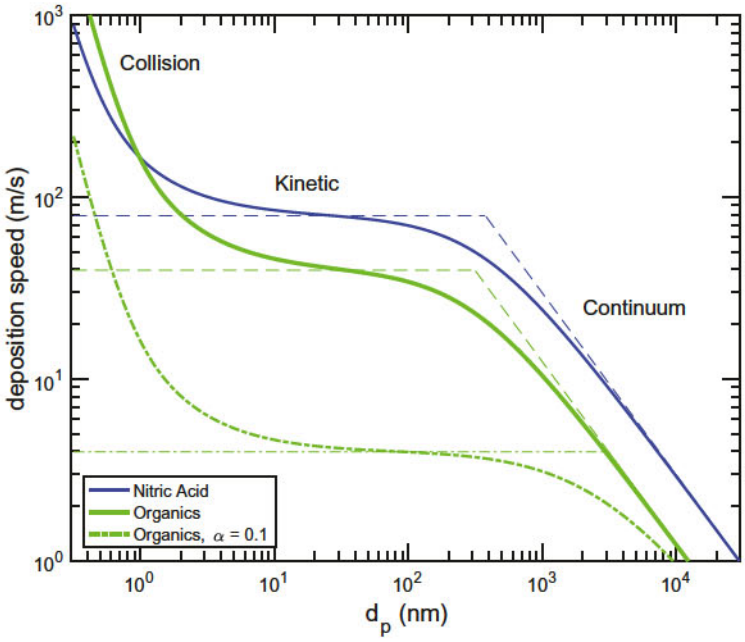

Fig. 4.9 Deposition speed for species to a particle surface vs. diameter. Two representative species are 63 amu nitric acid with an effective collisional diameter of 0.4 nm (blue) and 250 amu organic molecules with an effective collisional diameter of 0.8 nm (green). The solid curves are for a mass accommodation coefficient of $\alpha = 1$, the dashed curve is for organics with $\alpha = 0.1$. Collisions to very small particles (the collision regime) are faster than the simple molecular collision speed (the kinetic regime), while collisions to larger particles are limited by gas-phase diffusion (the continuum regime), but the influence of nonunit α diminishes.

4.3.2.1.2. Deposition Speed

The deposition speed is the speed with which gases collide with and are taken up by (or evaporate from) the particles. Figure 4.9 shows values for nitric acid and a typical condensible organic vapor over a wide particle size range and also illustrates the three limiting regimes. In these equations, $\alpha_{i,p}$ is the accommodation coefficient of species i on the particles p, and $\bar{c}_{i,p}$ is the center-of-mass collision speed of species i with the particle:

$$\bar{c}_{i,p} = \sqrt{8\,RT/(\pi\mu_{i,p})}. \tag{4.23}$$

Note that for collisions between vapors and ultrafine particles, the mean relative speed is somewhat higher than just the mean molecular speed because the appropriate mass is the reduced mass of the condensing molecule and the particle:

$$\mu_{i,p} = \frac{m_i\, m_p}{m_i + m_p}. \tag{4.24}$$

Just as with the cross section, it is conventional to consider the speed of the molecule over a static particle. To extract this, we can express the center-of-mass velocity in terms of the molecular speed and a speed enhancement factor

$$\bar{c}_i = \sqrt{8\,RT/(\pi\, m_i)}; \quad e_{i,p} = \sqrt{(m_i + m_p)/m_p}. \tag{4.25}$$

If we include both "enhancements" associated with the finite size and mass of the molecule sticking to a unit particle surface area, the deposition speed is

$$s_{i,p} = (e_{i,p}\, \epsilon_{i,p}\, B_{i,p})\, s_i^{\mathrm{kin}}; \quad s_i^{\mathrm{kin}} = \alpha_{i,p}\, \frac{\bar{c}_i}{4}. \tag{4.26}$$

Where s_i^{kin} is the deposition speed in the kinetic regime when collisions between the gas and particle are rate limiting, but the gas molecule is small and light compared to the particle.

With increasing particle diameter, diffusion from the bulk gas phase to the particle surface begins to limit the collision frequency and the microphysics enters the transition regime, and ultimately the continuum regime where gas-phase diffusion to the particle surface is fully rate-limiting. In the continuum regime, the deposition speed (flux per unit surface area and unit condensation driving force) is[63]

$$s_i^{\mathrm{cont}} = \frac{2\, D_{i,air}}{d_p} \tag{4.27}$$

Because the kinetic deposition speed is independent of diameter and the continuum deposition speed is inversely dependent on diameter, these two limiting values will intersect at some critical diameter d_p^{crit}

$$s_i^{\mathrm{cont}} = s_i^{\mathrm{kin}}; \quad \frac{2\, D_{i,air}}{d_p^{crit}} = \alpha_{i,p}\, \frac{\bar{c}_i}{4}; \quad d_p^{\mathrm{crit}} = \frac{8\, D_{i,air}}{\alpha_{i,p}\, e c_i} \tag{4.28}$$

We can define a modified Knudsen number based on the critical crossover diameter:

$$K_m = \frac{8\,D_{i,air}}{\alpha_{i,p}\bar{c}_i d_p} \tag{4.29}$$

For a simple resistor model, the diffusion limitation would be $1/(1 + 1/K_m)$ but more generally

$$s_{i,p} = (e_{i,p}\,\epsilon_{i,p})\,s_i^{\mathrm{kin}}\left(\frac{1}{1+\frac{1}{K_m}}\right)U_{i,p} \tag{4.30}$$

We illustrate this critical diameter for both nitric acid and an organic vapor in Fig. 4.9 by plotting both asymptotes as dashed lines.

The critical diameter and Knudsen number are related to the mean free path. The concept of a concentration gradient is meaningless on a length scale less than the mean free path. Further, any concentration gradients near a particle will vanish over a length scale proportional to the particle radius, so when the particle radius is much smaller than the mean free path, it is impossible to sustain a concentration gradient over a particle or to have any diffusion limitations in the gas phase; vapors simply collide randomly with the very small particles.

It is common for aerosol microphysics to be presented for large particles in the bulk regime and then corrected for $K_m \gtrsim 1$; here however, we use the kinetic regime as the "base" case and consider the onset of diffusion limitations in a laminar boundary layer around the particles as a limitation to mass transfer.[64] In Eq. (4.26), the term $U_{i,p} = U(K_m)$ is a transition-regime "broadening" correction to the simple Hinshelwood-like resistor expression in Eq. (4.30),[65] so the speed, $s_{i,p}$, is adjusted for uptake, diffusion, and finite size and mass of the colliding species, i:

$$U_{i,p} = \frac{(K_m+1)\,(0.75\,\alpha_{i,p}\,K_m+1)}{K_m\,(0.75\,\alpha_{i,p}\,K_m+1+0.283\,\alpha_{i,p})+1}. \tag{4.31}$$

The accommodation coefficient and the transition-regime correction are connected, as the correction represents the emergence of gas-phase concentration gradients near the particle. For very small particles ($K_m \gg 1$), there can be no gradients; for very large particles ($K_m \ll 1$), the gas concentration at the particle surface can be near zero even if $\alpha < 1$. It is convenient to distinguish molecules striking particles from molecules sticking to (accommodating into) particles. Thus, we define a collision speed $c_{i,p} = s_{i,p}\,(\alpha_{i,p} = 1)$ and an effective mass accommodation coefficient

$$\alpha'_{i,p} = \frac{\alpha_{i,p} K_m\,(0.75\,\alpha_{i,p} K_m + 1 + 0.283) + 1}{K_m\,(0.75\,\alpha_{i,p} K_m + 1 + 0.283\,\alpha_{i,p}) + 1}. \tag{4.32}$$

This is the fraction of molecules diffusing toward the particle surface (e.g., passing the imaginary demarcation surface one particle radius above the particle indicated in Fig. 4.7) that wind up accommodated into the particle. When $\alpha_{i,p} = 0.1$ and $K_m = 0.01, \alpha'_{i,p} \simeq 0.9$. The idea that the net flux can be diffusion limited by a diffusive boundary layer even when the accommodation coefficient is quite small is well known for diffusion to walls in chambers.[22,57,66]

It is important to establish proper scaling for the transition-regime correction (critical diameter) for different species, pressures, and temperatures. Even if we do not know specific diffusion constants, we can constrain how they differ from a reference value. The Chapman–Enskog expression for diffusion is[67]

$$D_{i,\mathrm{air}} = \frac{3}{2\sqrt{\pi}}\,\frac{(k_B T)^{3/2}}{\sqrt{2\mu_{i,air}}\,p\,d_{i,air}^2\,\Omega_{i,air}^{\prime(1,1)}} \tag{4.33}$$

Diffusivity depends on the reduced mass, $\mu_{i,\mathrm{air}}$, which for most but not all species of interest (exceptions being water vapor and ammonia) will be very nearly the average mass of air. The term Ω' is a collision integral normalized by the hard-sphere collision cross section, $\pi\,d_{i,\mathrm{air}}^2/4$. Again, for larger molecules this will be dominated by the size of the molecule, but the size of air molecules will rarely vanish. These two terms are directly analogous to the enhancements for collisions between molecules and extremely small particles in Eqs. 4.21 and 4.25.

For condensation of organics, the properties of the diffusing molecule will, in general, not be well known, and so it is best to scale relative to a reference compound. If we further consider a reference compound with diffusivity, $D_{\text{ref, air}}$, at reference temperature, T_0 (generally 300 K), and pressure, p_0 (generally 1 atm = 101325 Pa):

$$D_{i,\text{air}} = D_{\text{ref, air}} \left(\frac{T}{T_0}\right)^{3/2} \frac{p_0}{p} \sqrt{\frac{\mu_{ref,\,air}}{\mu_{i,air}}} \left(\frac{d_{ref,\,air}}{d_{i,air}}\right)^2 \frac{\Omega'^{(1,1)}_{ref,\,air}}{\Omega'^{(1,1)}_{i,air}} \tag{4.34}$$

The effective collisional diameter of air is $d_{\text{air}} \simeq 0.26\,\text{nm}$ given the observed self-diffusivity of air, $D_{\text{air}} = 2.02 \times 10^{-5}\,\text{m}^2\,\text{s}^{-1}$. Note that the spherical equivalent diameter of air based on bulk density given by Eq. (4.20) is 0.47 nm, and the contribution of air to the mobility diameter of particles is 0.3 nm.[68] At least for diffusivity, we can postulate a relationship between the bulk effective diameter and the collisional diameter using a scaling factor, δ:

$$d_i \simeq \delta \sqrt[3]{\frac{6\,m_i}{\pi\,\rho_i}}; \quad \delta \simeq \frac{2}{3}. \tag{4.35}$$

Whether or not $\delta = 2/3$ as suggested here, as long as it is relatively constant for the reference and target species then the overall scaling holds:

$$D_{i,\text{air}} \simeq D_{\text{ref, air}} \left(\frac{T}{T_0}\right)^{m} \frac{p_0}{p} \sqrt{\frac{m_{ref}(m_i + m_{air})}{m_i(m_{ref} + m_{air})}} \left(\frac{\frac{m_{ref}}{\rho_{ref}} + \frac{m_{air}}{\rho_{air}}}{\frac{m_i}{\rho_i} + \frac{m_{air}}{\rho_{air}}}\right)^{2/3} \tag{4.36}$$

where the density of (liquid) air is $\rho_{\text{air}} \simeq 874\ \text{kg}\,\text{m}^{-3}$. The temperature exponent, m, is in practice between 1.5 and 2.0 due to the temperature dependence of the collision integral, Ω'. In many cases, $m \simeq 1.7$.[67] For organics typically associated with oxidation of monoterpenes and other relatively large VOCs, diffusivities of polycyclic aromatic hydrocarbons provide a relatively well-studied reference pool.[69] We suggest a reference diffusivity $D_{\text{ref, air}} \simeq 6.6 \times 10^{-6}\,\text{m}^2\,\text{s}^{-1}$, with $M_{\text{ref}} \simeq 200\,\text{g}\,\text{mole}^{-1}$ and $\rho_{\text{ref}} \simeq 1.2 \times 10^3\,\text{kg}\,\text{m}^{-3}$. The critical particle diameter where the kinetic and continuum limiting deposition speeds meet for this reference species is $d_p^{\text{crit}} = 296\,\text{nm}$, whereas for molecular oxygen ($D_{\text{O}_2,\,\text{air}} \simeq 17.6 \times 10^{-6}$) it is 316 nm.

Note that the corresponding mean free paths by the conventional definition are 111 and 118 nm.

For relatively large and massive constituents (compared with air), the dominant effect of increasing mass will be on the cross section, with $D \propto m^{-2/3}$. Most notably, diffusivity will *not* scale like $m^{-1/2}$, as the reduced mass of the collisions will be totally determined by the mass of air molecules. For different systems, as the mass increases, the characteristic distance will scale with $d_p^{\mathrm{crit}} \propto D_{i,\mathrm{air}}/\bar{c}_i \propto m^{-2/3}/m^{-1/2} \propto m^{-1/6}$. The bottom line is that the critical diameter (mean free path, Knudsen number, etc.) will be a very weak function of mass for condensing vapors, as the comparison between the reference polycyclic aromatic hydrocarbon (PAH) and molecular oxygen shows. However, as pressure and temperature change (especially pressure), the value will change significantly. It is very important to realize that the "mean free path" in these formulations is a parameter that helps form a dimensionless Knudsen number that in turn helps with an asymptotic flux matching for the transition between the kinetic and continuum regimes — it is not a physical mean free path but only a phenomenological one, and the correct value is related in this case to the bulk diffusivity. In addition, provided that the majority of the aerosol surface area is found on particles smaller than a few 100 nm under most conditions, the influence of the diffusion coefficients will be very small, and instead exactly known kinetic properties (mass and speed) will dominate.

Ultimately we can express the deposition speed as a simple molecular normal speed modified by a series of correction terms. The term $(e_{i,p}\, \epsilon_{i,p}\, \alpha_{i,p}\, B_{i,p})$ represents all corrections to the simple deposition speed expected for a molecule with mean normal speed, $\bar{c}_i/4$, with respect to a unit particle surface area, which defines the traditional "kinetic limit".[63] The two enhancement terms increase the effective speed for very small particles, while the Fuchs term represents flux limitations and thus decreases the effective speed for larger (transition and continuum regime) particles. As Fig. 4.9 shows, there is a range for $10 \leq d_p \leq 100$ nm where the "traditional" kinetic formulation holds to within about 20%, but really the curves are almost never horizontal; however, the diffusion constant has a modest effect on the collision speed over most of the range relevant to particle growth and the condensation sink.

4.3.2.1.3. Condensation Driving Force

With the particle surface area and vapor deposition speed defined, the final element of the condensation flux is the thermodynamic driving force. A second way to write Eq. (4.19) for the net condensation flux is in terms of the effective accommodation coefficient and the collision frequency of molecules with suspended particles,

$$\Phi_{i,p}^{v,s} = \alpha'_{i,p}\,\nu_{i,p}^{s}\,C_i^{\mathrm{o}}[S_i^{v} - a_{i,p}^{s}]. \tag{4.37}$$

where the term in brackets is the excess saturation ratio, $S_{i,p}^{v,s;\mathrm{XS}}$. The condensation driving force $F_{i,p}^{v,s}$ is

$$F_{i,p}^{v,s} = [C_i^{v} - a_{i,p}^{s}\,C_i^{\mathrm{o}}] = C_i^{\mathrm{o}}\,S_{i,p}^{v,s;\mathrm{XS}} \tag{4.38}$$

where the excess saturation ratio is the fundamental activity difference between the two phases. The saturation ratio (gas-phase activity) is $S_i^{v} = C_i^{v}/C_i^{\mathrm{o}}$. The term $a_{i,p}^{s}$ is the condensed-phase activity of species i at the surface of the particle. If the particle is well mixed and large enough to be effectively flat, this can be expressed in terms of the bulk particle composition (in the dominant organic phase), $({a'}_{i,p}^{s} = X_{i,p}\,\gamma_{i,p})$, where $X_{i,p} = C_{i,p}^{s}/C_p^{s}$ is the mass fraction and $\gamma_{i,p}$ is the mass-based activity coefficient in the organic condensed phase. Even if species i is surface active, its surface activity must equal its bulk activity at equilibrium (though the surface concentration may be greatly enhanced).

For small, curved particles, the activity,

$$a_{i,p}^{s} = {a'}_{i,p}^{s}\,K_{i,p}, \tag{4.39}$$

includes the Kelvin term. The Kelvin term $K_{i,p}$ scales with a "Kelvin diameter" for decadal change, d_{K10}:

$$K_{i,p} = 10^{(d_{K10}/d_p)};\, d_{K10} = \log_{10}(e)\,(4\,\sigma\,M)/(R\,T\,\rho). \tag{4.40}$$

For a surface tension $\sigma = 0.03\,\mathrm{N\,m^{-1}}$ and a molar weight of $300\,\mathrm{g\,mole^{-1}}$ at 300 K, $d_{K10} \simeq 4.5\,\mathrm{nm}$. In the important special case of Köhler theory for activation of cloud droplets, the Kelvin term is critically important even for large (1–10 μm)) water droplets, but this is only true because the relevant critical supersaturations of water vapor are $S^{\mathrm{XS}} < 1\%$; for organic mixtures where volatility C_i° varies over orders of magnitude, the Kelvin term only significantly influences the smallest particles ($d_p \lesssim 10\,\mathrm{nm}$). For those particles, $a'_{i,p} \gg 1$, and so a large supersaturation is required to drive condensation. For $d_{K10} = 4.5\,\mathrm{nm}$ volatility over 4.5 nm diameter spheres increases by one order of magnitude compared to a flat surface, volatility over 2.25 nm diameter spheres increases by two orders of magnitude, and volatility over 1.1 nm diameter spheres increases by three orders of magnitude. A $300\,\mathrm{g\,mole^{-1}}$ monomer with a bulk density of $1400\,\mathrm{kg\,m^{-3}}$, has a nominal spherical diameter of 0.9 nm, while a dimer has a diameter of 1.1 nm. This is why supersaturations of order 10,000 can be required for homogeneous nucleation of organic vapors.

When we examine the behavior of the ensemble such as the VBS, it is useful to consider the cumulative concentration of all constituents below a reference saturation concentration and the associated effective saturation ratio[70]:

$$C_i^{v,\mathrm{sum}} = \sum_j^{C_j^{\circ} \leq C_i^{\circ}} C_j^{v}; \quad S_i^{\mathrm{eff}} = C_i^{v,\mathrm{sum}} / C_i^{\circ} \tag{4.41}$$

This is valid and useful so long as the compounds form a reasonably ideal solution. It is not much different from lumping compounds with identical volatilities.

Two limitations or approximations deserve special mention for the smallest particles. First, this is a bulk representation, and to the extent that the representation is extended down to small molecular clusters, it will eventually be inaccurate. Formally, the Kelvin term $K_{i,p}(d_p)$ could subsume most of the noncontinuum factors via an empirical form that deviated from the simple exponential of Eq. (4.40). Second, we must emphasize that the condensation driving force depends on the *surface* activity. This may differ from the bulk activity, especially if the growth rate of the particle exceeds the diffusion rate within the particle (i.e., for glassy particles) and thus generates an inhomogeneous particle.[46–52] However, the condensed-phase activity only matters when the gas-phase activity is small; in cases where the steady-state gas-phase activity is much greater than 1.0 the condensed-phase activity only matters for tiny particles with $d_p \ll 10\,\text{nm}$ and otherwise condensation will be essentially irreversible, regardless of the condensed-phase properties.

4.3.2.2. *Limiting Cases and Important Parameters*

There are several important limiting cases as well as alternative groupings of the gas-particle flux Eq. (4.19).

4.3.2.2.1. Growth Rates

The deposition speed can be converted into a rate of diameter change per unit condensation driving force (i.e., given a driving force of $1\,\mu\text{g}\,\text{m}^{-3}$)[27]:

$$s_{i,p}^{\text{GR}} = 2\,s_{i,p}/\rho_i \tag{4.42}$$

If the speed and density are in MKS units, $\text{m}\,\text{s}^{-1}$ and $\text{kg}\,\text{m}^{-3}$, and if the concentration units (condensation driving force) are in $\mu\text{g}\,\text{m}^{-3}$, then this unscaled expression will be in units of nm s^{-1} ($\text{nm}\,\text{s}^{-1}/\text{gm}^{-3}$). Multiplying by $3600\,\text{s}\,\text{h}^{-1}$ will give $\text{nm}\,\text{h}^{-1}$, which is a standard unit for growth rates. Given the condensation driving force for each component, $F_{i,p}^{v,s}$ we can then calculate the individual component and total growth rate

$$R_{i,p}^{G} = s_{i,p}^{\text{GR}}\,F_{i,p}^{v,s}; \quad R_{p}^{G} = \sum_i R_{i,p}^{G} \tag{4.43}$$

If we know the driving force, we can predict the growth rate, but conversely, if we know the growth rate we know the condensation driving force; we can thus use an observed growth rate to constrain the gas-phase concentration of condensible species. As an example we can consider a species with a molar weight of $M_i \simeq 350\,\text{g}\,\text{mole}^{-1}$ and reasonably low volatility ($C_i^{\circ} \lesssim 0.01\,\mu\text{g}\,\text{m}^{-3}$) at 278 K, for which $\bar{c}_i \simeq 130\,\text{m}\,\text{s}^{-1}$. For a typical organic density of $1.4\,\text{g}\,\text{cm}^{-3} = 1400\,\text{kg}\,\text{m}^{-3}$, the monomer of this species has an effective physical diameter $d_i = 0.92\,\mathrm{nm}$ (a mobility diameter near 1.2 nm). It is reasonable to use the growth rate at 10 nm as a reference, because the traditional kinetic regime limit is closest to valid there.[23] Here both the Kelvin term and the collision enhancement will be small, yet diffusion limitations will be slight. To the extent that the condensing species at 10 nm have similar molar weights and densities, we can use R^G_{10} to estimate the condensation driving force relatively free of the Kelvin term:

$$F^{v,s}_{10} = R^G_{10}/s^{\mathrm{GR}}_{10} \simeq R^G_{10}/198(\mu\mathrm{g\,m^{-3}}) \tag{4.44}$$

More generally, the growth rate at a given diameter gives a direct estimate of the effective gas-phase concentration of condensible vapors (their concentration if they were nonvolatile). If the sinks are known, this constrains the production rate; if a precursor loss rate is known, this in turn constrains the yields.[23,26]

4.3.2.2.2. Collision Frequency and Condensation Sink

It is useful to know how often molecules collide with the surface of particles in population p. Given the collision speed $c_{i,p}$, the collision frequency of the vapors with suspended particles p is

$$\nu^s_{i,p} = (\pi d_p^2)\, N^s_p\, c_{i,p}. \tag{4.45}$$

This is the frequency with which species i collides with the particle population p. The total frequency with all particles is $\nu^s_i = \sum_p \nu^s_{i,p}$. The time constant for collisions is thus $\tau^{v,s}_i = 1/\nu^s_i$.

The suspended condensation sink, $k^s_{i,\mathrm{cond}} = \sum_p \alpha'_{i,p}\, \nu^s_{i,p}$, gives the actual time constant for exchange of vapors between particles and the gas phase. The condensation sink determines the fundamental equilibration timescale between the gas and particle phases, $\tau^{v,s}_{i,\mathrm{eq}} = 1/k^s_c$, when condensation is the main loss of vapors and the change in particle volume during equilibration is small.[71,72]

Of all parameters one should track in aerosol experiments, the collision frequency and the condensation sink are among the most important. Further, while it is common to report a "condensation sink," given an observed aerosol size distribution,[39] this is usually based on an assumed (unity) mass accommodation coefficient. Because the mass accommodation coefficient is not in general well known, the collision frequency for a standard vapor with a known mass and size (often sulfuric acid) is a more robust and precisely defined quantity to report.

4.3.2.2.3. Evaporation Timescale

A second important timescale is for evaporation of species i from an individual particle.[73] Here we shall consider the case where either the species under consideration is a trace constituent or other factors prevent significant diameter change (i.e., exchange of isotopomers). For the evaporation timescale, we take the limit where the gas-phase concentration remains identically zero (i.e., there is a strong sink such as a vacuum, a sorbent, or other particles denuding the system of vapors). The mass of i in an individual particle is $X_{i,p}\,\rho_i\,v_p^s = X_{i,p}\,\rho_i \frac{\pi}{6} d_p^3$ while the evaporation flux from that particle is $\pi\, d_p^2\, s_{i,p}\, K_{i,p}\, X_{i,p}\, C^*_{i,p}$, so

$$\tau_{i,\mathrm{evap}} = \frac{\rho_i\, d_p}{6\, s_{i,p}\, K_{i,p}\, C^*_{i,p}} = \frac{\rho_i}{6\,\frac{\bar{c}_i}{4}\,\alpha_{i,p}}\;\frac{d_p}{e_{i,p}\,\epsilon_{i,p} B_{i,p}\, K_{i,p}}\;\frac{1}{C^*_{i,p}} \tag{4.46}$$

Here we have factored the expression into three terms: a prefactor, a term that depends on the particle diameter, and the inverse of the saturation concentration. We show the end result in Fig. 4.10 for a succession of saturation concentrations; the bottom line is that it will take about 1 h to drain all of the $1\,\mu\mathrm{g\,m^{-3}}$ material out of a 300 nm particle if the diffusion timescales within that particle are less than 1 h.

4.3.2.2.4. Diffusion Timescale

The third timescale is for diffusion within particles,[51]

$$\tau_{i,p} = d_p^2/(4\,\pi^2\,\mathcal{D}_{i,p}) \tag{4.47}$$

where $\mathcal{D}_{i,p}$ is the diffusion coefficient of compound i in particle p. The diffusion timescale will control whether particles reach an internal equilibrium and thus whether the surface activity of species i is equal

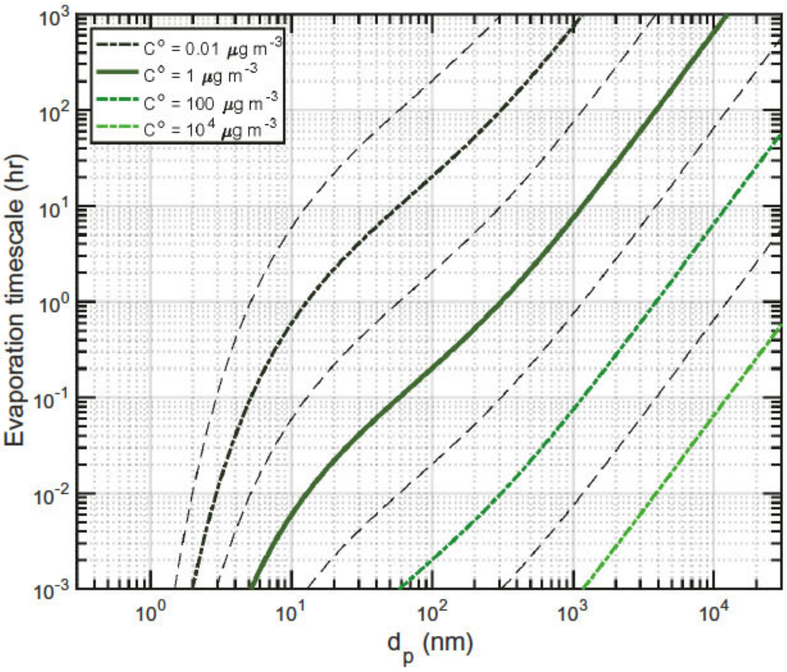

Fig. 4.10 Characteristic evaporation timescales (in hours) for organics vs. particle diameter d_p for a series of volatilities (C°). We use the four volatilities plotted with colored curves shown in the legend for a "gap" VBS later on. Organics with $C^{\circ} = 1\,\mu\mathrm{g\,m^{-3}}$ in a 300-nm particle will evaporate in approximately 1 h if mass accommodation is perfect and diffusion within the particle is more rapid than 1 h. For $d_p \lesssim 10\,\mathrm{nm}$, evaporation accelerates dramatically due to the Kelvin term and increased evaporation velocity and lifetimes plunge. These are timescales for evaporation of a trace constituent from a particle with constant d_p, in which case they give a first-order (exponential) timescale. For pure particles, evaporation is pseudo zeroth order because it accelerates as particles shrink.

to its bulk activity. Because $100\,\mathrm{nm}^2 = 10^{-10}\,\mathrm{cm}^2$, for $d_p = 100\,\mathrm{nm}$ and $\mathcal{D}_{i,p} = 10^{-15}\,\mathrm{cm^2\,s^{-1}}$, $\tau_{i,p} = 2500\,\mathrm{s}$ (40 min). This is roughly the timescale above which diffusion limitations are likely to be important in ambient particles, where most timescales are measured in hours. However, experiments conducted on much shorter timescales can be vulnerable to (or sensitive to) diffusion limitations with much higher diffusion constants.[50]

4.3.2.2.5. Overall Timescales

These timescales are very different from each other. The diffusion timescale will serve as a limitation for evaporation and/or exchange if $\tau_{i,p} \gtrsim \tau_{\text{evap}}$. A complex mixture will come into a steady state with respect to particle diameter change with timescale τ_{cond}, which is independent of volatility and often rapid, and yet complete removal of species i from the particles depends on C^{o} and can be very slow. However, if diffusion within the particle is slow, this equilibration timescale will be between the gas phase and the particle surface, and the ultimate equilibration timescale will again be determined by diffusion.

These timescales are often confused with each other. The evaporation timescale is not the equilibration timescale, and experiments designed to measure evaporation reveal little about equilibration, though they are highly informative in their own right. Further, whenever there is a net condensation flux, there must be an activity difference between the surface and the bulk of a particle; the question is how large it will be and that will depend on the condensed-phase diffusivity.[46,47]

4.3.2.2.6. Collision Frequencies on Particles

In some cases, it is important to know how often vapors collide with a given particle. Specifically, the collision frequency of vapors to a particle surface will govern whether the particle growth is uniform or relatively stochastic. This frequency is

$$\nu_{i,p}^{v,s} = (\pi\, d_p^2)\, s_{i,p}\, (C_i^v / m_i). \tag{4.48}$$

We show this in Fig. 4.11 for vapor concentrations ranging from $1\,\text{ng}\,\text{m}^{-3}$ to $1\,\mu\text{g}\,\text{m}^{-3}$, which would drive growth rates between 0.225 and $225\,\text{nm}\,\text{h}^{-1}$ in the kinetic regime. Particles larger than 100 nm are struck tens to thousands of times per second by (condensible) gas-phase molecules, but near 1 nm, small clusters are struck only once every 100 s if the growth rates are near ambient values ($C_i^v \simeq 0.01\,\mu\text{g}\,\text{m}^{-3}$) and roughly once per second at growth rates more commonly found in smog-chamber experiments.

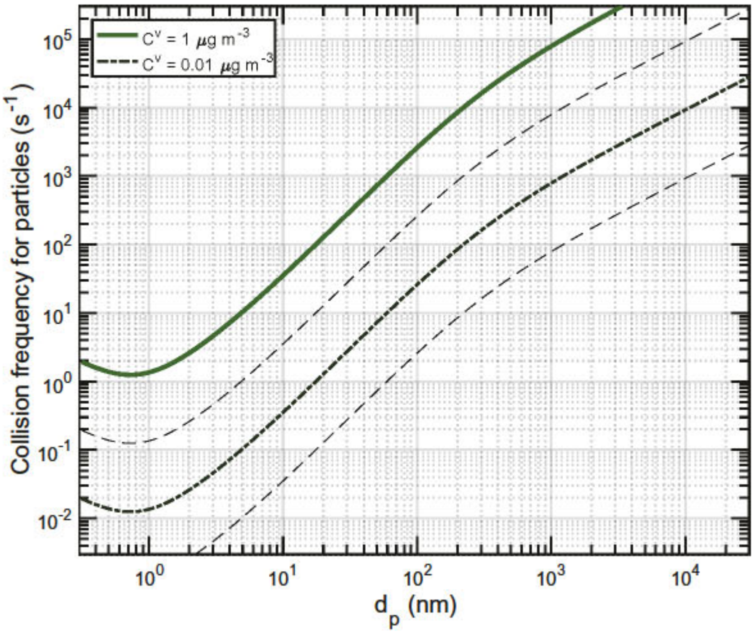

Fig. 4.11 Collision frequencies of vapors to particles as a function of particle diameter for different vapor concentrations C^v. This is the frequency with which a condensible vapor at concentration C^v strikes a particle of diameter d_p. For $C^v = 0.01\,\mu\text{g}\,\text{m}^{-3}$ (dark green dashed curve), where the kinetic growth rate is of order $2.25\,\text{nm}\,\text{h}^{-1}$, condensible vapors will strike a 1 nm diameter particle roughly once every 100 s.

Condensation growth is almost always modeled as a continuum process, so that the flux $\phi_{i,p}^{v,s}$ will be uniform to all particles and thus the entire population will grow at the same rate. However, at the lowest concentrations and growth rates, for the smallest particles, where the collision frequency is well under 1 Hz, this assumption may begin to break down. Instead, some fraction of particles at a given size may experience collisions in a given time step, causing them to grow in a process more akin to coagulation.

4.3.2.3. *Equilibrium Solution*

At equilibrium, the condensation driving force in Eq. (4.38) is zero. The mass fraction in population p is $X_{i,p} = C_{i,p}^s / C_p^s$. If we define

$C^{*}_{i,p} = \gamma_{i,p} C^{\circ}_{i}$ and a Kelvin adjusted volatility as $C^{*'}_{i} = K_i C^{*}_{i}$, then $a^{s}_{i,p} = \gamma_i K_{i,p} X_{i,p} = \gamma_{i,p} K_{i,p} C^{s}_{i,p}/C^{s}_{p}$. The equilibrium condition is $C^{v}_{i} - a^{s}_{i,p} C^{\circ}_{i} = 0$ and

$$C^{v}_{i} = C^{\circ}_{i} K_{i,p} \gamma_{i,p} C^{s}_{i,p}/C^{s}_{p} = C^{s}_{i,p} C^{*'}_{i}/C^{s}_{p} \tag{4.49}$$

This gives

$$C^{v}_{i}/C^{s}_{i,p} = C^{*'}_{i}/C^{s}_{p} \tag{4.50}$$

If the mass fraction of semi-volatiles is the same in all particles, then $X_i = C^{s}_{i}/C^{s}_{\mathrm{OA}}$ and so Eq. (4.49) holds for the bulk. In this case, the bulk fraction of species i in the suspended-particle phase, f^{s}_{i}, is

$$f^{s}_{i} = \frac{1}{1 + C^{*}_{i}/C^{s}_{OA}} \tag{4.51}$$

This is the foundation for organic aerosol calculations assuming equilibrium partitioning.[11,34] More generally, the equilibrium condition is that the activity of species i is the same in all phases and particles ($a^{s}_{i,p} = a^{s}_{i}$). For very small particles, the Kelvin term will ensure that more volatile species have a lower mass fraction and thus the same overall activity as larger particles unaffected by curvature.

4.3.2.3.1. Steady-state Solutions

Organic aerosol production, P_i, (or loss) is inherently not an equilibrium process, but many terms will reach a steady state in different situations. Here we shall consider only net production in the vapor phase, P^{v}_{i}. There are two relevant limits: one where condensation to suspended particles controls the vapor concentrations on a timescale given by the condensation sink ($\alpha'_i \nu^{s}_{i}$), and one where losses, k_i (i.e., wall losses) control those vapor concentrations. We are interested in the steady-state saturation ratio S^{ss}_{i} and excess saturation ratio $S^{\mathrm{XS,ss}}_{i}$.

When losses control the steady state, the steady-state saturation ratio will be a simple balance between production and loss: $S^{\mathrm{ss}}_{i} = (P_i/C^{\circ}_{i})/k_i$. If the suspended particles control the steady state, then it will involve a near balance between condensation and evaporation and the excess saturation ratio will be in steady state. A fraction of P_i will go to vapors and a fraction to the particles — this fraction will be approximately f_i^s.

$$\Phi_{i,p}^{v,s} = f_i^s\, P_i = \alpha'_{i,p}\, \nu_i^s\, C_i^\circ [S_i - a_{i,p}^s] = \alpha'_i\, \nu_i^s\, C_i^\circ\, S_i^{\mathrm{XS,ss}} \tag{4.52}$$

$$S_i^{\mathrm{XS,ss}} = f_i^s\, \frac{P_i/C_i^\circ}{\alpha'_i\, \nu_i^s} \tag{4.53}$$

S_i^{ss} is a key diagnostic for organic condensation. If $S_i^{\mathrm{ss}} \gg 1$, then the condensation will be essentially “nonvolatile” ($a_{i,p}^s$ will have no influence on the condensation), while if $S_i^{\mathrm{ss}} \lesssim 1$ then the condensation will be “semi-volatile”. Finally, if $S_i^{\mathrm{XS}} \ll 1$, then species i cannot be an important driver of condensation, as $a_{i,p}^s$ cannot grow larger than S_i during net gas-phase production.

4.3.3. *Idealized Experiments*

With the condensational dynamics laid out, we shall now turn our attention to a few idealized experiments to consider how condensation dynamics influence those experiments. The objective of almost any experiment involving SOA is to determine either the yields of various products, as in Eq. 4.14 or 4.15, or something about the physical characteristics of SOA that reasonably represents SOA found in the atmosphere. Experiments almost always involve a container of some sort (a chamber, a flowtube, etc.), but our conception of the experiment is often formed without considering that container, and also with some sort of notionally monodisperse aerosol in mind. Here we explore a few idealized experiments where there are no containers (and specifically no container walls), where mixing is homogeneous and for the most part instantaneous, for a mono-disperse population of relatively large particles.

4.3.3.1. *SOA Formation and Subsequent Dilution*

We shall first consider an idealized experiment with constant production of SOA, followed by a short relaxation period and then an instantaneous, large dilution step. The concept of this experiment is to perturb the aerosol equilibrium first via condensation driven by net production, allow equilibration, and then perturb the equilibrium again via dilution and subsequent evaporation. The reason for this simulation is that for two decades, SOA formation experiments have been interpreted in the context of equilibrium partitioning theory, starting with the pioneering work of Odum.[34] The key feature explained in that work was that experimental SOA mass yields ($Y = C_{\mathrm{OA}}/\Delta C_{\mathrm{prec}}$) are routinely observed to increase with increasing C_{OA}, which is consistent with equilibrium partitioning theory as presented in Eq. (4.51).

In addition to the features common to typical SOA formation experiments, we shall add two other steps. We shall assume that the production can be stopped instantaneously, and we shall let the particles rest for 20 min after production stops. Finally, we shall impose instantaneous dilution by a factor of 100 and consider subsequent evaporation over a period of 100 min. To distinguish the SOA production from dilution phases, we shall set $t = 0$ at the dilution step, so SOA production occurs at negative time and relaxation following the dilution step occurs at positive time.

For several reasons, when SOA mass production and not particle nucleation is the topic, it is useful to conduct experiments with seed particles, which are ideally completely noninteracting targets for condensation. Here we shall consider as a base case ("high seed") monodisperse seed particles with a suspended collision frequency $\nu^s_{c,\mathrm{seed}} \simeq 1\,\mathrm{min}^{-1}$, which is readily achieved with roughly 16,000 cm^{-3} of 100 nm diameter seed particles (about $15\,\mu\mathrm{g\,m}^{-3}$ of ammonium sulfate). For sensitivity calculation, we shall also consider a case ("low seed") with 10 times less seed aerosol and thus $k^s_{c,\mathrm{seed}} = 0.1\,\mathrm{min}^{-1}$. We shall assume that $\alpha = 1$ for the sake of this illustration, but there is a good deal of evidence that in general $0.1 \leq \alpha \leq 1$.[71,72,74,75]

The simplified model system we shall consider here consists of an oxidation reaction making four products with equal yields ($y_i = 0.25$ each) that form an ideal solution. The reaction will proceed at a rate $L_{\mathrm{prec}} = 1\,\mu\mathrm{g\,m}^{-3}\,\mathrm{min}^{-1}$, for 80 min, which is not atypical of SOA formation experiments. Ultimately, at equilibrium, there will be about $46\,\mu\mathrm{g\,m}^{-3}$ of SOA, with $d_p \simeq 180\,\mathrm{nm}$ and $\nu^s_c \simeq 2.5\,\mathrm{min}$ in the high-seed case and $d_p = 350\,\mathrm{nm}$ and $\nu^s_c \simeq 0.7\,\mathrm{min}$ in the low-seed case.

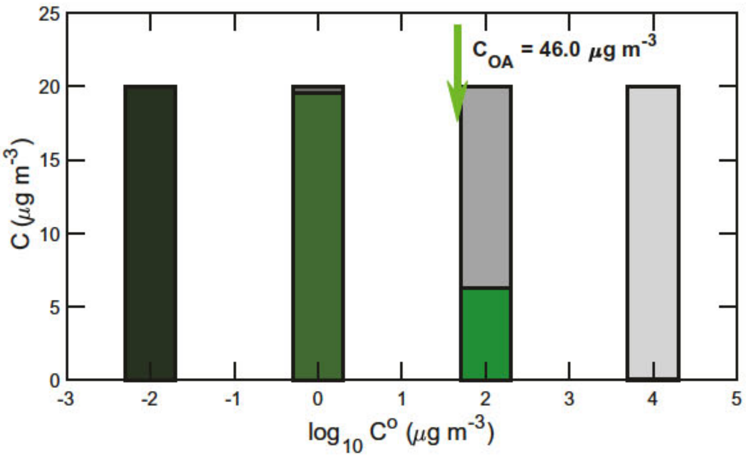

Fig. 4.12 Product distribution and equilibrium partitioning for an idealized experiment with organic products distributed evenly in four volatility bins, separated by a factor of 100 in volatility. Conditions shown are for an equilibrium with $10\,\mu\mathrm{g\,m^{-3}}$ of secondary organic aerosol (SOA). The condensed phase is indicated with shades of green and the vapor phase with shades of gray, as shown.

It is instructive for the four species to form a "gap" VBS with $C^{\mathrm{o}} = \{0.01, 1, 100, 10000\}\,\mu\mathrm{g\,m^{-3}}$, which we depict in Fig. 4.12 along with the expected equilibrium partitioning at the end of the production phase, where $C_{\mathrm{OA}} = 46\,\mu\mathrm{g\,m^{-3}}$, with a total concentration for each species of $20\,\mu\mathrm{g\,m^{-3}}$ and a production rate of $P_i^v = 0.25\,\mu\mathrm{g\,m^{-3}}$ $\mathrm{min^{-1}}$. In Fig. 4.12, we represent different volatilities with different color saturation. The least volatile species are the darkest, and the condensed phase is shown with greens while the vapor phase is shown with grays. We shall maintain this scheme throughout.

One of many useful timescales to consider in experimental design is the "saturation timescale," or how long it takes a given species to build up to a saturation ratio of 1. Under the conditions described here, the least volatile bin will saturate in $\Delta t = C_i^{\circ}/P_i = 0.01/0.25 = 0.04\,\mathrm{min} = 2.5\,\mathrm{s}$, meaning that its behavior will be essentially nonvolatile throughout the experiment. The second species will be saturated in 4 min, the third will have some partitioning into the condensed phase, and the fourth will have only a minimal condensed-phase fraction, serving almost as a passive tracer. It is also worth noting that for the low-volatility product in this example, with $P_i = 1\,\mu\mathrm{g\,m^{-3}\,min^{-1}}$, it will take approximately 1 min to build up $S_i^{\mathrm{xs,ss}}$; this confirms that the equilibration timescale for the system is $u^c = 1/(\alpha_i' \nu^c)$.

We shall assume that condensation to the suspended seeds begins rapidly. The purpose of the noninteracting seed is for condensation (formation of a condensed phase) to begin immediately once the least volatile species reaches saturation, without requiring any significant supersaturation; this is in contrast to nucleation experiments, where a large supersaturation ($S > 1000$) can be required to initiate condensation at a rate sufficient to measure in either the laboratory or the atmosphere.

In Fig. 4.13, we show results of a numerical simulation of Eq. (4.16) for both the gas and particulate phases in terms of both mass concentration and activity (saturation ratio or mass fraction). In these figures the y-axis is split, with the left-hand axis applying before dilution ($t < 0$) and the right-hand axis, scaled by the dilution factor of 100, applying after dilution ($t > 0$). The behavior of individual species (with different volatilities) is quite revealing, and the corresponding measurements (even for "volatility tracers") would be extremely useful. The recent application of high-sensitivity chemical ionization mass spectrometry has demonstrated the power of gas-phase and condensed-phase composition measurements.[5,7,59,76] Measurements of the transient vapor concentrations, C_i^v, can be a key diagnostic in SOA experiments, including for vapor wall losses[59] and also by forcing stepwise changes in seed condensation sinks.[7]

During the SOA production phase ($-100 < t < -20$ min), the gas-phase concentrations (Fig. 4.13a) of the relatively low-volatility products rise quickly to a roughly constant value and then stabilize or even decline slightly, whereas the gas-phase concentrations of the more volatile products rise steadily to much higher values (as a reminder, the production rates are all identical). Conversely, the condensed-phase concentrations (Fig. 4.13b) all show a similar functional form, with a nearly linear rate of increase, but the condensed-phase concentrations of the more volatile products lie well below those of the less volatile products. During the very earliest

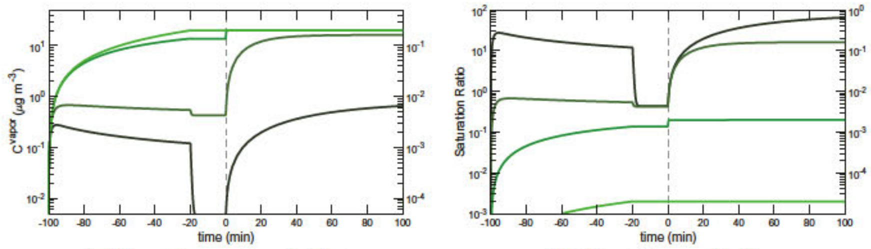

(a) Gas-phase concentrations. (b) Gas-phase activities.

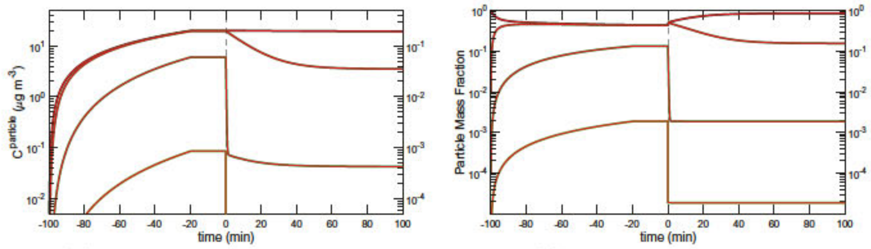

(c) Particle-phase concentrations. (d) Particle-phase activities.

Fig. 4.13 Model simulation of an idealized SOA experiment assuming an initial seed condensation sink of $1\,\mathrm{min}^{-1}$. Total production is $1\,\mu\mathrm{g\,m}^{-3}\ \mathrm{min}^{-1}$ from $t = -100$ to -20 min, according to the basis set in Fig. 4.12, and the curve shade indicates volatility, with darker shades being less volatile as indicated in that figure as well. At $t = 0$ min, indicated by a dashed vertical line, the system is diluted by a factor of 100. The left-hand y-axis applies to predilution conditions (negative time) while the right-hand y-axis applies to postdilution conditions (positive time). The left-hand panels show concentration while the right-hand panels show activity (saturation ratios for the gas phase, mass fractions for the particulate phase). The top panels show the gas phase, while the bottom panels show the particulate phase. The thin red curves within the shaded green curves indicate the ammonium sulfate (red) seed particles.

period of the experiment, the condensed-phase concentration of the $C^{\mathrm{o}} = 1\,\mu\mathrm{g\,m}^{-3}$ species lags that of the $C^{\mathrm{o}} = 0.01\,\mu\mathrm{g\,m}^{-3}$ species by a small amount, though it is unlikely that such a small and transient difference could be observed.

The activities in Fig. 4.13c and Fig. 4.13d complete the story. The gas-phase saturation ratio of the $C^{\mathrm{o}} = 0.01\,\mu\mathrm{g\,m}^{-3}$ species quickly reaches a value of roughly 30 and then slowly relaxes back toward 10 as the production period continues. It is thus significantly supersaturated throughout, though well below a typical critical value for significant nucleation — this is thus an example of a "well-designed" seed experiment that suppresses nucleation and forces all condensation to preexisting seed particles. The gas-phase saturation ratio of the $C^{\text{o}} = 1\,\mu\text{g}\,\text{m}^{-3}$ species also quickly reaches a constant value; but in this case, it is just under one, suggesting something closer to equilibrium behavior. In contrast, the gas-phase saturation ratios of the two more volatile constituents rise steadily throughout the experiment but stay well below one.

The particle-phase mass fractions (activities) in Fig. 4.13d also separate the two low-volatility products from the other two. The two low-volatility products quickly converge to mass fractions near 0.5 (they are produced at the same rate and dominate the particle composition), though the early transient is again evident. In contrast, the two more volatile species remain trace constituents with steadily rising mass fractions, though the $C^{\text{o}} = 100\,\mu\text{g}\,\text{m}^{-3}$ species eventually constitutes about 10% of the particle composition. The gas-phase and particle-phase activities of these two volatile species are nearly identical throughout the production period, showing that they both remain in equilibrium.

The 20-min relaxation period for $-20 < t < 0\,\text{min}$ is unremarkable from the point of view of the particle composition — the concentrations and activities simply stop rising. However, the gas-phase behavior is highly informative. After production stops, the concentrations of the two low-volatility products drop significantly, while the more volatile products barely register any change. Because production is driven in the gas phase in this simulation, that phase is most sensitive to dynamical delays. Further, it is the species with high steady-state saturation ratios that respond most dramatically to the sudden stop in production. Because the low-volatility vapors are in a steady state but far from equilibrium, their concentrations drop notably when production ceases, consistent with Eq. (4.53). This is most evident for the species with $C^{\text{o}} = 0.01\,\mu\text{g}\,\text{m}^{-3}$, whose gas-phase concentration drops by almost a factor of 100 when production ceases. The concentration falls to about $0.004\,\mu\text{g}\,\text{m}^{-3}$ because the condensed-phase mass fraction is about 0.4. On the other hand, the vapor concentration of the species with $C^{\text{o}} = 1\,\mu\text{g}\,\text{m}^{-3}$ also reaches a steady state during production but the concentration drops only modestly at $t = -20\,\mathrm{min}$ when production stops. The two more volatile species build up in the vapor phase and simply stop accumulating after production stops.

The change in gas-phase concentration through a rapid drop in the production rate is a very strong diagnostic of the volatility behavior of different species, in theory directly revealing the steady-state saturation ratio during the production phase; for OH photo-oxidation, this is straightforward — one simply turns off the lights. It is worth noting that this can also be used to measure the equilibration timescale of the system. If the collision frequency of the vapors with particles is known and if particle-phase diffusion limits (or slow chemistry) are not a factor, this then constrains the mass accommodation coefficient. In our simulation, $\alpha = 1$ and the condensation sink is high, so the relaxation is almost instantaneous.

The benefits of dilution are also evident in Fig. 4.13, especially considering the most volatile species as a passive tracer; the gas-phase concentration of that product drops by exactly the dilution factor (100) and so because the y-axis scales change by the same factor the concentration curve in Fig. 4.13a forms a horizontal line. After dilution, the two species with intermediate volatility evaporate, nearly matching the tracer concentration, while the concentration of the least volatile species slowly rises to near its saturation value ($C^{\mathrm{o}} = 0.01\,\mu\mathrm{g\,m^{-3}}$). The gas-phase concentrations of the two low-volatility products rise relatively slowly, whereas the $C^{\mathrm{o}} = 100\,\mu\mathrm{g\,m^{-3}}$ product jumps (flashes) to its steady value almost immediately. In Fig. 4.13, the y-axis shifts by a factor of 100 across the dilution step at $t = 0$ in all cases except the condensed-phase activity (mass fraction), where the scale does not change across the dilution step. Consequently, the postdilution activities in Figs. 4.13c and 4.13d can be compared directly, and it is evident that the activities in the two phases converge after the dilution step — almost instantly for the two more volatile products and more slowly for the less volatile products.

This final element demonstrates the difference between equilibration and evaporation timescales; the evaporation timescale for the species with $C^{\mathrm{o}} = 0.01\,\mu\mathrm{g\,m^{-3}}$ is roughly 100 h, yet it equilibrates along with the species with $C^{\mathrm{o}} = 1\,\mu\mathrm{g\,m^{-3}}$ in roughly 1 h. The behaviors are not identical because both the aerosol surface area and composition are changing as the particles shrink, but they are very similar. Modern chemical ionization mass spectrometers have the sensitivity required to observe this behavior; $C = 0.01\,\mu\mathrm{g\,m^{-3}}$ is roughly 1 pptv.[7]

Until very recently, the full behavior of these systems has been deduced from limited observations: precursor loss (ΔC_{prec}) and some measure of total organic aerosol production (ΔC_{OA}).[19,34,77] What we actually observe is aerosol growth. We observe this in three ways: growth of the integrated particle volume (mass); diameter growth; and growth in the organic aerosol to seed ratio, $\mathrm{OA:S} = C^s_{\mathrm{OA}}/C^s_{\mathrm{seed}}$.

$$\begin{aligned} -\Phi^{v,s}_p &= \underbrace{N^s_p\,\rho_{\mathrm{OA}}\,\frac{\mathrm{d}\,v^s_p}{\mathrm{d}t}}_{\text{total volume growth rate}} = N^s_p \times \underbrace{\rho_{\mathrm{OA}}\,\frac{\pi}{2}\,d^2_p\,\frac{\mathrm{d}\,d_p}{\mathrm{d}t}}_{\text{individual particle growth rate}} \\ &= \underbrace{\frac{\mathrm{d}(OA:S)_p}{\mathrm{d}t}}_{\text{bulk organic to seed ratio}} \times C^s_{\mathrm{seed},p} \qquad (4.54) \end{aligned}$$

This condensation almost never consists of a single compound (thus $\Phi^{v,s}_p$ and not $\Phi^{v,s}_{i,p}$), but in the idealized world of a monodisperse aerosol (a single value of p, especially with a passive seed) in theory, the net condensation to suspended particles should be readily observable. Furthermore, though the three measures are nominally equivalent, especially in this idealized example, they have very different sensitivities to external influences such as wall losses and can also be measured with different instruments. The total particle volume change is most directly measured with a scanning mobility particle sizer (SMPS), especially for a relatively broad particle size distribution; alternatively, the total particle mass can be measured with an aerosol mass spectrometer (AMS), a centrifugal particle mass analyzer (CPMA), or even a filter sample (OC:EC). The particle diameter change can again be measured with an SMPS, especially when the particle distribution is close to monodisperse, but as a

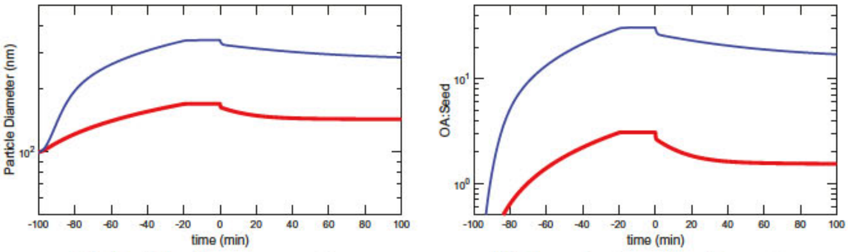

(a) Particle diameters vs time.

(b) Organic to seed ratios vs time.

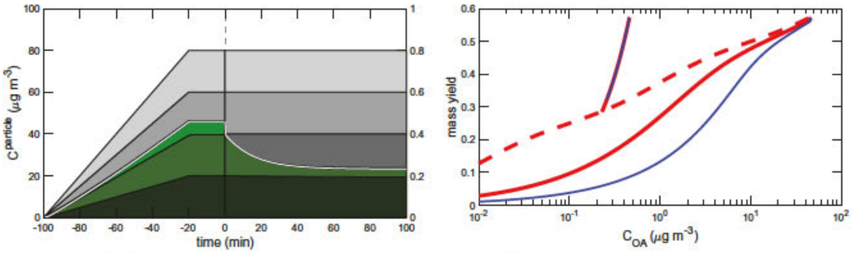

(c) Total concentrations.

(d) Condensed-phase mass yields.

Fig. 4.14 Model simulation of an idealized SOA experiment assuming an initial seed condensation sink of $\sim$1 min^{-1} (red) and $\sim$0.1 min^{-1} (blue). Total production is 1 μg m^{-3} min^{-1} from $t = -100$ to -20 min, according to the basis set in Fig. 4.12. At $t = 0$ min, the system is diluted by a factor of 100. (a) Particle diameters vs. time for the two seed concentrations — the lower number of blue seeds grow more. (b) Organic aerosol to seed mass ratio vs. time for the two cases — the lower number of blue seeds gain more mass. (c) Stack plot of all organic concentrations vs. time for the high-seed case with $C_{OA} = 47 \mu$g m^{-3} at maximum. Greens are condensed phase, grays are vapors. Darker shades are lower volatility as shown in Fig. 4.12. The left-hand y-axis applies for $t \leq 0$, the right-hand y-axis for $t \geq 0$ after dilution. (d) Traditional mass-yield "Odum" plot. Dynamic yields are solid curves while the equilibrium yields are the dashed curve.

differential (change in modal size, etc.) as opposed to an integral (total volume) quantity. Finally, the organic to seed mass ratio can be measured by an AMS without needing to know the particle collection efficiency.[78]

We show the reduced data quantities from the numerical simulation for this idealized experiment in Fig. 4.14, again with four panels. The first three panels show the three different quantities used to constrain the SOA mass flux and yields, while the final panel shows the associated dynamic and equilibrium mass yields. In Fig. 4.14, we plot results for the base-case ("high seed") model with a thick red curve (for nominal ammonium-sulfate seeds) and the results for the low-seed model with a thinner blue curve (for nominal ammonium nitrate seeds).

Figure 4.14a shows the simulated particle diameter and Fig. 4.14b shows the simulated OA:seed as a function of time. The y-axis in each case is logarithmic and the scale remains constant across the dilution step at $t = 0$ because both quantities are intrinsic to the particles. The dynamics are clearly evident, especially after the dilution step at $t = 0$ (where the equilibrium change is instantaneous). For both of these quantities, the low-seed (blue) case shows a larger change because with fewer particles the same total mass flux is concentrated on a smaller number of particles (by a factor of 10); consequently, OA:seed rises to a ten-fold higher value and the diameter change is 2.15 times larger for the high-seed (red) case. A major advantage of OA:seed is that this ratio can be measured with high precision using an AMS.[79] By measuring the concentration ratio on otherwise similar particles, the measurement also avoids complications associated with the particle collection efficiency (bounce), which can complicate absolute concentration measurements (especially in chamber experiments).[78,80] This is why in Eq. (4.54) we separate measurement of OA:seed from a potentially independent determination of $C^s_{\mathrm{seed},p}$. Another challenge for unspeciated measurement of the total diameter or volume change (measurements that do not separate organics from seeds) is that the measurement is intrinsically a difference; in this case the change from 100 nm. This would seem to put value on the low-seed case, where the diameter change (or even the OA:seed) is larger.

In Fig. 4.14c we show the total aerosol mass for the high-seed case alone, with the contributions from each bin plotted according to the VBS color scheme introduced in Fig. 4.12. Here the particle- and gas-phase compositions plotted in Fig. 4.13 are stacked to show the total concentrations in each phase on a linear scale; a thin white curve separates the particulate from the vapor phase. In this case we again employ the split y-axis with the post dilution left-hand axis applying after the dilution stage at $t = 0$. This is because the total suspended mass is an extrinsic quantity. After the dilution stage, the $C^{\mathrm{o}} = 100\,\mu\mathrm{g\,m}^{-3}$ product flashes from the particles immediately, while the $C^{\mathrm{o}} = 1\,\mu\mathrm{g\,m}^{-3}$ product evaporates over the course of about an hour.

Fig. 4.14d shows a logarithmic "Odum" plot of observed "dynamic" mass yield $F_{OA} = C_{OA}/\Delta C_{\mathrm{prec}}$ vs. the organic aerosol concentration, C_{OA}.[19,81,82] The dynamic yield curves start in the lower left, with low mass yields and low total aerosol, and progress diagonally to the upper right. We also show equilibrium mass yields from Eq. (4.51) with a dashed curve based on the instantaneous total product concentration. The dynamic yields significantly lag the equilibrium yield. In the "high-seed" case, the dynamic and equilibrium values converge at roughly $C_{\mathrm{OA}} \simeq 10\,\mu\mathrm{g\,m}^{-3}$; in the "low-seed" case, convergence occurs at $C_{\mathrm{OA}} \simeq 30\,\mu\mathrm{g\,m}^{-3}$. The high-seed convergence occurs after roughly 20 min in the simulated experiment, and for the next hour the system rises in roughly equilibrium toward a final yield of almost 0.6. In the low-seed case, convergence occurs much later, after almost an hour of SOA production, and the final relaxation toward equilibrium only occurs after the production halts, producing a small hitch in the dark green curve at the very highest values. The range between the two dynamic curves represents a typical range of seed condensation sinks in chamber experiments; the space between them as well as the space between any dynamic curve and the dashed equilibrium curve is due to an excess saturation of condensible organic vapors that will condense but are still in the gas phase at any given time (with a given measured amount of precursor consumption) simply because they have not had time to encounter a particle.

The dynamic yield curve in Fig. 4.14a shows the dilution step as a discontinuity. The factor of 100 dilution is evident in a sudden drop of C_{OA} from 46 to $0.046\,\mu\mathrm{g\,m}^{-3}$. The remaining particles are out of equilibrium and relax back to the dashed equilibrium curve over the next hour, leaving a nearly vertical trace; this is the opposite case to the delayed condensation. It is a useful check of the dynamical and equilibrium numerics that the two solutions ultimately converge.

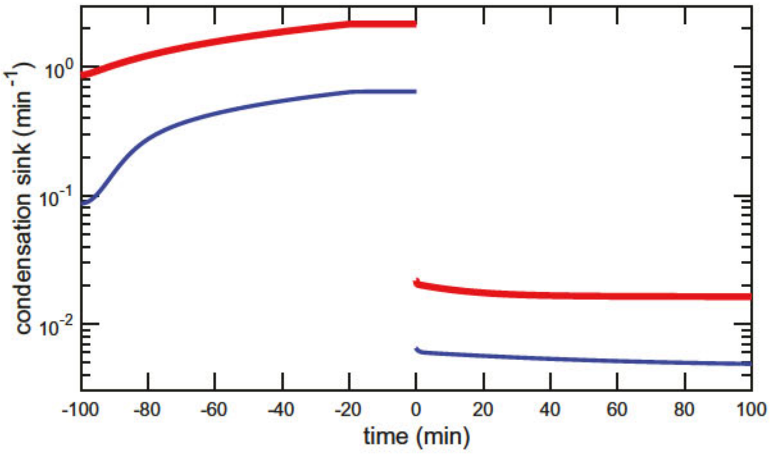

Fig. 4.15 Particle condensation sinks in an idealized SOA production experiment. Vapors are produced from -100 min $\leq t \leq -20$ min and there is a stepwise $\times 100$ dilution at $t = 0$.

It is also interesting that the low- and high-seed cases overlap, though in the low-seed case the condensation sink is so low that the system does not quite reach equilibrium even after 100 min.

We show the condensation sinks for the high- and low-seed cases in Fig. 4.15. The two cases are initially separated by a factor of 10 at about 0.1 and 1 per minute, but as condensation causes the particle surface area to increase, the condensation sinks also increase. Because the fewer particles in the low-seed case grow more, the values of the condensation sink in the two cases converge somewhat during production. After dilution, the high-seed condensation sink drops to 0.02 min^{-1} and organics with $C^{\mathrm{o}} = 100\,\mu\mathrm{g\,m^{-3}}$ (and an evaporation timescale of 0.5 min) flash from particles rapidly, while $C^{\mathrm{o}} = 1\,\mu\mathrm{g\,m^{-3}}$ organics reequilibrate with a 50-min timescale driven by the condensation sink. If the condensed-phase concentration of a species, C_i^s or indeed the partitioning $C_i^s/(C_i^s + C_i^v)$ were measured unambiguously, this dynamic behavior after a dilution step would be very informative.

The dynamics are most evident in Fig. 4.16, where we show the excess saturation ratios ($S_{i,p}^{v,s;\mathrm{XS}}$) in Eq. (4.37), including a Kelvin term with $d_{\mathrm{K10}} = 4.5\,\mathrm{nm}$). The least volatile species are out of

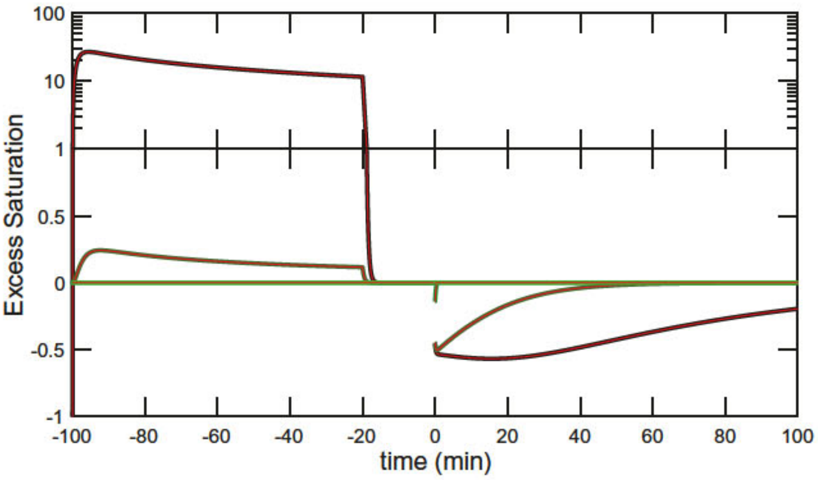

Fig. 4.16 Vapor excess saturation ratios in an idealized SOA production experiment. Vapors are produced from -100 min $\leq t \leq -20$ min and there is a stepwise × 100 dilution at $t = 0$. The y-axis is split between a linear range ($-1 \leq S_{i,p}^{v,s;\text{xs}} \leq 1$ and a logarithmic range ($S_{i,p}^{v,s;\text{xs}} > 1$).

equilibrium whenever there is a significant perturbation, with a sometimes very high excess saturation during production and a more modest negative excess saturation after dilution. When the excess saturation is greater than 1 the condensation is effectively "nonvolatile" because the condensed-phase activity has no influence over the dynamics, while when the excess saturation is near 0 the condensation is fully "semi-volatile" as with the $C^{\text{o}} = 100\,\mu\text{g}\,\text{m}^{-3}$ constituent. Because the condensation sink is of order $0.01\,\text{min}^{-3}$ after the dilution step, the least volatile $C^{\text{o}} = 0.01\,\mu\text{g}\,\text{m}^{-3}$ species remains significantly out of equilibrium for the entire 100 min, whereas the more volatile species relax according to their evaporation timescales (this includes a very brief period of disequilibrium for the $C^{\text{o}} = 100\,\mu\text{g}\,\text{m}^{-3}$ species, which has an evaporation timescale of roughly 10 s under these conditions and effectively flashes off of the particles).

This species with $C^{\text{o}} = 100\,\mu\text{g}\,\text{m}^{-3}$ reveals the physics underlying the rising yields described by Odum *et al.*[34] In the model system we are simulating here, the semi-volatile species is never a major constituent of the particles, but it does eventually contribute 10% of the particle composition at the end of the production phase (at $t = -20\,\text{min}$). However, it can only do this when the saturation ratio rises sufficiently, as seen in Fig. 4.13c, though its excess saturation ratio never deviates significantly from zero (it is always effectively in equilibrium). Because of the high volatility, this takes a long time and consequently later on during the simulated experiment the aerosol mass yields rise. This is why mass yields increase as the total aerosol mass also increases; any element of an experiment that interferes with this vapor buildup (e.g., irreversible wall loss[57–59]) will thus short-circuit the contribution of semi-volatile species to the condensed phase.

All in all, this simulation shows that even an idealized SOA formation experiment deviates significantly from equilibrium behavior for a long time, taking between 30 and 60 min to approach a nominal equilibrium state. This alone would lead to significant underestimation of SOA mass yields during "dynamic yield" experiments, as has been shown in comprehensive simulations as well.[26] However, complementary measurements of gas-phase concentrations would significantly augment the experiments, provided the instruments had a sufficiently fast time response.[59] Measurements of the condensed-phase composition, or the concentration ratios between the gas and condensed phases, would also enhance the experiments.

4.3.3.2. *Organic Aerosol Mixing*

A second type of experiment we have developed to probe the volatility of organic aerosol mixtures is to form two separate aerosol suspensions ($p = 1$ and $p = 2$), often on different identifiable seed types. We form the organic aerosol either from chemically distinct precursors or materials (systems with easily separated mass spectra) or from isotopomers of the same precursor (i.e., H- and D-substituted precursors, or ^{12}C- and ^{13}C-substituted precursors). These experiments rely on quantitative single-particle mass spectrometry, such as with light-scattering single-particle AMS (LSSP AMS)[83,84] or event triggering AMS,[85] where the original population (often based on

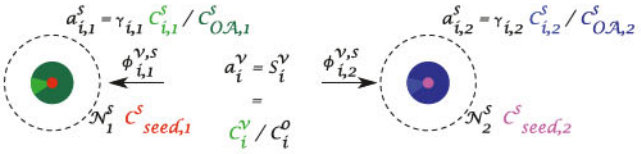

Fig. 4.17 Fluxes between two suspended-particle populations ($p = 1, 2$) and the vapor phase during a particle mixing experiment. The populations are distinguished by different seeds (red and magenta) and are coated with organics that may have different isotopic composition (green and blue). Species i will have a single gas-phase activity $a^v_i = C^v_i / C^o_i$ and consequently the activities in the two populations $a^s_{1,i}$ and $a^s_{2,i}$ will relax toward an equilibrium with $a^s_{1,i} = a^v_i = a^s_{2,i}$.

the seed signature) can be determined for each particle and then individual particle mass spectra can be averaged within time windows to improve signal to noise.

Following the combination of two populations, the vapors around them will establish a steady-state saturation ratio, governed by a flux balance between the two populations illustrated in Fig. 4.17, on a timescale equal to roughly the sum of the two suspended condensation sinks: $\Phi^{v,c}_{i,1} = -\Phi^{v,c}_{i,2}$. Consequently

$$\begin{aligned} k^s_{1,\mathrm{cond}}[C^v_i - a^s_{i,1}\, C^o_i] &= -k^s_{2,\mathrm{cond}}[C^v_i - a^s_{i,2}\, C^o_i] \\ S^{\mathrm{ss}}_i = \frac{C^{v,\mathrm{ss}}_i}{C^o_i} &= \frac{k^s_{1,cond}\, a^s_{i,1} + k^s_{2,cond}\, a^s_{i,2}}{k^s_{1,cond} + k^s_{2,cond}} \end{aligned} \tag{4.55}$$

This is the condensation-sink weighted average of the activities; it is easily understood for a case where the two condensation sinks are the same and the populations start isotopically pure, so $a^s_{i,1}(t=0) = a^{s,0}_{i,1}; a^s_{i,2}(t=0) = 0$. The vapor saturation ratio will drop to $0.5 \cdot a^{s,0}_{i,1}$ and stay there while the activities in the two condensed phases relax toward that value in equal measure over time.

The simplest form of mixing experiments are those in which the composition and concentrations of the two populations are initially identical, either through injection of a preformulated mixture or identical production of SOA. In that case a constant-pressure injection of one population into the other (either by withdrawing a small amount of the initial population or by expanding the overall volume) will not perturb the overall equilibrium between the total concentration of the vapor and condensed phases. Entropy, however, will still drive mixing.

Here we shall model that case, where two otherwise identical populations are composed of isotopologues of each other. Specifically, we shall model the "gap" VBS discussed above, in which we imagine two SOA populations are grown in separate chambers just as before, but using isotopically distinct precursors. In this case, it is self-evident that all isotopologues should progress toward an equilibrium ratio in each particle equal to the relative suspended volumes (mass concentrations) of the two labeled populations. For example, if equal volumes are intermingled (say $5\,\mathrm{m}^3$ containing $40\,\mu\mathrm{g\,m}^{-3}$ from each population), then each particle will ultimately contain equal fractions of each labeled constituent, while if volumes are intermingled with a 99:01 ratio (say 100 L containing $40\,\mu\mathrm{g\,m}^{-3}$ of "probe" aerosol added to $9.9\,\mathrm{m}^3$ containing $40\,\mu\mathrm{g\,m}^{-3}$ of "chamber" aerosol), then the "chamber" (major) particles should contain 1% of the minor population, and the "probe" (minor) particles should contain 99% of the major population. It is also evident that the relevant timescale for this equilibration should be a function of the evaporation, the condensation, and the diffusion timescales; the intermixing cannot occur until a constituent evaporates fully from a particle, but it also cannot occur until the resulting vapor finds and diffuses into other particles. Very volatile compounds have high gas-phase concentrations and are largely unaffected by the particle phase. They will thus equilibrate with the evaporation timescale provided they can diffuse into particles. Conversely, very low-volatility compounds have high condensed-phase fractions and even though their evaporation timescales are long, only a small portion needs to evaporate for the system to equilibrate (again provided they can diffuse out of or into particles). In this case, the condensation sink defines the equilibration timescale.

In Fig. 4.18, we show theoretical concentrations for an idealized mixing experiment in which equal mass concentrations ($40\,\mu\mathrm{g\,m}^{-3}$) of the same SOA system are intermingled. In this case, one population is prepared with an isotopic label (i.e., ^{13}C).[83,86] This simulates the

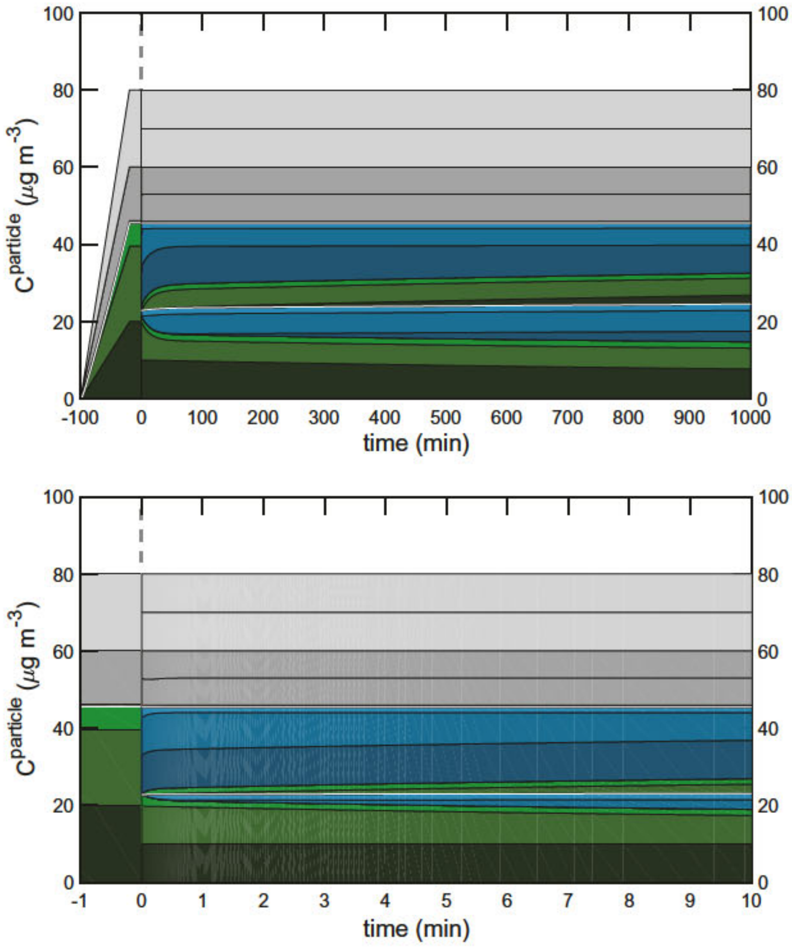

Fig. 4.18 Idealized SOA mixing experiment. Total production is $1\,\mu\mathrm{g\,m}^{-3}\ \mathrm{h}^{-1}$ from $t = -100$ to -20 min, split evenly between $C* = \{0.01, 1, 100, 10^4\}\mu\mathrm{g\,m}^{-3}$ for two different sets of isotopomers. At $t = 0$ min, the two populations are interchanged with a 50:50 proportion. (a) Stack plot of all organics. Greens are condensed phase, blues are condensed phase of isotopically labeled species (after mixing), grays are vapors. Condensed organics are colored for only one seed population (originally green) for clarity; the population of the originally blue "isotopomers" are kept white for clarity. They are a mirror image of the green population. Darker shades are lower volatility. (b) Zoomed plot for 1 min before and 10 min after mixing.

single-particle mixing experiments we have been conducting.[83–85,87] We grow one SOA population on 50 nm seed particles and one on 200 nm seed particles to include the effect of differing condensation sinks as well as a slight influence from the Kelvin term due to the different final particle diameters. At $t = 0$ min, we simulate a 50:50 interchange of these two populations (suspended particles and vapors). We dilute each population by a factor of two and then combine them. The compounds initially on population $p = 1$ (red seeds) are shown in shades of green, while the isotopologues initially on population $p = 2$ (blue seeds) are shown in shades of turqouise. After the intermingling at $t = 0$, we show first the condensed-phase species on population 1, $C^s_{i,1}$, which start as all green but gradually become progressively half turquoise, and second the condensed-phase species on population 2. We separate the two populations with a thin white curve. We show the gas-phase concentrations of each volatility class with the same shade of gray, so that, e.g., the most volatile (lightest gray) constituent, with $C^v_4 = 20\,\mu\mathrm{g\,m^{-3}}$ just before intermingling consists of two isotopically labeled constituents, each with $C^v_4 = 10\,\mu\mathrm{g\,m^{-3}}$ just afterwards. The top panel shows a full 1000 min simulation and the lower panel zooms into $-10 \leq t \leq 10\,\mathrm{min}$. The difference in particle sizes causes the slight perturbation in the semi-volatile vapors (medium gray) visible in the zoomed panel, and the small effect of the Kelvin term causes the larger ($p = 1$) population to grow slowly at the expense of the smaller population.

During the mixing simulation, there is almost no change in diameter for either seed population (1 and 2), as the system is in equilibrium with respect to net condensation other than the Kelvin difference, even while the isotopomers mix via gas-phase exchange. The initial (pre-intermingling) SOA concentration is $C^s_{\mathrm{OA},1} \simeq 45\,\mu\mathrm{g\,m^{-3}}$. After $t = 0$, each population maintains a mass $C^s_{\mathrm{OA},i} \simeq 22.5\,\mu\mathrm{g\,m^{-3}}$, so the total SOA remains the same. The gas-phase activity of every species quickly drops to half its premingling value at $t = 0$ and remains there (i.e., the equilibrium activity as the system has been diluted by a factor of two without changing the overall organic mass).

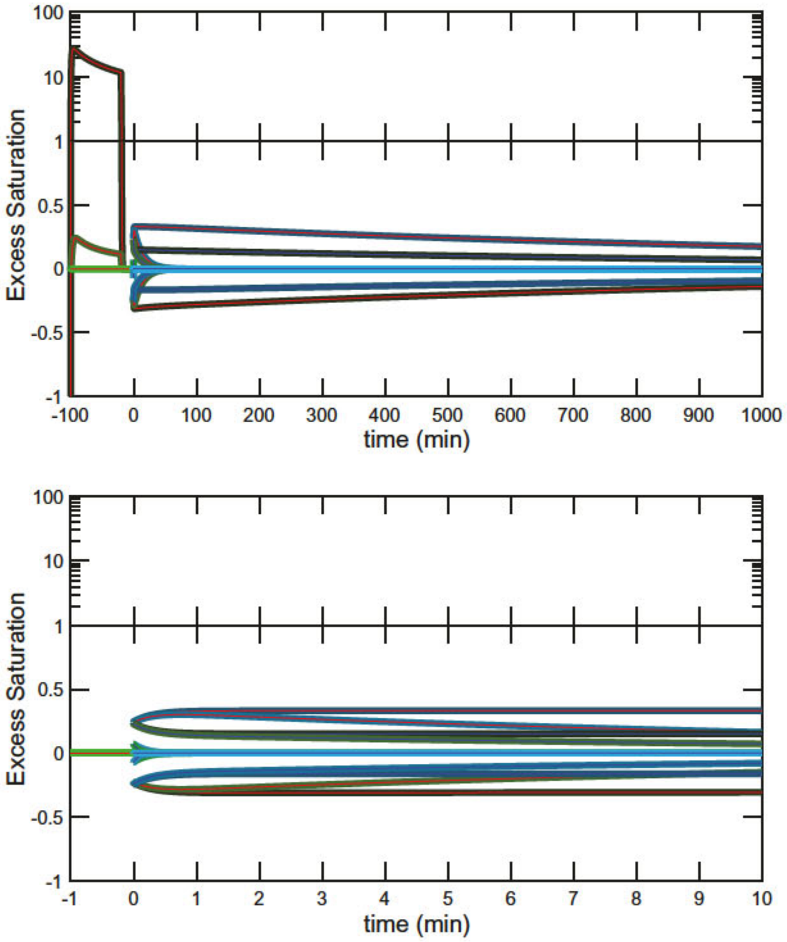

Fig. 4.19 Vapor excess saturation ratios in an idealized SOA mixing experiment. Vapors are produced from -100 min $\le t \le -20$ min and there is a 50:50 mixture at $t = 0$ with two populations identified by the thin red and blue curves within the curve representing each organic species. The y-axis is split between a linear range ($-1 \le S_{i,p}^{v,s;\mathrm{xs}} \le 1$ and a logarithmic range ($S_{i,p}^{v,s;\mathrm{xs}} > 1$). The lower panel zoom in on the time interval around the mixing event ($-1 < t < 10$ min).

In Fig. 4.19, we show the excess saturations for this mixing experiment, with the full time range in the top panel and a zoomed range below. For $t < 0$, we show only the chamber population, and the values are identical to the case discussed earlier. After 50:50

intermingling, the two populations are driven out of equilibrium symmetrically: the particles find themselves with a surfeit of their "own" isotopologue and a deficit of the opposing isotopologue, and so the excess saturations are offset symmetrically from $S^{\mathrm{XS}} = 0$. These values relax toward zero according to the evaporation timescales. In addition, the different condensation sinks cause a short-term excursion visible in the zoomed panel, with the (blue) particles with the higher condensation sink absorbing (or evaporating) semi-volatile constituents more rapidly. Finally, there is a very slight asymmetry due to the Kelvin term.

The timescales probed by the mixing experiments are thus the evaporation timescales we show in Fig. 4.10. The $C^\circ = 100\,\mu\mathrm{g\,m^{-3}}$ species exchanges in less than 1 min, the $C^\circ = 1\,\mu\mathrm{g\,m^{-3}}$ species in about half an hour, and the $C^\circ = 0.01\,\mu\mathrm{g\,m^{-3}}$ species takes more than 1 day. This is completely consistent with, e.g., the slow but steady exchange of squalane isotopomers described by Robinson *et al.*[83] Specifically, the species with $C^\circ = 1\,\mu\mathrm{g\,m^{-3}}$ will have an evaporation timescale of roughly 0.5 h from nearly 150 nm diameter particles, while the species with $C^\circ = 100\,\mu\mathrm{g\,m^{-3}}$ will have an evaporation timescale of only 15 s. Finally, the least volatile species with $C^\circ = 0.01\,\mu\mathrm{g\,m^{-3}}$ has a timescale of 30 h and has only begun to exchange at the end of the 1000 min simulation. Thus, without diffusion limitations within particles, these mixing experiments conducted in typical chambers will be able to classify species into three broad categories: low-volatility species with $C_i^\circ \lesssim 0.1\,\mu\mathrm{g\,m^{-3}}$ will show almost no exchange during these mixing experiments; semi-volatile species with $C_i^\circ \simeq 1\,\mu\mathrm{g\,m^{-3}}$ will exchange on timescales ranging from a fraction of an hour to several hours; relatively volatile species with $C_i^\circ \gtrsim 10\,\mu\mathrm{g\,m^{-3}}$ will exchange "instantaneously" on a timescale limited by the mixing time and condensation sink of the experiment. Fortunately (because the experimental timescale is near the atmospherically relevant timescale), this is exactly the separation that is most useful for atmospheric applications.

In Fig. 4.20, we show the composition of the two populations, displaying only the mass fraction of the "foreign" isotopologues, along with the composition of the chamber particles for $t < 0$. Thus

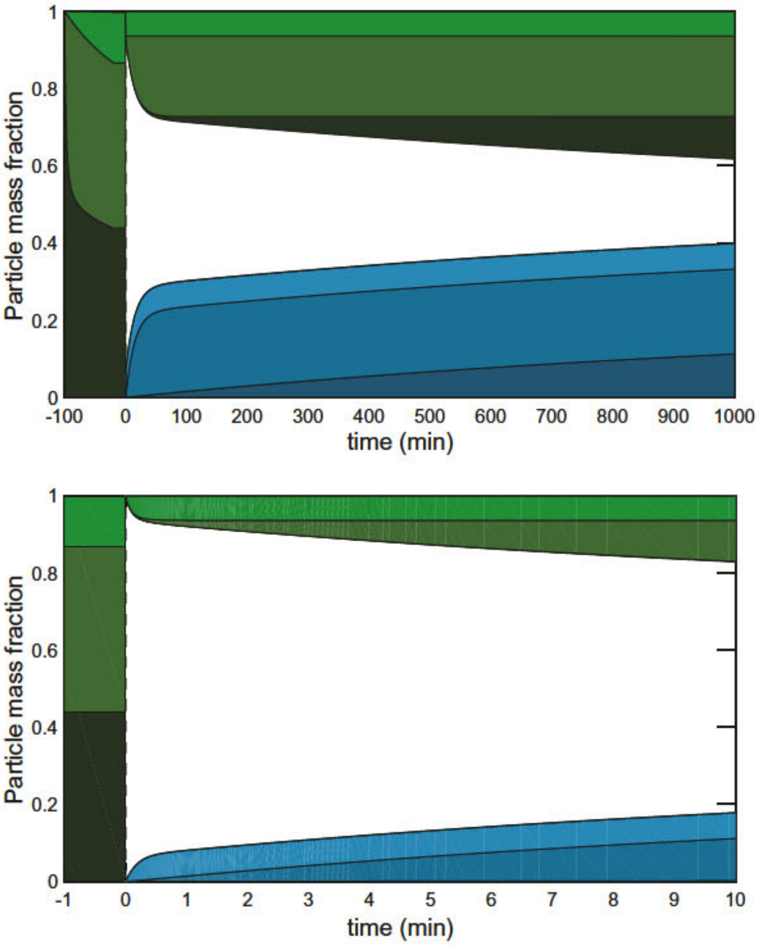

Fig. 4.20 Idealized SOA mixing experiment. Total production is $1\,\mu\text{g}\,\text{m}^{-3}\,\text{h}^{-1}$ from $t = -100$ to -20 min, split evenly between $\text{C}^* = \{0.01,\ 1,\ 100;\ 10^4\}$ $\mu\text{g}\,\text{m}^{-3}$ for two different sets of isotopomers. At $t = 0$ min, the two populations are interchanged with a 50:50 proportion. (a) Stack plot of all organics. Greens are condensed phase, blues are condensed phase of isotopically labeled species (after mixing), grays are vapors. Condensed organics are colored for only one seed population (originally green) for clarity; the population of the originally blue "isotopomers" are kept white for clarity. They are a mirror image of the green population. Darker shades are lower volatility. (b) Zoomed plot for 1 min before and 10 min after mixing.

the "chamber" particles gradually gain turquoise "probe" vapors while the "probe" particles gradually gain green "chamber" vapors over time. This is the same form of display we use for single-particle mass spectrometer data.[84,85,88] This emphasizes the three timescales driven by different volatility: nearly instantaneous uptake of volatile species, gradual exchange of semi-volatile species, and very slow exchange of low-volatility species.

4.4. Particle Microphysics

With the condensation dynamics described from the point of view of (moving) particle populations, we now need to consider the full set of microphysical constraints on a distribution of particles. As with many transport problems, the moving, Lagrangian, description following the growth of particles is more natural for a single, isolated system but a fixed, Eulerian, description is more suited to mixing between volumes as well as systems with sources such as nucleation or particle emission. Consequently, we shall now describe particle microphysics for fixed size distributions, again focusing on a very wide range of sizes in order to connect new-particle formation as well as a full range of particle growth and loss.

At each stage of this presentation, we are simplifying the representation of organic compounds and increasing the complexity of the microphysics. Initially, we described a full 2D-VBS in a chemical mechanism, then we considered only net condensation to a single particle population using a 4-bin 1D-VBS, and now we shall consider a full particle size distribution with only a single organic and two inorganic constituents.

4.4.1. *Geometric Definitions*

4.4.1.1. *Monodisperse Particles*

A particle in population p, shown in Fig. 4.21, will contain a total mass m_p, distributed among several constituents i according to mass fractions $f_{i,p}$. The particle may contain more than one condensed phase h with individual masses m_p^h, densities ρ_p^h, and constituent

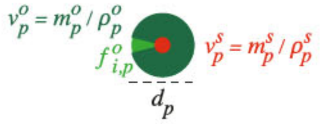

Fig. 4.21 Size, mass, and volume definitions for a particle with two condensed phases (organic, $h = \mathrm{o}$, and seed, $h = \mathrm{s}$).

mass fractions $f_{i,p}^h$. In most cases, there will be either one or two phases represented, but two represents the typical experimental situation in which a condensation seed is used to help track the evolution of particles. In the atmosphere, fine particles are thought to commonly contain at least a fairly hydrophobic (organic) and a hydrophilic (aqueous) phase, and larger particles may have a mineral or refractory phase(s).

Each phase will have a volume $v_p^h = m_p^h / \rho_p^h$ for a total volume

$$v_p = \sum_h v_p^h = \sum_h \frac{m_p^h}{\rho_p^h}; \quad m_p = \sum_h m_p^h. \tag{4.56}$$

There are many possible size parameters but we shall use the spherical equivalent diameter in Eq. (4.18). This size parameter may change with time, given by a growth rate $g_p = \mathrm{d}\, d_p / \mathrm{dt}$:

$$\begin{aligned} g_p &= \frac{1}{3} \sqrt[3]{\frac{6}{\pi}} \frac{1}{v_p^{2/3}} \frac{\mathrm{d}\, v_p}{\mathrm{dt}} = \frac{1}{3} \sqrt[3]{\frac{6}{\pi}} \frac{1}{v_p^{2/3}} \sum_h \sum_i \frac{\mathrm{d}}{\mathrm{dt}} \frac{m_{i,p}^h}{\rho_p^h} \\ &= \frac{1}{3} \sqrt[3]{\frac{6}{\pi}} \frac{1}{v_p^{2/3}} \sum_h \frac{1}{\rho_p^h} \sum_i \left(\frac{\mathrm{d}\, m_{i,p}^h}{\mathrm{dt}} - \frac{m_{i,p}^h}{\rho_p^h} \frac{\mathrm{d}\, \rho_p^h}{\mathrm{dt}} \right). \end{aligned} \tag{4.57}$$

Aside from the vexing issue of potential changes to the phase density ρ_p^h, assuming that the net mass flux to the particle p, given by $\mathrm{d}\, m_p^h / \mathrm{dt}$, is driven at any given time by net condensation into only a single phase. If we know the net flux per unit particle surface area ϕ_p^h, then $\mathrm{d}\, m_p^h / \mathrm{dt} = \phi_p^h \, s_p$. The term s_p is the individual particle surface area, which given a shape factor q_p is related to the spherical equivalent particle surface area by:

$$s_p = q_p \, \pi d_p^2 = q_p \, \sqrt[3]{\pi} \, (6 \, v_p)^{2/3}. \tag{4.58}$$

All told, this means the growth rate is related to the flux per unit surface area by:

$$g_p = 2 \, q_p \sum_h \frac{\phi_p^h}{\rho_p^h}. \tag{4.59}$$

From this, we can relate the rate of change of the particle diameter (size parameter) to the net condensation flux to the particle. This growth rate and net condensation flux, along with the integrated net condensation flux (total mass growth) of the entire particle ensemble, are generally the most important quantity to be derived from organic aerosol experiments.

An important caveat is that so far we are representing the flux to (and from) the particle surface and implicitly assuming rapid mass transport within the particle — including between phases. Fluxes are driven by activity gradients and so we are implicitly representing the *surface* activity with the mass fractions f_p^h and assuming for the time being that surface and bulk activities within all of the phases equilibrate rapidly compared with other changes in the population.

4.4.1.2. *Polydisperse Particles*

The flux considerations describe how the size of an individual particle changes in a Lagrangian frame of reference following the particle population, but in general, we observe a distribution of particles at fixed sizes and the evolution of that distribution in an Eulerian sense, with the size parameter d_p as an independent variable.

Given the infinite number of potential populations, we can represent particles as an ensemble of populations p that are each internally mixed, each containing some number concentration N_p as shown in Fig. 4.22. If the properties vary smoothly, this would constitute a continuous number size distribution of particles integrating to number N per unit volume (# cm^{-3}),

$$n_N = \frac{dN}{d\,d_p}; \quad n_N^\circ = \frac{dN}{d\log_{10} d_p} = \ln(10)\, d_p \, n_N, \tag{4.60}$$

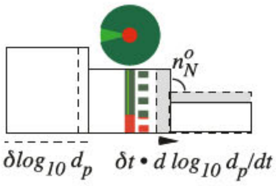

Fig. 4.22 Sectional representation of particle size distribution n_N° in $\log_{10} d_p$ coordinates, including growth rate.

separated by some spacing δd_p or $\delta \log_{10} d_p$. Because of the enormous dynamic range of particle sizes, we almost always use the logarithmic distribution, as depicted in Fig. 4.22. In a logarithmic distribution, the bin $p + 1$ is larger than the bin p by a factor:

$$d_{p+1} = d_p \times 10^{\delta \log_{10} d_p}. \tag{4.61}$$

There are several options to numerically representing the discretized distribution in a sectional algorithm, including allowing the sections to move (d_p will grow and shrink with the particle) and treating several moments (number, mass, etc.). For various reasons, we shall consider a succession of monomodal populations at discrete values of $\log_{10} d_p$ separated by even intervals of $\delta \log_{10} d_p$, using the index p. Formally, the number of particles in each bin is:

$$N_p = \int_{\log_{10} d_p - \frac{1}{2}\delta \log_{10} d_p}^{\log_{10} d_p + \frac{1}{2}\delta \log_{10} d_p} n_N^\circ \, d \log_{10} d_p'. \tag{4.62}$$

In a single moment algorithm, we can either assume that n_N° is constant across the interval or that a single mode exists at the center (this is our assumption). In either case,

$$N_p = n_N^\circ \, \delta \log_{10} d_p. \tag{4.63}$$

and we can represent the bin in a numerical scheme by either the total number N_p or the distribution n_N°.

However, these are *not* equivalent. The total volume in the section is

$$V_p = \frac{\pi}{6} \int_{\log_{10} d_p - \frac{1}{2}\delta \log_{10} d_p}^{\log_{10} d_p + \frac{1}{2}\delta \log_{10} d_p} n_N^\circ \, d_p'^3 \, d \log_{10} d_p'. \tag{4.64}$$

While for the central monodisperse case, this is exactly $V_p = (\pi/6)\, d_p^3$, it is larger for the constant case.

4.4.1.3. *Redistributing Particles*

When particles grow at a growth rate g_p for a time interval δt, they will move by $\Delta d_p = g_p\, \delta$t. However, our sectional distribution is based on a $\log_{10}$ coordinate and so both the distribution, n_N^{o}, and the growth rate must be represented with that ordinate:

$$g_p^{\text{o}} = \frac{\mathrm{d}\log_{10} d_p}{\mathrm{dt}} = \frac{1}{\ln(10)}\frac{1}{d_p}\frac{\mathrm{d}\, d_p}{\mathrm{dt}} = \frac{g_p}{\ln(10)\, d_p}, \tag{4.65}$$

and the growth will be by an amount $\Delta \log_{10} d_p = g_p^{\text{o}}\, \delta t$. In words, the *fractional* growth of very small particles for a given linear growth rate is very much larger than that of larger particles.

As depicted in Fig. 4.22, growth by $\Delta \log_{10} d_p$ will sweep out an area $\delta N_p = -n_{N,p}^{\text{o}}\, \Delta \log_{10} d_p$, acting as a sink of particles from the bin. The number fraction of the total particles lost to the larger bin will be $f_{p+} = \Delta \log_{10} d_p / \delta \log_{10} d_p$. This loss in turn will be a source of particles to the neighboring bin $+n_{N,p+1}^{\text{o}} = \delta N_p / \delta \log_{10} d_p$, which by definition will conserve the total particle number. However, growth is driven by a flux of mass, which depends on d_p^3; if we simply redistribute the particle number to a larger bin, this will not conserve mass.

This is an instance of a more general occurrence for sectional representations, where some number of new particles N_p appears at some size d_{pn} between two designated sizes d_{p-} and d_{p+}. To preserve the sectional representation, the particles must be distributed between the two sizes, and almost without fail, the proper approach is to conserve mass. In this case, using a monodisperse representation, the "new" particles are the entire number N_p, which have grown by an amount $\Delta \log_{10} d_p$ as shown in Fig. 4.22. Some fraction χ_{p+} will move (grow) to the larger bin, while the remainder $\chi_{p-} = 1 - \chi_{p+}$ will move to (remain in) the smaller bin. To conserve mass (volume), the redistribution is given by the cube of the diameters:

$$\chi_{p+} = \frac{d_{pn}^3 - d_{p-}^3}{d_{p+}^3 - d_{p-}^3} = \frac{d_{pn}^3/d_{p-}^3 - 1}{d_{p+}^3/d_{p-}^3 - 1} \tag{4.66}$$

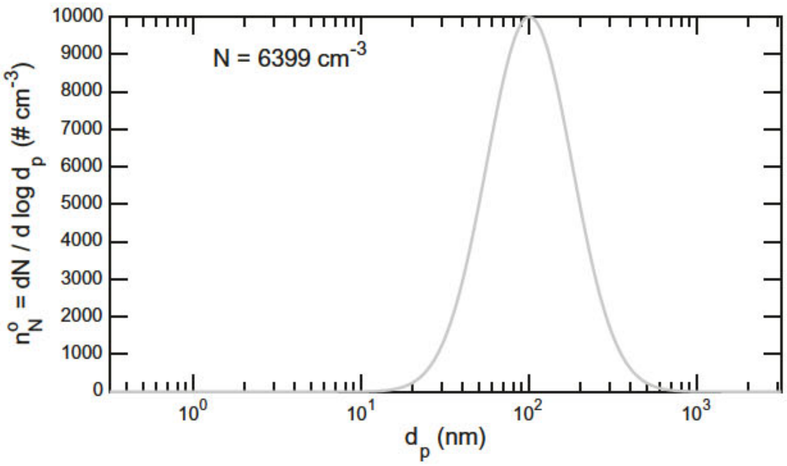

Fig. 4.23 Number distribution n°_N for a lognormal size distribution centered at 100 nm spherical equivalent diameter.

For a single-moment algorithm such as we are using, this redistribution causes numerical diffusion.[89]

4.4.2. *Particle Size Distributions*

To illustrate conditions typical of smog-chamber experiments, we shall consider a lognormal distribution of particles shown in Fig. 4.23:

$$n^\circ_N = A \exp\left(-\frac{(\log_{10} d_p - \log_{10} d_p^{\max})^2}{2\log_{10}^2\sigma}\right), \qquad (4.67)$$

with $A = 10000$, $\sigma = 1.8$, and the number mode $d_p^{\max} = 100\,\text{nm}$. The integral is $N = \sqrt{2\pi}\,A \log_{10}\sigma = 6399\,\text{cm}^{-3}$, which agrees with the numerical integral as shown in the figure. It is important to be able to visually integrate these distributions. The reason for the $d\log_{10} d_p$ in the abscissa is for the visual area of the distributions plotted in semilog x space to be proportional to the integral property — total number in this case. Peaks are roughly triangular, with area $\mathcal{A} = 1/2\,b \times h$. The height h is the peak, so $h = 10000$. The base is the rough basal width, *in decades*, extending the roughly linear sides of the peak function down to the baseline, so $b \simeq 1.1$ in this case. Thus the integral is roughly $\mathcal{A} \simeq 5500$ # cm^{-3}. This usually gets within about 10% or so.

Our size parameter is a volume equivalent diameter rooted in particle mass and so we can convert the number size distribution to a volume and then a mass distribution, shown in Fig. 4.24 for this simple lognormal number distribution

$$n_V^{\mathrm{o}} = \frac{\pi}{6}\, d_p^3\, n_N^{\mathrm{o}}. \tag{4.68}$$

One caveat in the conversion is that it is conventional to report aerosol number concentrations in # per cm^3, but most other aerosol quantities are reported per m^3. The easiest way to report the volume concentration is $\mu\mathrm{cm}^3\,\mathrm{m}^{-3}$; for a density of $\rho = 1\,\mathrm{g\,cm}^{-3}$, this converts directly to $\mu\mathrm{g\,m}^{-3}$. Here, we show a mass distribution $n_M^{\mathrm{o}} = \rho\, n_V^{\mathrm{o}}$ for a constant density of $\rho = 1.77\,\mathrm{g\,cm}^{-3}$, typical of ammonium sulfate seeds. Note that d_p is the physical (spherical equivalent) diameter of the particles, and so the mobility diameter d_{mob} will depend on the density, the shape factor q_p, and also collisional interaction factors for small particles that add approximately 0.3 nm to the mobility size for neutral particles.

We also want to know the surface-area distribution:

$$n_S^{\mathrm{o}} = \pi\, q_p\, d_p^2\, n_N^{\mathrm{o}}, \tag{4.69}$$

but once again we need to be careful about the desired units. In this case, we are interested in surface area because things bump into that surface area at some speed, typically in $\mathrm{m\,s}^{-1}$, and if we know the surface area per unit volume in $\mathrm{m}^2\,\mathrm{m}^{-3}$, then multiplying by that speed will give us the collision frequency of molecules with surface area, s^{-1}. The surface-area distribution for the fairly broad number size distribution we are using as an example case is shown in Fig. 4.25. Whereas the peak (mode) of the mass and volume distributions were at roughly 300 nm (for the number distribution peaked at 100 nm) the surface-area distribution peaks at about 200 nm.

4.4.2.1. *Sectional Numerical Representation*

For examples in this work, we shall implement a high-resolution single-moment sectional algorithm illustrated in Fig. 4.22, with

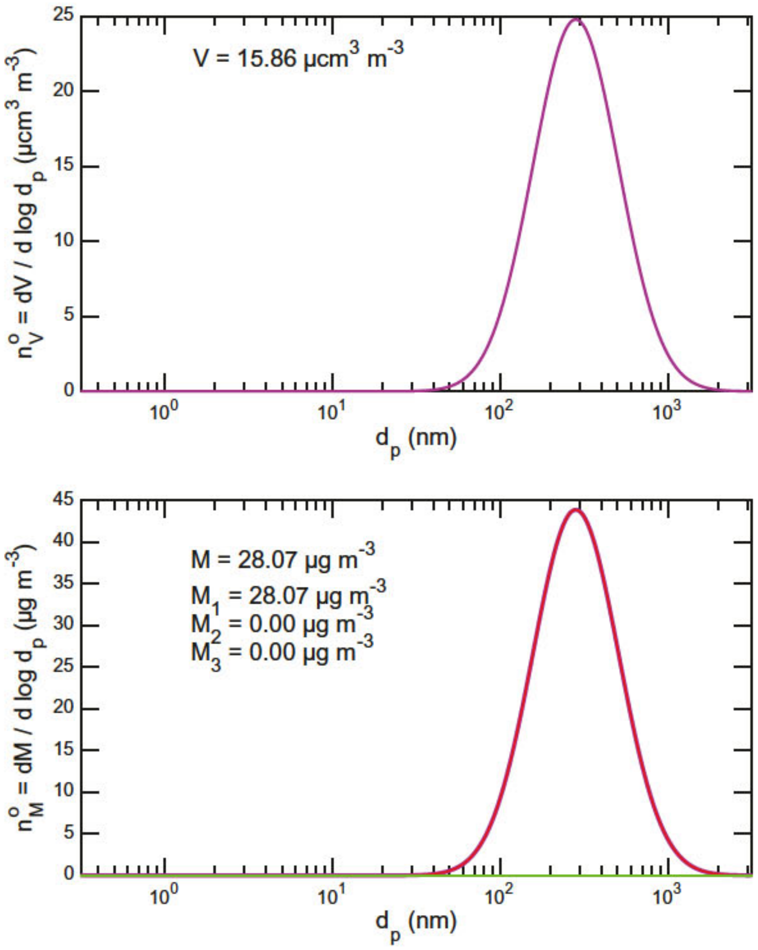

Fig. 4.24 Volume distribution, n_V°, (top) and mass distribution, n_M° (bottom) for a lognormal number size distribution of $1.77\,\mathrm{g\,cm^{-3}}$ particles centered at 100 nm. Mass is shown for three constituents, ammonium sulfate (M_1, red), ammonium nitrate (M_2, blue), and organics (M_3, green), in this case for pure ammonium sulfate. For this broad distribution, the volume and mass modes are shifted to nearly 300 nm.

discrete values of spherical equivalent diameter $\log_{10} d_p$ separated by $\delta \log_{10} d_p = 0.01$. We shall consider a wide range containing 401 bins with $0.3 \le d_p \le 3000\,\mathrm{nm}$, i.e., $0.5 \le \log_{10}(d_p/\mathrm{nm}) \le 3.5$. The smallest "particles" in this distribution are almost certainly free

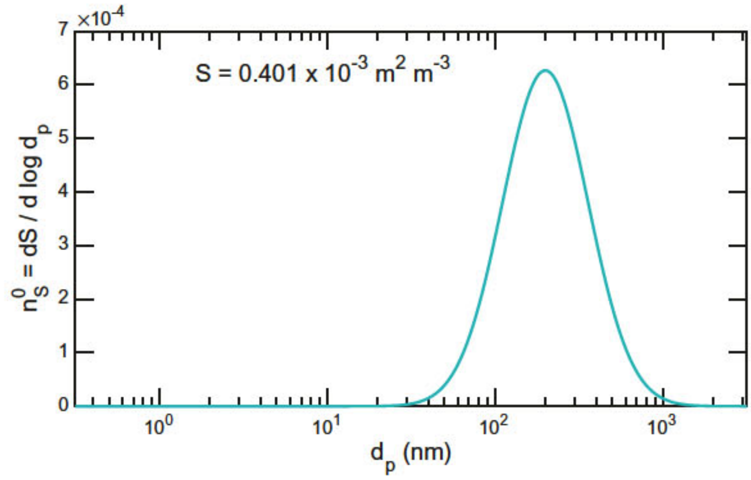

Fig. 4.25 Surface-area distribution for a lognormal number size distribution of particles centered at 100 nm. For this broad distribution, the surface-area mode is shifted to roughly 200 nm.

molecules and almost any real distribution will be broader than the bin width; however, it is very useful to extrapolate microphysics to the gas-kinetic limit, and it is equally useful to resolve any properties of the distribution. For chamber box modeling including 401 variables (or a multiple of this) is not excessive.

We represent the particle distribution with several arrays. First, we have the volume equivalent diameters, $\boldsymbol{d}$; we also used the subscript p as the index of this array, which can be extended generally to indicating a specific particle population, so an element of $\boldsymbol{d}$ is d_p. Corresponding arrays of the diameter squared and cubed along with the particle volume are $\boldsymbol{d}2 = \boldsymbol{d}.\hat{}2$, $\boldsymbol{d}3 = \boldsymbol{d}.\hat{}3$, and $\boldsymbol{v} = (\pi/6)\boldsymbol{d}3$, where $.\hat{}$ is the "pointwise power" array operator.

Often the sections will be spaced by some even interval $\delta \log_{10} d$ but in general, the spacing need not be even, and if we represent the distribution with a moving sectional algorithm including many monodisperse populations, the spacing will certainly not be even. If the spacing is not even, the intervals will also be an array, with $\delta \log_{10} \boldsymbol{d} = (\Delta^+(\log_{10} d) + \Delta^-(\log_{10} d))/2$. In this notation, the finite difference $\Delta^+ x = x_{n+1} - x_n$ while $\Delta^- x = x_n - x_{n-1}$ so

$(\Delta^{+}(\log_{10} d) + \Delta^{-}(\log_{10} d))/2 = (x_{n+1} - x_{n-1})/2$ is the symmetrical average distance between neighboring bins. By extrapolation, we also assume $\delta \log_{10} d_1 = \delta \log_{10} d_2$ and $\delta \log_{10} d_e = \delta \log_{10} d_{e-1}$, where x_e is the end element of the array.

We represent the actual number of particles in the distribution with the integral number in each section, N_p. This is to most effectively accommodate moving sectional representations where the interval spacing varies in time. The number distribution is thus $n_N^{\circ} = \boldsymbol{N}./\delta \log_{10} \boldsymbol{d}$, where we are using the ./ operator to indicate point-by-point element division. We also represent the composition of each particle by the volume fraction of each constituent, $f_{i,p}$, so $v_{i,p} = f_{i,p}(\pi/6)d_p^3$ and $m_{i,p} = \rho_i v_{i,p}$.

4.4.3. *Integral Quantities and Instrument Functions*

We often want to obtain integral quantities from these distributions (the distributions are formed the way they are so that semilog curves showing them have visual areas that we can interpret) but in general, these integrals are bounded by some minimum and maximum size, either for practical reasons (i.e., $\mathrm{PM}_{2.5}$ refers to mass below $2.5\,\mu$m diameter) or instrumental reasons (i.e., instrument transmission intervals).

We will use the substitution $x = d_p$ when we use a subscript to designate size — i.e., J_x is the particle formation rate at size x nm, as in J_3. In this context, the total number N_x above some cutoff size $d_{p,\min}$ is:

$$N_x = \int_{d_{p,\min}}^{+\infty} n_N^{\circ}\, d\log_{10} d_p. \tag{4.70}$$

In practice, the total number measured above the cutoff size is

$$\mathcal{N}_x = \int_{0}^{+\infty} c(d_p; d_{p,\min})\, n_N^{\circ}\, d\log_{10} d_p, \tag{4.71}$$

including a cut function that is in theory given by $c(d_p) = 0, d_p < d_{p,\min}; c(d_p) = 1, d_p \geq d_{p,\min}$ but for all practical instruments exhibits a transition (often presumably sigmoidal) from 0 to 1 over some range. The "cut size" is the 50% transmission diameter. In addition, given transfer lines and the presence of cyclones, etc., real instruments either intentionally or accidentally have some high-size threshold function as well at $d_{p,\max}$ (e.g., 1 nm, 2.5 nm, etc.). The shape of the cutoff/transfer function can be critical to interpreting instrument responses for very small particles during new-particle formation experiments.

We are also interested in numerous other integral parameters of the distribution related to production and loss, often of number, which in general, we can represent as a size-dependent parameter $z(d_p)$:

$$Z_x = \int_{d_{p,\min}}^{+\infty} n_N^{\circ}\, z(d_p)\, d\log_{10} d_p = \bar{z}_x. \tag{4.72}$$

The integral property Z_x is the average over the number size distribution of the parameter $z(d_p)$.

4.4.4. *Dynamical Evolution of the Distribution*

We are interested in the time evolution of the size distribution, with:

$$\begin{aligned}\frac{\partial}{\partial \mathrm{t}} n_N^{\circ} &= \frac{\partial}{\partial \mathrm{t}} \frac{N_p}{\delta \log_{10} d_p} \\ &= P_p - L_p \end{aligned} \tag{4.73}$$

where P_p is production *into* a size interval and L_p is loss *out of* that interval. Production includes direct sources such as new-particle formation, J_p and direct emission, E_p, as well as net condensation into the size range, F_p^{+} and coagulation growth into the size range via collision of two smaller particles, C_p^{+}. Losses include ventilation, V_p (generally independent of size), net condensation out of the size range, F_p^{-}, coagulational growth of particles in the size range when smaller particles augment their mass C_p^{-}, coagulation of particles in the size range onto larger particles C_p, and deposition, D_p (wall losses, W_p, in chamber experiments). In theory, one could consider disaggregation in opposition to coagulation but this is probably important only for the smallest clusters below a hypothetical critical diameter very near the low end of the size distribution.

The terms with superscripts, $X^{+,-}$, are transport (net growth) terms specific to the Eulerian framework of the distribution due to condensation and coagulation. They are paired and should integrate to equal and opposite quantities; neither is a net source nor a sink of particle number, though each is a net source (or sink for evaporation) of mass. Coagulation includes three terms because collisions of smaller particles with larger particles are a net sink of particle number, and overall the mass flux associated with the three coagulation terms must also integrate to zero, as coagulation conserves mass.

The emission and ventilation terms are straightforward, and nucleation is usually represented as a rate of formation into the smallest size bin of the sectional distribution, though in our case new particles may appear in some bin or bins near the low end of the distribution. However, condensation, coagulation, and deposition (wall losses) are central to the objectives and limitations of chamber and flowtube experiments and so we shall examine them in detail.

Once we describe the microphysics, we can now implement and examine the time evolution of the size distribution under both nucleation and accumulation-mode condensation conditions.

$$\frac{\partial}{\partial t} n_N^{\mathrm{o}} = J_p + F_p + E_p + C_p + V_p + W_p. \tag{4.74}$$

If we integrate Eq. (4.74), we obtain the governing equation for the integral quantities with a cut size at $d_p = x$:

$$\begin{aligned}
\frac{\partial}{\partial \mathrm{t}} N_x &= \bar{F}_x + \bar{E}_x + \bar{C}_x + \bar{V}_x + \bar{W}_x \\
&= F_x^{+} + C_x'^{+} + C_x'^{-} + \bar{E}_x + \bar{V}_x + \bar{W}_x \\
&= J_x' + C_x'^{-} + \bar{E}_x + \bar{V}_x + \bar{W}_x \qquad (4.75)
\end{aligned}$$

$$\begin{aligned}
J_x' &= \frac{\partial}{\partial \mathrm{t}} N_x - (C_x'^{-} + \bar{V}_x + \bar{W}_x) \qquad (4.76) \\
&= \frac{\partial}{\partial \mathrm{t}} N_x - (\text{Losses}).
\end{aligned}$$

Here, the apparent particle formation rate (at the cut size) J'_x is given by the rate of change of the total number above that cut size minus any losses (assuming no emissions). This growth across the cut size can occur via condensation or due to a subset of coagulation. The condensation is straightforward, but the coagulation is more subtle. Effective production from coagulation, C'^{+}_{x}, occurs only when two particles smaller than the cut size combine to form one particle larger than the cut size. Likewise, effective loss from coagulation, C'^{-}_{x}, occurs only when two particles larger than the cut size combine to form one particle larger than the cut size. Coagulation between one particle smaller than the cut size and one larger than the cut size has no effect on the apparent formation rate at the cut size, nor does coagulation between two smaller particles that produces a particle that is still smaller than the cut size.

4.4.4.1. *Condensation Mass Flux*

The condensation flux per unit particle surface area depends on the particle size, as described in Section 4.3 and given by Eq. (4.37). In the top panel of Fig. 4.26, we show the ratio of the deposition velocity and the surface normal molecular speed for condensing vapors with three different compositions, representing nitric acid, sulfuric acid, and highly oxidized organics. The nitric acid (blue) has a molar weight of $64\,\mathrm{g\,mole^{-1}}$ and a volume equivalent diameter of 0.25 nm, the sulfuric acid (red) has a molar weight of $98\,\mathrm{g\,mole^{-1}}$ and a volume equivalent diameter of 0.3 nm, and the organics (green) have a molar mass of $250\,\mathrm{g\,mole^{-1}}$ and a volume equivalent diameter of 0.9 nm, consistent with condensing organic monomers. The different masses and sizes of the condensing vapors influence the collisional reduced mass and overall impact parameter for very small particles; below 1 nm, the effects are extraordinarily important, but even up to 3 nm the effect is almost a factor of two.

The collision velocity $v^{\mathrm{col}}_{i,p}$ contains the size dependence of collisions between gases and the particle suspension, which constitutes a large fraction of the expected size dependence for condensation. We can write the full collision frequency distribution for vapors with

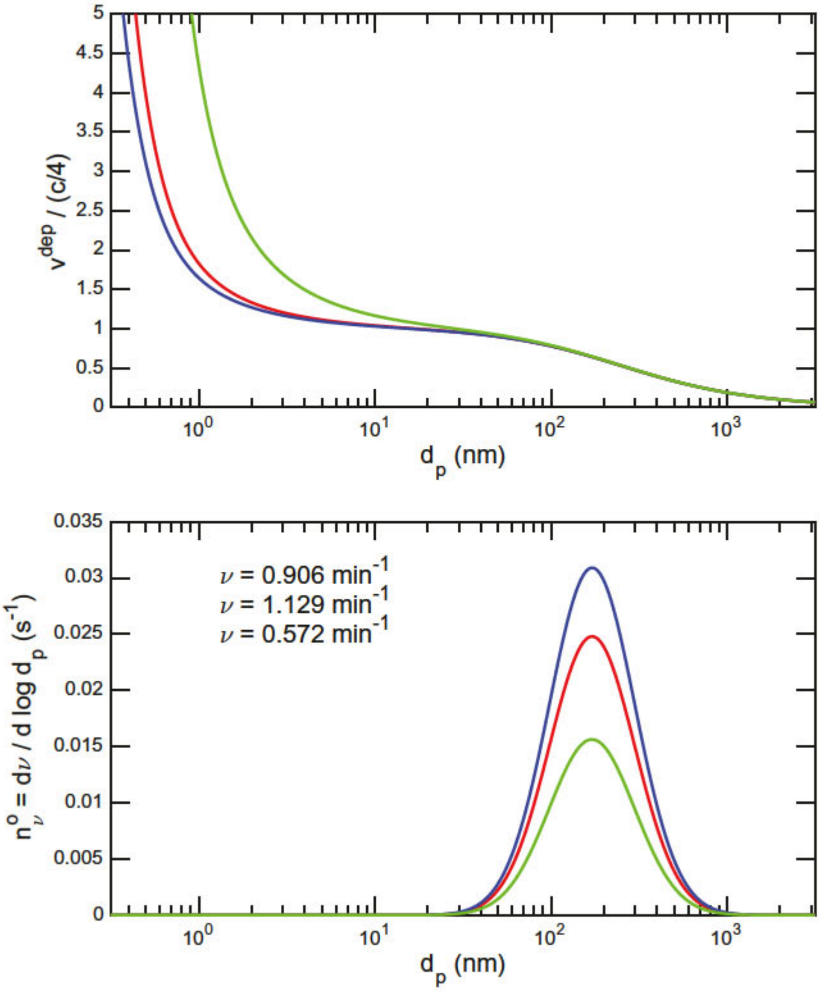

Fig. 4.26 Scaled deposition velocity and collision frequency distribution for a lognormal number size distribution of particles centered at 100 nm. The green curve (“organics”) is for 250 g mole^{-1} vapors with a 0.9 nm collisional diameter and density of 1.4 g cm^{-3}, the red curve (“sulphate”) is for somewhat faster 98 g mole^{-1} vapors with a 0.3 nm collisional diameter and density of 1.84 g cm^{-3}, and the blue curve (“nitric acid”) is for even faster 64 g mole^{-1} vapors, where the collision enhancement at small size is reduced. Note that for this broad distribution the collision frequency mode is shifted to roughly 180 nm.

particle surface area as

$$n^{\mathrm{o}}_{\nu} = v^{\mathrm{col}}_{i,p}\, n^{\mathrm{o}}_{S}. \tag{4.77}$$

This collision frequency is often casually referred to as the condensation sink as well, though the condensation sink must also account for effective mass accommodation coefficient α' and so the two are equal only if $\alpha = 1$. When calculating the collision frequency distribution, we must (as always) pay careful heed to the units. Given that we are starting with a number distribution in # cm^{-3} and d_p in nm, we need to multiply by 10^{-18} to convert nm^2 to m^2 and 10^6 to convert cm^3 to m^3 for an overall scaling factor of 10^{-12}. The resulting collision frequency distribution for the example number distribution under consideration here is shown in the bottom panel of Fig. 4.26, again for nitric acid, sulfuric acid, and a highly oxidized organic monomer. The mode for the collision frequency distribution is slightly smaller than the mode for the surface-area distribution because of the onset of gas-phase diffusion limitations toward larger sizes.

As the collision frequency distribution in Fig. 4.26b shows, the larger and heavier organics collide less frequently than the lighter inorganics with a transition-regime surface-area distribution such as the one under consideration here, yet will collide more frequently with surface area in the smallest particle sizes as noted above. Thus condensible organics can contribute disproportionately to the growth (and survival) of the smallest particles; however, this effect is also highly uncertain because the major contributor is the effective collisional diameter of the condensing vapors.

The collision frequency distribution is of great interest for the gas-phase condensible vapors because they will be produced via oxidation chemistry and lost via either condensation to suspended particles or the chamber walls; the frequency is a major element of their sink. However, for the particles themselves we are interested in the condensation mass flux, as well as the integrated mass flux from the vapor to the condensed phase, $\Phi_i^{v,h}$. Given the collision frequency distribution, total surface-area distribution, and condensation driving force, we can define a net condensation distribution as:

$$n_{\Phi}^{\circ} = n_{\nu}^{\circ}\, \alpha_p'\, F_{i,p}^{v,h}. \tag{4.78}$$

If we regard the initial distribution of particles in our fairly broad 100 nm mode as seed particles for condensation, we can calculate the normalized flux distribution assuming $\alpha' = 1$ and $F_{i,p}^{v,h} = \text{const.}$, and compare that with the normalized seed particle mass distribution, as shown in the top panel of Fig. 4.27. This shows condensation characteristically favoring smaller particles according to their "Fuchs corrected" surface area, which drives condensational narrowing and will cause broad seed distributions to develop a strongly size-dependent condensate to seed mass ratio. In the bottom panel of Fig. 4.27, we show the absolute flux distribution for $F_{i,p}^{v,h} = 1\,\mu\text{g}\,\text{m}^{-3}$ of condensible organic vapors; given the integrated collision frequency $\nu = 0.572\,\text{min}^{-1}$ it is self-evident that the condensation should be $34.3\,\mu\text{g}\,\text{m}^{-3}\text{h}^{-1}$.

4.4.4.2. *Net Condensational Growth*

As illustrated in Fig. 4.22, the growth rate g_p is a source and sink of number distribution n_N. The growth rate is:

$$g_{i,p} = \frac{2\, q_p\, \phi_{i,p}^{h}}{\rho_p^h} = 2\, q_p\, \alpha_{i,p}'\, v_{i,p}^{\text{col}}\, \frac{F_{i,p}^{v,s}}{\rho_p^h}; \quad g_p^{\circ} = \frac{\sum_i g_{i,p}}{\ln(10)\, d_p}. \tag{4.79}$$

The term $F_{i,p}^{v,s}/\rho$ is the net condensation driving force for species i to all suspended phases h within the particle, and so we indicate the total particle suspended phase with superscript s. This is divided by the density of the condensed phase; it is thus the condensed volume concentration equivalent of condensible vapors.

In Fig. 4.28, we show the growth rate given a constant driving force $F_p^{v,s} = 1\,\mu\text{g}\,\text{m}^{-3}$. The salient feature is that for 10–100 nm particles, this drives roughly $200\,\text{nm}\,\text{h}^{-1}$ growth. Producing $35\,\mu\text{g}\,\text{m}^{-3}$ of secondary material in a chamber experiment over an hour would be a relatively modest condensation rate, and yet the growth rate is roughly 100 times the typical $1\,\text{nm}\,\text{h}^{-1}$ of the ambient atmosphere.

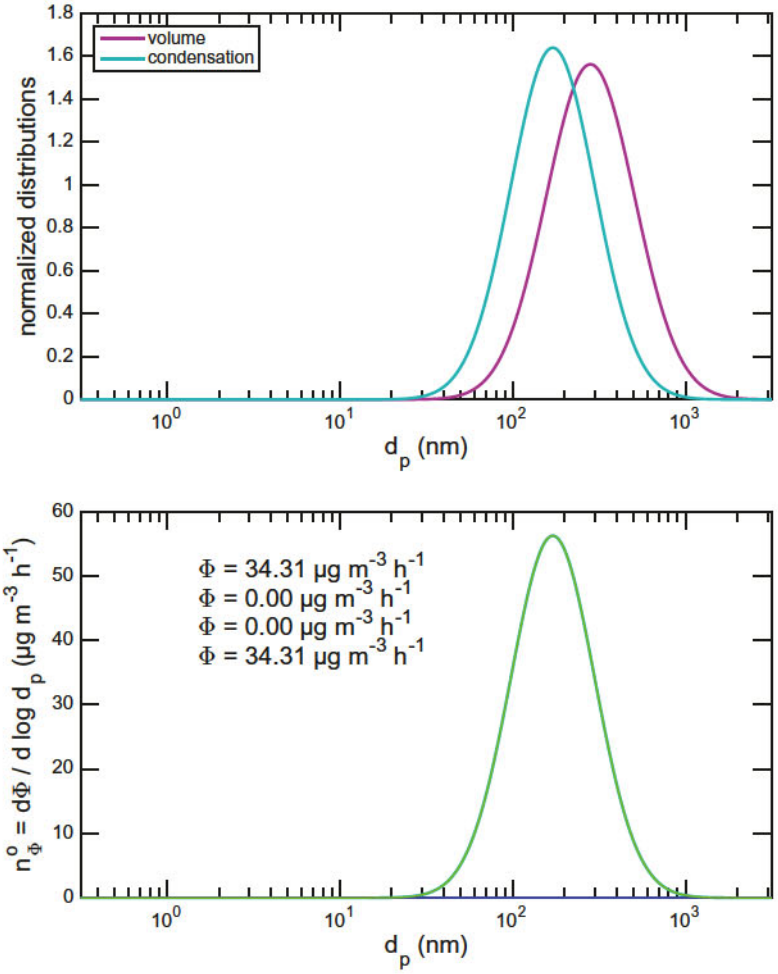

Fig. 4.27 Condensation to seeds. The top panel shows the (area) normalized condensation distribution follows the collision frequency distribution for nonvolatile condensation, with a mode at 180 nm, whereas the seed mass mode is at roughly 300 nm. The bottom panel shows the corresponding mass flux distribution for a condensation driving force of 1 μg m^{-3} of the organics.

The growth rate g_p^o multiplied by some time element δt gives a distance swept out in the the number distribution $n^o_{N,p}$, as illustrated in Fig. 4.22 and discussed above. This is a production term (or loss term for evaporation) of total number above the size threshold d_p

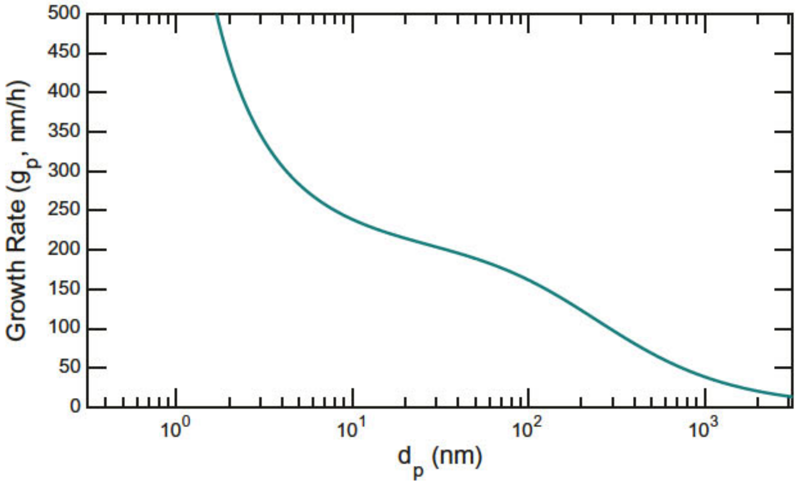

Fig. 4.28 Growth rate from condensation of 250 g mole^{-1} vapors, in nm h^{-1}, given a 1 μg m^{-3} condensation driving force.

(neglecting coagulation):

$$J'_p = g_p^{\circ}\, n_{N,p}^{\circ}. \tag{4.80}$$

Extending to extremely small diameter (notionally the "critical" diameter d_p^{crit}) this is the nucleation rate itself.

We show the formation rate for the example size distribution and $F^{v,h} = 1\,\mu\text{g}\,\text{m}^{-3}$ in Fig. 4.29. There are three items of note. First, this is *not* a distribution though it resembles the number distribution; the function gives the net formation rate at any given size. Second, it is shifted dramatically to smaller size than the number distribution because of the $1/d_p$ dependence of g_p° and to a lesser degree the size dependence of g_p within (this has a dramatic effect below 10 nm). Third, because of the $1/d_p$ dependence, the formation rate at this size is modest; an identical looking distribution with the same amplitude and total number centered at 1 nm would give a formation rate 100 times larger due to the $1/d_p$ dependence and roughly a factor of five larger due to the increased effective collision speed, resulting in a formation rate of roughly 1000 cm^{-3} s^{-1}.

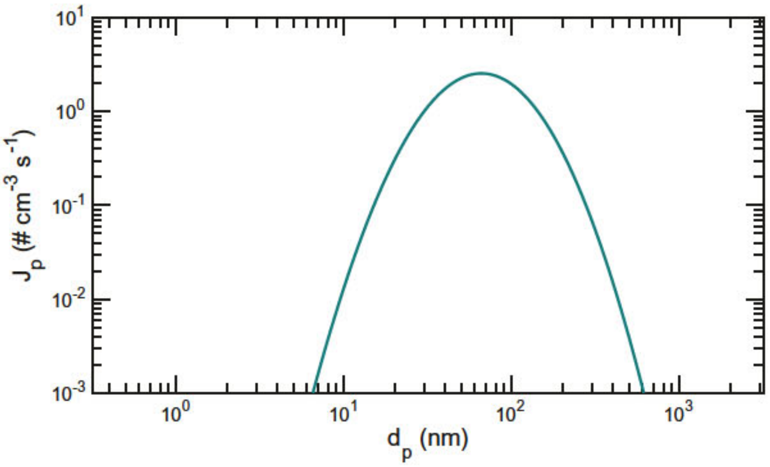

Fig. 4.29 Particle formation rate from condensation, J_p', at any given size, d_p, for a lognormal number size distribution of $1.4\,\mathrm{g\,cm^{-3}}$ particles centered at 100 nm with a condensation driving force of $1\,\mu\mathrm{g\,m^{-3}}$.

4.4.4.3. *Condensation and the Size Distribution*

From the perspective of a given size bin, net condensation to particles in that bin will be a loss out of that bin, while condensation from the neighboring smaller bin (for growth) or larger bin (for evaporation) will be a source. The net change is a derivative and it can be expressed as a net condensational change in the balance equations:

$$F_p = F^+_{(p-1)} - F^-_p = -dJ_p/d\log_{10}d_p. \tag{4.81}$$

This is one reason why a broad distribution makes it difficult to measure growth rates in experiments, as the small derivatives obscure the growth rate.

When we take a finite difference of discrete sizes, the raw number fluxes F_p will not conserve mass, and we must apply a mass conservation factor, F_C. This is a variant of the redistribution described in Eq. (4.66); when particles grow part of the way toward the next discretized size, we hold a portion back to conserve mass. It is far more stable numerically to do this after allowing particles to grow in a moving sectional size step, but when we are numerically integrating distributions to determine overall process rates, we still need to account for what amounts to unrepresented curvature in the distribution functions.

For a logarithmic distribution, we can represent the larger sizes as a fraction of the original (smaller) size:

$$d_{pn} = d_{p-} \cdot \Delta; \quad d_{p+} = d_{p-} \cdot \delta, \tag{4.82}$$

where

$$\Delta = 10^{\Delta \log_{10} d_p}; \delta = 10^{\delta \log_{10} d_p}. \tag{4.83}$$

and $f_{p+} = d_{pn}/d_{p+}$. The mass conserving fraction is thus

$$\chi_{p+} = \frac{\Delta^3 - 1}{\delta^3 - 1}. \tag{4.84}$$

The mass conserving expressions for redistribution are exact, but considering numerical integration it is useful to expand them. Specifically, we generally will set up distributions with $\delta \log_{10} d_p \ll 1$ and short time-steps will presumably involve $\Delta \log_{10} d_p \ll \delta \log_{10} d_p$. With the substitution $x = 3\,\delta \log_{10} d_p$, we have a Taylor series

$$\delta^3 = 10^x = 1 + \ln(10)\,x + \frac{1}{2}\ln^2(10)\,x^2 + \frac{1}{6}\ln^3(10)\,x^3 + \cdots \tag{4.85}$$

and with $X = \Delta\log_{10} d_p$, we have

$$\chi_{p+} = \frac{\ln(10)\,X + \frac{1}{2}\ln^2(10)\,X^2 + \frac{1}{6}\ln^3(10)\,X^3 + \cdots}{\ln(10)\,x + \frac{1}{2}\ln^2(10)\,x^2 + \frac{1}{6}\ln^3(10)\,x^3 + \cdots}, \tag{4.86}$$

or

$$\chi_{p+} = f_{p+}\,\frac{1 + \frac{1}{2}\ln(10)\,X + \frac{1}{6}\ln^2(10)\,X^2 + \cdots}{1 + \frac{1}{2}\ln(10)\,x + \frac{1}{6}\ln^2(10)\,x^2 + \cdots}. \tag{4.87}$$

At the limit of very small time-steps, $(X \ll x \ll 1)$, the numerator will approach 1.0, but the denominator will remain slightly larger than 1.0 for any realistic section spacing.

Numerical integration of the growth rates within a logarithmic sectional representation will find a number flux $J = g_p^\circ n_N^\circ$ that slightly overestimates the mass flux by a factor:

$$f_C = 1 + \frac{3}{2}\ln(10)\,\delta\log_{10}d_p + \frac{3}{2}\ln^2(10)\,(\delta\log_{10}d_p)^2 + \cdots. \tag{4.88}$$

When particles are growing, the raw number flux will *over*estimate the mass flux, while when they are shrinking the raw number flux will *under*estimate the mass flux, so we need to separate the two, which can occur simultaneously in different parts of the distribution. For $\delta\log_{10}d_p = 0.01$, $F_C \simeq 1.0353$. As a finite difference, net condensation to particles growing out of the bin is a sink

$$F_{p+}^{-} = J_p/(F_C\,\delta\log_{10}d_p), \tag{4.89}$$

and net evaporation from particles shrinking out of the bin is also a sink

$$F_{p-}^{-} = -F_C\,J_p/\delta\log_{10}d_p, \tag{4.90}$$

At the same time, net condensation from the next smallest bin is a source

$$F_{p+}^{+} = J_{p-1}/(F_C\,\delta\log_{10}d_p), \tag{4.91}$$

and net evaporation from the next largest bin is also a source

$$F_{p+}^{+} = -F_C\,J_{p+1}/\delta\log_{10}d_p. \tag{4.92}$$

Numerically, we are converting the uniform process of condensation, which should cause growth of all particles in the (internally mixed) bin at a uniform rate, into a process in which a fraction of the particles in the bin given by $g_p^\circ\delta\mathrm{t}/\delta\log_{10}d_p$ are selected to carry all of the growth into the next bin, as illustrated in Fig. 4.22. This intrinsically generates numerical diffusion.

The upper panel of Fig. 4.30 shows the numerical derivative of the formation rate (including the mass correction factor F_C), which gives the net contribution of condensation to the number size distribution n_N°. The integrated contribution is zero, as condensation conserves

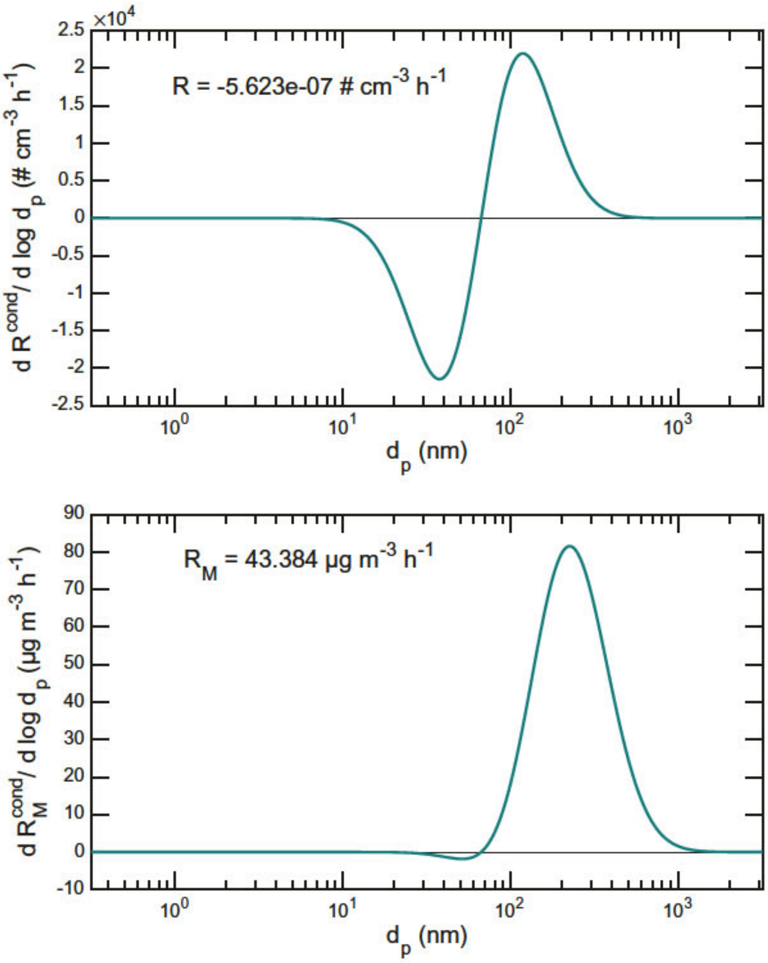

Fig. 4.30 Rate of change of the number distribution (top) and mass distribution (bottom) caused by condensation for a lognormal number size distribution of $1.4\,\mathrm{g\,cm^{-3}}$ particles centered at 100 nm with a condensation driving force of $1\,\mu\mathrm{g\,m^{-3}}$.

mass, but below the maximum of J_p (when particles are growing) condensation is an effective net sink and above the maximum it is an effective net source. However, this is obviously a source of mass, as shown in the lower panel of Fig. 4.30. While the total mass flux agrees with the condensation flux distribution shown in Fig. 4.27, the size dependence of the effective mass flux has significant differences — most notably that the effective number sink toward the small end of the distribution necessarily appears as a small but nontrivial mass sink. This is the difference between the condensation flux from the gas phase to the particle phase, which for all sizes (given a net positive condensation driving force) must be positive definite, and the effect of this condensation on the mass distribution, which must *integrate* to the same number but differs in detail because the condensation drives growth.

4.4.4.4. *Coagulation*

Coagulation (collisional coalescence of two particles to form one larger particle) can be broken down into two subelements: loss of small particles when they collide with larger particles, and growth of large particles when they incorporate smaller particles. The growth element in turn can be thought of in two parts: a formal growth rate of the large particle, derived from the rate of volume addition by incorporation of all smaller particles, and the resulting size distribution of the enlarged particles, distributed between sizes only slightly larger than the original size when the incorporated particle is very small to $\sqrt[3]{2} = 1.26$ larger when the two particles are the same size.

Coagulation occurs between particles and mostly involves at least one particle in the high Knudsen number limit where the particle radius is smaller than the mean free path of air molecules, and thus diffusion of momentum (viscosity) plays a limited role compared to direct collisional energy transfer between air molecules and particles. In other words, there is a significant slip correction factor because a no-slip momentum transfer boundary condition will generally not be appropriate for the smaller particle. Coagulation is described in terms of a coagulation coefficient $K_{i,j}$ between particles with (size) index i and j. This is a second-order rate coefficient and because number concentrations are generally given in $\# \text{ cm}^{-3}$ it has units of $\text{cm}^3 \ \#^{-1} \, \text{s}^{-1}$. The coagulation rate constant is unique for collisions between two particle sizes i and j and is thus a matrix $\boldsymbol{K}$ with

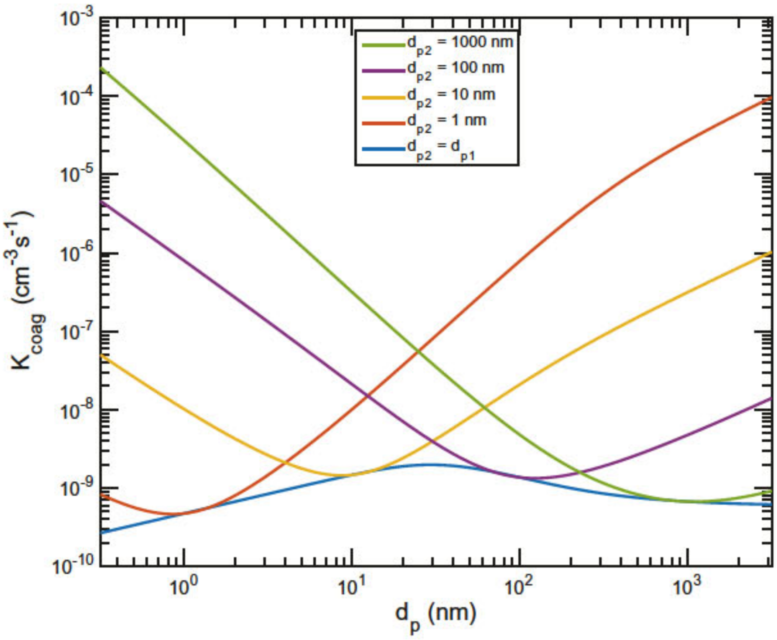

Fig. 4.31 Coagulation rate coefficient for two particles of density 1.4 g cm^{-3}.

elements $K_{i,j}$ given by, e.g., Table 13.1 in the second edition of Seinfeld and Pandis.[63] In Fig. 4.31, we show values for neutral particle collisions based on Fuchs via Seinfeld and Pandis as a function of particle size d_{p1} for a selection of second particle sizes d_{p2}. The blue curve shows the collisional rate constant for two particles of the same size. Note that a typical hard-sphere collisional rate constant for small molecules with effective spherical diameters of 0.3 nm or so is $3 \times 10^{-10}\,\mathrm{cm^3\,mole^{-1}s^{-1}}$, which is reproduced in Fig. 4.31.

For this example calculation, we are considering condensible organic vapors with a condensed-phase density $\rho_i = 1.4\,\mathrm{g\,cm^{-3}}$, a molar mass of $250\,\mathrm{g\,mole^{-1}}$, and an effective diameter $d_i = 0.9\,\mathrm{nm}$. This diameter is based on the mass and density and reflects some compromise between the physical (hard sphere) size of the gas-phase condensible molecules and longer-range attractive forces that increase the interaction distance. It is a common assumption but it does introduce uncertainty for the smallest particles. For coagulation, the properties of vapors are only relevant in the smallest portion of the size distribution where the distinction between gases and particles blurs. However, the coagulation rate constants do depend on particle density and so if any dynamical processes change the particle density, the rate constants will change.

The collisional rate between two particles is given by

$$R_{\mathrm{col}} = \boldsymbol{n}_N^{\circ} \cdot^{*} (\boldsymbol{n}_N^{\circ} \times \boldsymbol{K}). \tag{4.93}$$

4.4.4.5. *Coagulation Number Loss*

When a smaller particle collides with a larger particle (and half the time when two particles of the same size collide), we call this "coagulational loss". This fully describes the loss of number associated with coagulation. The coagulation loss first-order rate constant for a particle of size d_p at any given time is thus

$$k^{I}_{\mathrm{coag}}(d_p) = \int_{d_p}^{\infty} n_N^{\circ}\, K(d_p, d_p')\, d\log d_p'. \tag{4.94}$$

This gives the collisional frequency for particles of size d_p with any particles larger than d_p (with a caveat for particles that are exactly the same size, where either the rate constant is halved or the number of particles "smaller than the other" is half of the total). The coagulation number loss coefficient and loss rate constant are given by the lower left portion of the coagulation coefficient matrix, along with the diagonal divided by two.

In Fig. 4.32, we show the first-order loss frequency for the example number size distribution centered at 100 nm as a function of particle diameter. This shows the full features of coagulation; smaller particles have a shorter lifetime because they move faster, so below the range of the surface-area size distribution (roughly between 80 and 800 nm), the loss frequency drops steadily as size increases. As size moves through the range of the distribution, the available surface area for loss also drops and so the overall loss frequency drops precipitously.

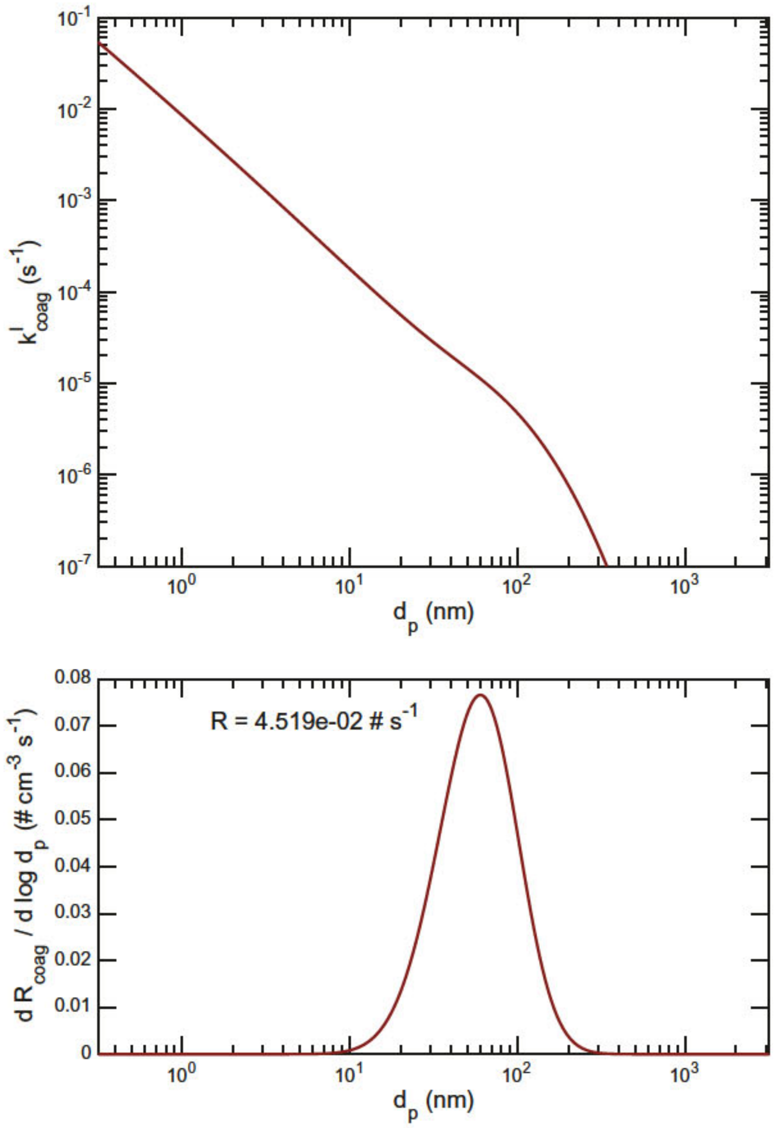

Fig. 4.32 First-order coagulation rate constant (top) for a lognormal number size distribution of 1.4 g cm^{-3} spherical particles centered at 100 nm, leading to a total first-order loss frequency distribution (bottom).

To check the overall values, it is again worthwhile considering the condensing vapors in this example, which are 250 g mole^{-1} molecules with an effective size of 0.9 nm and as shown in Fig. 4.26 have a condensation loss frequency of $9 \times 10^{-3}\,\mathrm{s}^{-1}$. The values in Fig. 4.32 are very similar at the same size. Particles (clusters) of roughly 1 nm diameter have a lifetime of 100 s ($1/k^I$) or roughly 2 min but by 70 nm this lifetime is 10^5s (more than 1 day).

Overall, the coagulation rate for this distribution is small, with a total loss of 166 cm^{-3} h^{-1}/6399 cm^{-3} = 2.6% h^{-1}. The features visible in Fig. 4.26 are characteristic. The coagulation loss is strongly weighted toward the small end of the number size distribution, and for a distribution such as this with relatively large particles, the overall coagulation loss rate is very small.

4.4.4.6. *Coagulation Mass Redistribution*

The second aspect of coagulation is that it represents a mass flux to the larger particles, and the mass flux drives particle growth. As with all formal growth rates, we can relate the mass flux per unit (larger) particle surface area due to accretion of (smaller) particles and directly calculate a growth rate. We show this in Fig. 4.33 for

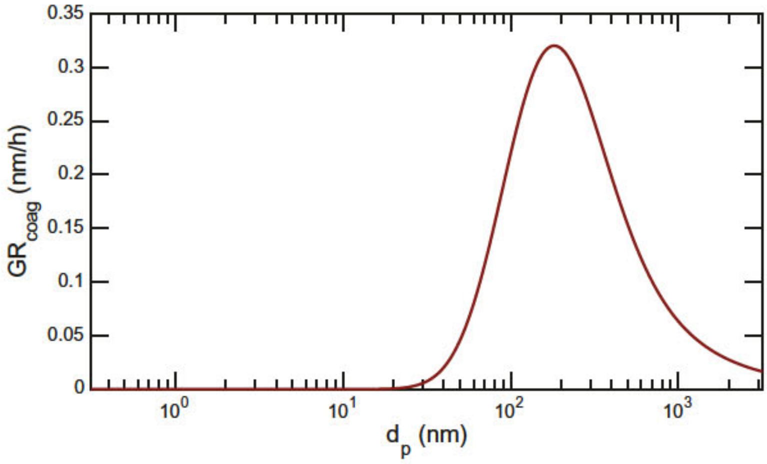

Fig. 4.33 Growth rate from coagulation for a lognormal size distribution centered at 100 nm spherical equivalent diameter.

the example size distribution we have been considering. Compared with the roughly 200 nm h^{-3} condensational growth, the growth rate from coagulation is very small, barely 0.1% at most.

With coagulation, however, the growth rate is not sufficient to locate the larger particles, because coagulation is not a continuum process driving gradual growth but rather causes a stepwise change in size. The new particle will have a mass $m_p = m_s + m_l$ and thus be located at some greater size than the larger particle involved in the collision. As with condensational growth, for a sectional algorithm we must distribute the resulting particle in two bins above and below the exact new-particle size in order to conserve mass.

In Fig. 4.34, we show the three separate coagulation rates: real loss of small(er) particles, $dC_p/d\log_{10} d_p$; apparent loss of larger particles, $dC_p^-/d\log_{10} d_p$; and production of large(st) particles from the coalescence $dC_p^+/d\log_{10} d_p$. Each rate distribution must (and does) integrate to the same absolute value.

In Fig. 4.35, we show the net effect of coagulation on the number (top) and mass (bottom) distributions. Where condensation conserved total number and caused a mass change in the distribution equal to the net condensation flux, here coagulation conserves mass

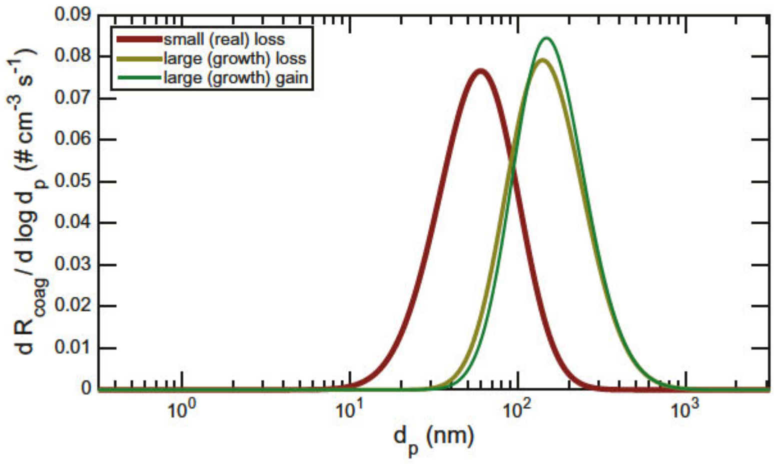

Fig. 4.34 Coagulation rates for a lognormal size distribution centered at 100 nm spherical equivalent diameter.

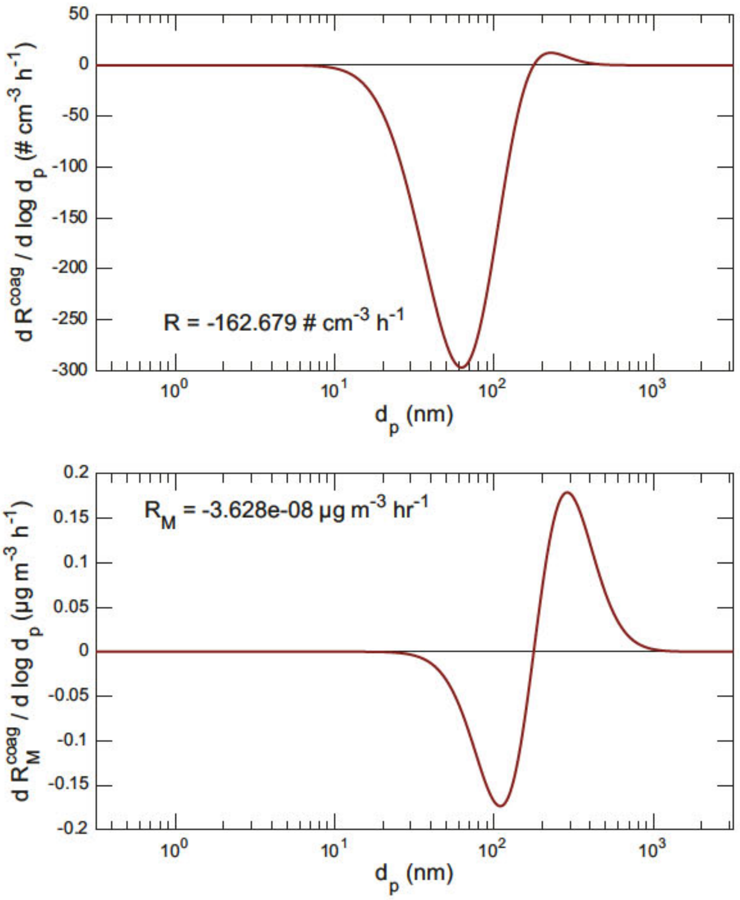

Fig. 4.35 Rate of change due to coagulation of the number distribution (top) and mass distribution (bottom) for a lognormal number size distribution of 1.4 g cm^{-3} particles centered at 100 nm.

(the bottom distribution integrates to zero) and causes a net number loss equal to the total loss rate of smaller particles colliding with larger particles.

4.4.4.7. *Wall Loss*

The last major nontrivial loss is wall loss. Wall loss of suspended vapors and particles in turbulent chambers results in a first-order loss process in which the collision frequency of material with the chamber wall is controlled by both the turbulent energy, characterized by a nominal eddy mixing parameter, k_e, the surface area to volume ratio of the chamber (S:V), and the diffusion coefficients $D(d_p)$ (neglecting gravitational settling of larger particles and any charge effects):

$$\nu_{\text{wall}} = \frac{2}{\pi}\,\mathrm{S:V}\,\sqrt{k_e\,D(d_p)}. \tag{4.95}$$

In Fig. 4.36, we show the first-order wall loss rate constant for a 10 m^3 chamber with an eddy parameter of $k_e = 1\,\mathrm{s}^{-1}$, which is consistent with observed particle wall losses but overestimates observed vapor wall losses for sulfuric acid (red) and organics (green) as shown. The loss rate is roughly 10 times the coagulation number loss rate, as shown in Fig. 4.32, so under these circumstances, wall losses dominate over coagulation by roughly one order of magnitude.

The wall loss rates for number and mass are recapitulated in Fig. 4.37, for both the number and mass distributions. Unlike the other microphysics, wall losses are positive definite across the size range for both number and mass; they transfer number and mass only to the walls, and do not redistribute either.

4.4.5. *Overall Influences on the Size Distribution*

The overall effect of these processes on the size distribution is our ultimate objective. In Fig. 4.38, we show the size-dependent first-order coagulation and wall loss frequencies, along with a size-independent ventilation loss with a time constant of 1 day. A general design objective for chamber experiments is to have condensible vapors collide with particles many times before they interact with the walls (so the "coagulation" loss should exceed the wall loss for small d_p, where "coagulation" is actually condensation), and yet the suspended particles ideally will have relatively small coagulation and small wall losses that nonetheless exceed coagulation, so that the mass balance corrections for wall losses are straightforward and accurate.

The coagulation rate is a function of the suspended surface-area size distribution, while the wall loss is a function of chamber

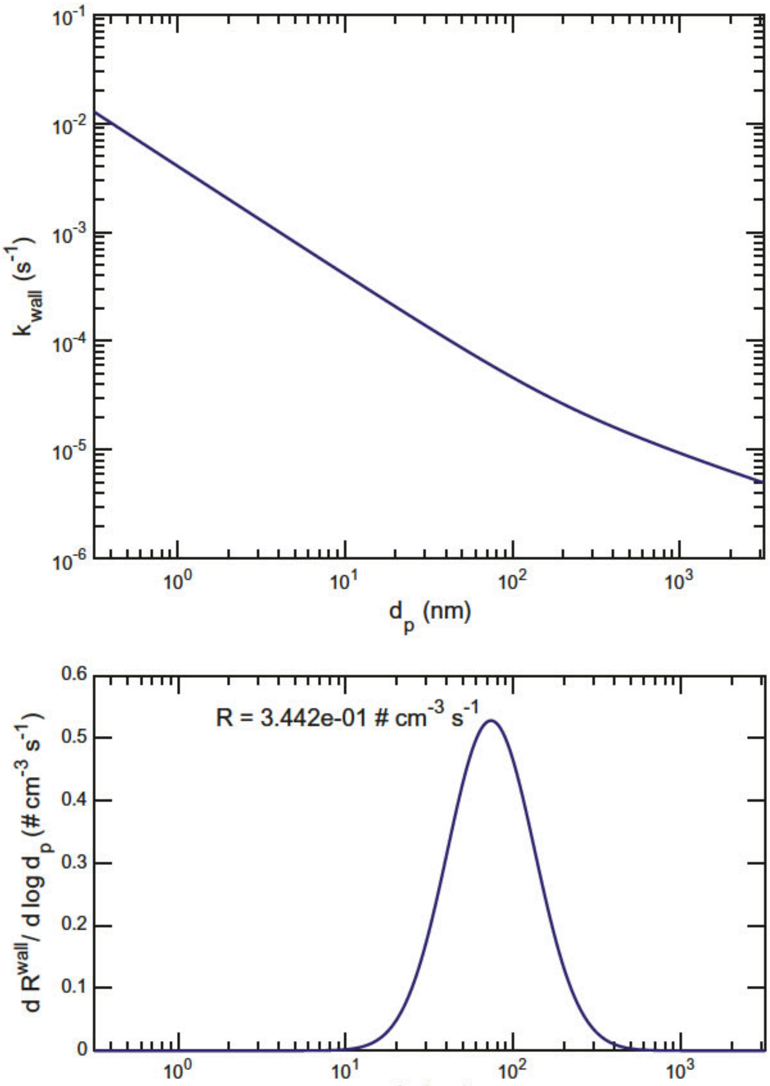

Fig. 4.36 First-order wall-collision frequency (top) for a lognormal number size distribution of 1.4 g cm^{-3} spherical particles centered at 100 nm, leading to a wall loss rate distribution (bottom).

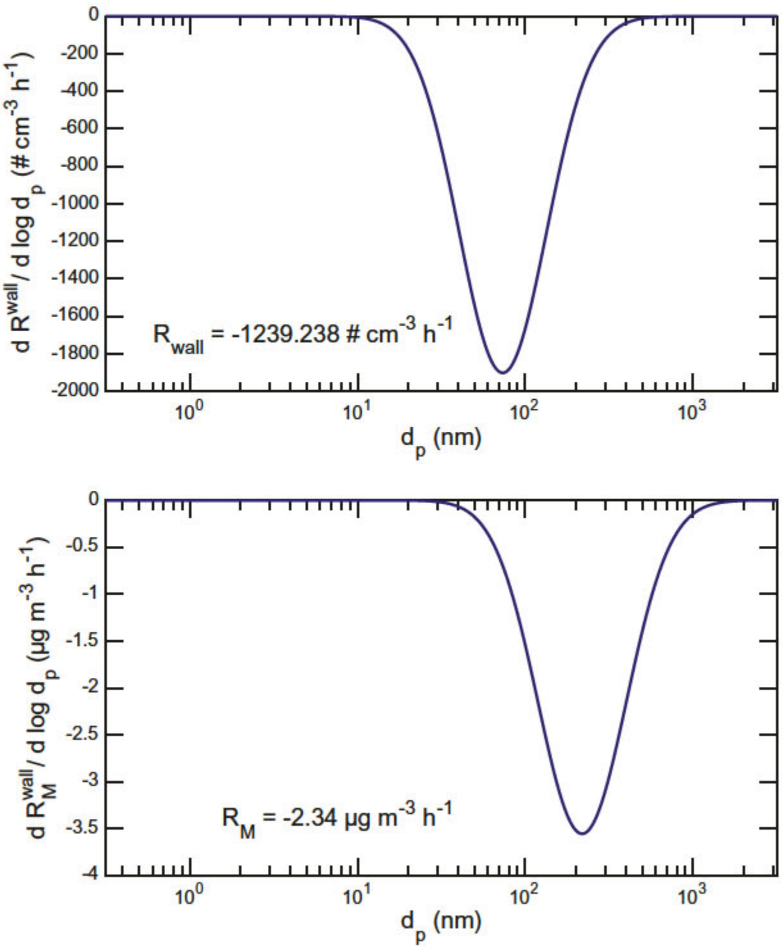

Fig. 4.37 Rate of change due to wall loss of the number distribution (top) and mass distribution (bottom) for a lognormal number size distribution of 1.4 g cm^{-3} particles centered at 100 nm.

turbulence (and perhaps charging, which we have not treated here). However, the objective is to have the two quantities cross somewhere near $d_p = 10\,\mathrm{nm}$ with a suspended seed distribution well larger and condensing vapors (obviously) much smaller. At least in theory, that objective is met for the situation shown in Fig. 4.38, though as particles are lost to the wall, the coagulation values will drop.

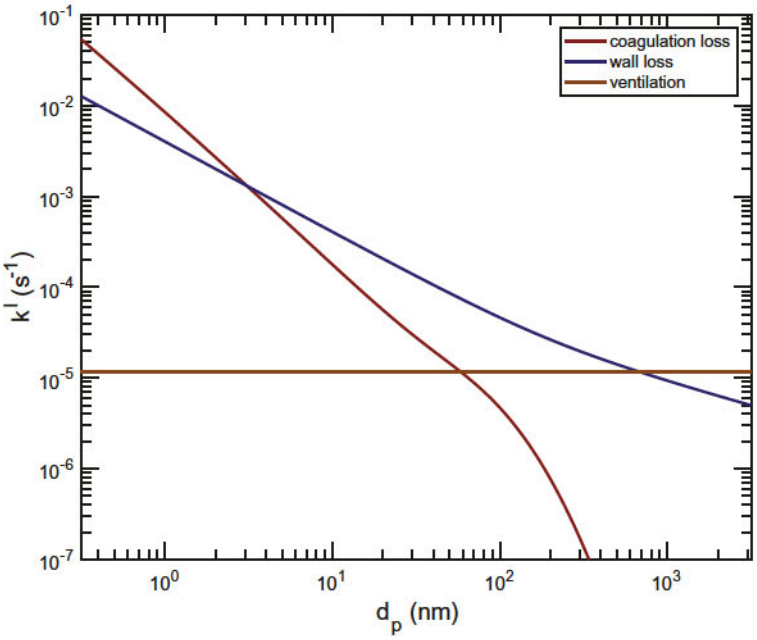

Fig. 4.38 Overall first-order loss frequencies for a lognormal number size distribution of 1.77 g cm^{-3} spherical particles centered at 100 nm.

We show the total effect of these three processes on the number and mass distributions in Fig. 4.39. This shows that when there is a large condensation driving force ($F^{v,c} = 1\,\mu\mathrm{g\,m}^{-3}$ in this case) that condensation largely overwhelms the other processes. This even applies to the particle number rates, meaning that the particle growth has a much larger influence on the distribution than the losses; however, the integral of condensation is still zero, so the integral quantity — the change in total number $\mathrm{d}N/\mathrm{dt}$, is still controlled by wall loss and coagulation. That is why we use relatively high seed surface area (to ensure that the condensible vapors encounter particles before the wall) and relatively high condensation driving forces (to ensure that the particle distribution is influenced principally by condensation). The microphysical evolution is in this case readily attributable to condensation; large nearly stepwise changes in the size and total suspended mass of the distribution are easy to detect.

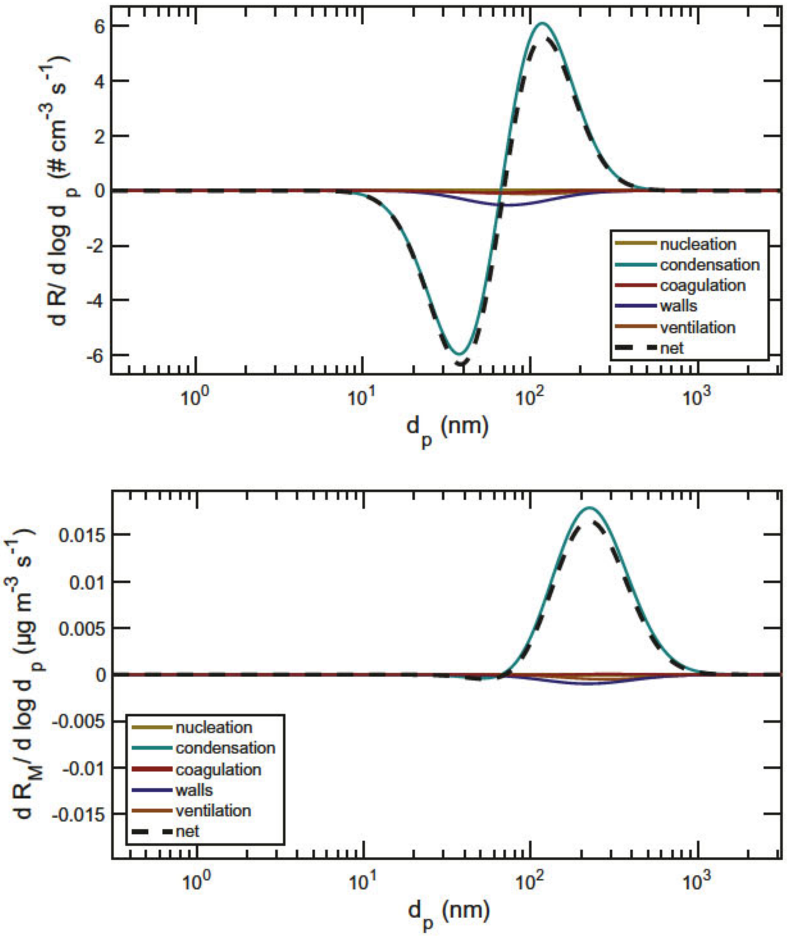

Fig. 4.39 Rate of change due to all causes of the number distribution (top) and mass distribution (bottom) for a lognormal number size distribution of particles centered at 100 nm.

However, the conditions do not correspond to those found in the atmosphere.

The near perfect separation of changes in the distribution n_N° and the integral N of particle number are one reason we separate the experimental methods focused on integrated volume from those focused on growth rates in Eq. (4.54). The constraints on these two measures (of the same overall process) are largely independent. The tools presented thus far can and should be used in a diagnostic mode during any experiment with measurements of the size distribution (number or mass), as they reveal the sensitivities of any given distribution to various processes. However, they also form the basis for numerical simulations of the evolution of the particle population.

4.4.6. *Dynamical Simulations*

For the fine sectional algorithm employed here, we can solve the coupled equations using finite difference with a master time step Δt:

$$\frac{\delta n_N^\circ}{\delta \mathrm{t}}\Delta t = J_p\Delta t + F_p\Delta t + C_p\Delta t + V_p\Delta t + W_p\Delta t. \tag{4.96}$$

With each process treated in sequence via operator splitting. This is because the numerical behavior of different processes is quite different. For example, new-particle formation simply generates particle number (with a specified composition) in one or more bins over the specified time. Condensation is best treated with a moving sectional algorithm over the master time step, after which the resulting distribution is redistributed over the fixed size distribution, conserving mass (and composition) and number. The moving section is numerically stable, and number and mass conservation is straightforward, whereas treating the condensation step within the fixed distribution is quite unstable. Coagulation again removes and redistributes particles, which are also placed into bins within the fixed size distribution to conserve mass and number. Finally, wall loss and ventilation remove number (and mass), either as a uniform first-order removal for ventilation or a size-dependent first-order process for wall loss. As with any first-order finite difference scheme, the overall accuracy is fair, but it is well within the measurement precision of any instruments available even for relatively coarse time steps.

4.4.6.1. *Evolution of Two Narrow Seed Populations*

To explore the time evolution of a size distribution from the combined effects of condensation, coagulation, and wall loss, we shall consider a particle population consisting of two narrow but widely separate modes: one centered at 10 nm (number) diameter with a dispersity of 1.12 and an amplitude of 10^6 cm^{-3}, comprised initially of ammonium nitrate but modeled with a low density of 1.51 g cm^{-3} (the density of nitric acid), and one centered at 250 nm with a dispersity of 1.2 and an amplitude of 10^4 cm^{-3}, comprised initially of ammonium sulfate with a density of 1.77 g cm^{-3}. We show the initial number, collision frequency, and mass distributions in Fig. 4.40; the ammonium nitrate particles dominate the number distribution while the ammonium sulfate seeds dominate the mass distribution. For the condensation sink (the collision frequency), the two modes are more evenly matched, but the larger particles still constitute about 75% of the total. We use the lower density of nitric acid for the first mode so that the two seed populations have quite different densities, which makes testing the mass conservation of the numerics (based on volume equivalent diameter) easier to observe.

In addition to the losses, we consider condensation of organic vapors with a molecular weight of 250 g mole^{-1}, a density of 1.44 g cm^{-3}, and a vapor concentration of 0.1 μg m^{-3}. To simulate condensation of semi-volatile material, we scale the vapor concentration with a Kelvin like term $10^{-4\,\mathrm{nm}/d_p}$, consistent with a surface tension near 30 mN m^{-1} and a gas-phase saturation ratio slightly over one. This results in a growth rate from condensation shown as a function of diameter in Fig. 4.42, peaking near 15 nm h^{-1}. The Kelvin term only significantly influences growth when the effective activity in Eq. (4.39) competes with the gas-phase activity (saturation ratio); however, in the limiting case illustrated here when all of the condensing organics are semi-volatile, the effect can be dramatic for particles smaller than roughly $d_p \leq 10 \times d_{K10}$.

With all of these contributions, in Fig. 4.43, we show the overall rate of change of the size and mass distribution from condensation, coagulation, and wall loss (there is no nucleation), along with the net rate of change. As with the first example, condensation is the largest contributor to changes in the size distribution, but now the other terms are nontrivial as well.

We simulated 2 h of condensational growth by these organic vapors, and show the resulting number and mass distributions in

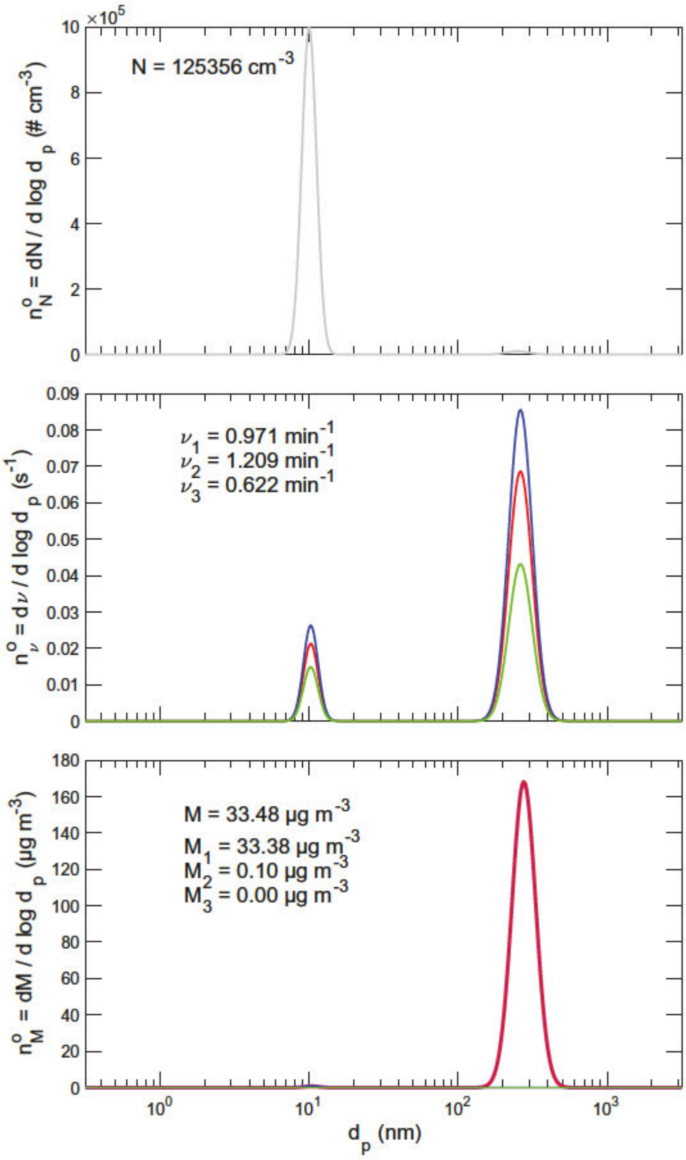

Fig. 4.40 Number, collision frequency, and mass distributions for 10 nm ammonium nitrate and 250 nm ammonium sulfate seed particles. Condensing vapors and mass composition includes three constituents, nominally sulfate, nitrate, and organics in that order.

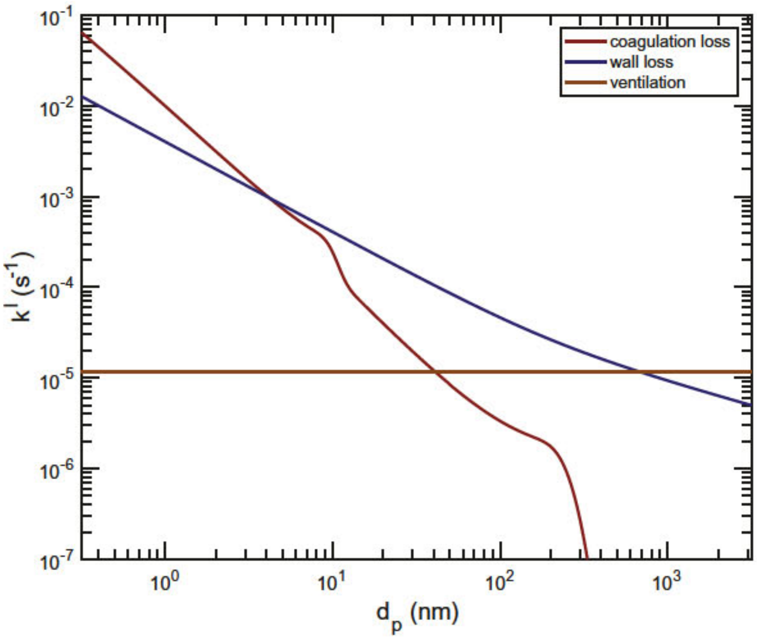

Fig. 4.41 Overall first-order loss frequencies for a two-mode lognormal number size distribution with 1.51 g cm^{-3} spherical particles centered at 10 nm and 1.77 g cm^{-3} spherical particles centered at 250 nm.

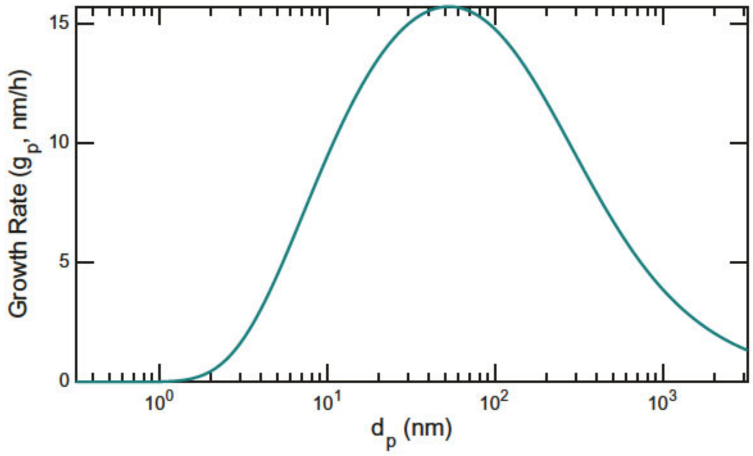

Fig. 4.42 Growth rate for condensation of 0.1 μg m^{-3} of semi-volatile organic vapors with a 4 nm decadal Kelvin diameter.

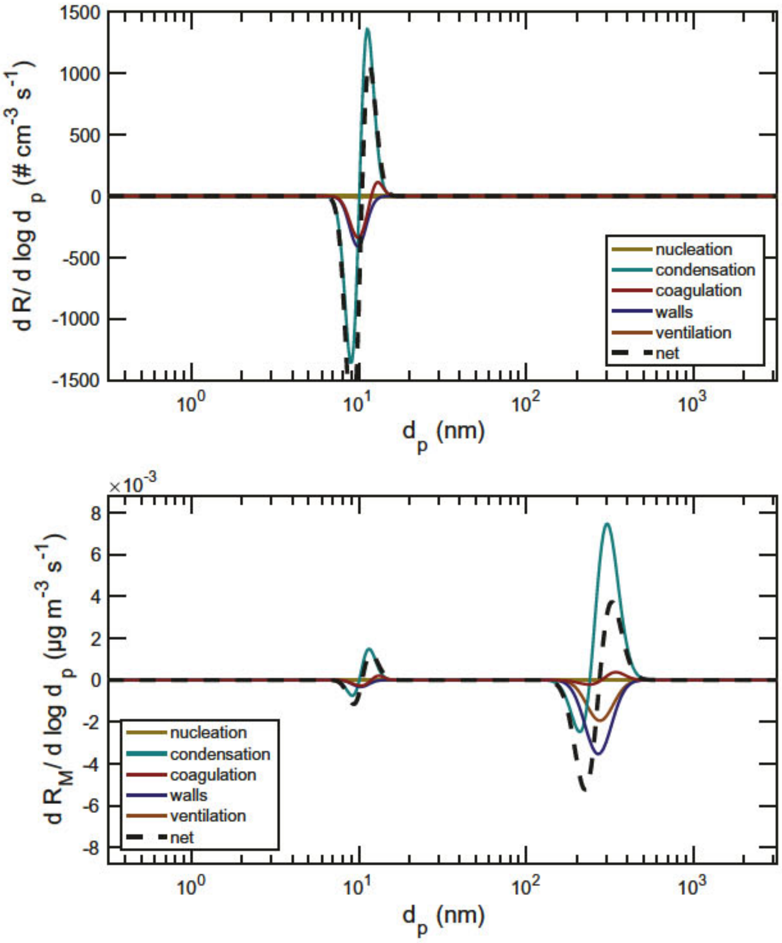

Fig. 4.43 Rate of change due to all causes of the number distribution (top) and mass distribution (bottom) for a bimodal lognormal number size distribution of 1.51 g cm^{-3} particles centered at 10 nm and 1.77 g cm^{-3} particles centered at 250 nm.

Fig. 4.44. The smaller 10 nm particles have grown to nearly 40 nm, consistent with a 15 nm h^{-1} growth rate, while the larger 250 nm particles have grown to 270 nm, as their growth rate is closer to 10 nm h^{-1}. Over this time interval, the total number has dropped precipitously from $N(0) \simeq 125000$ to $N(2\,\mathrm{h}) \simeq 17000$, whereas the

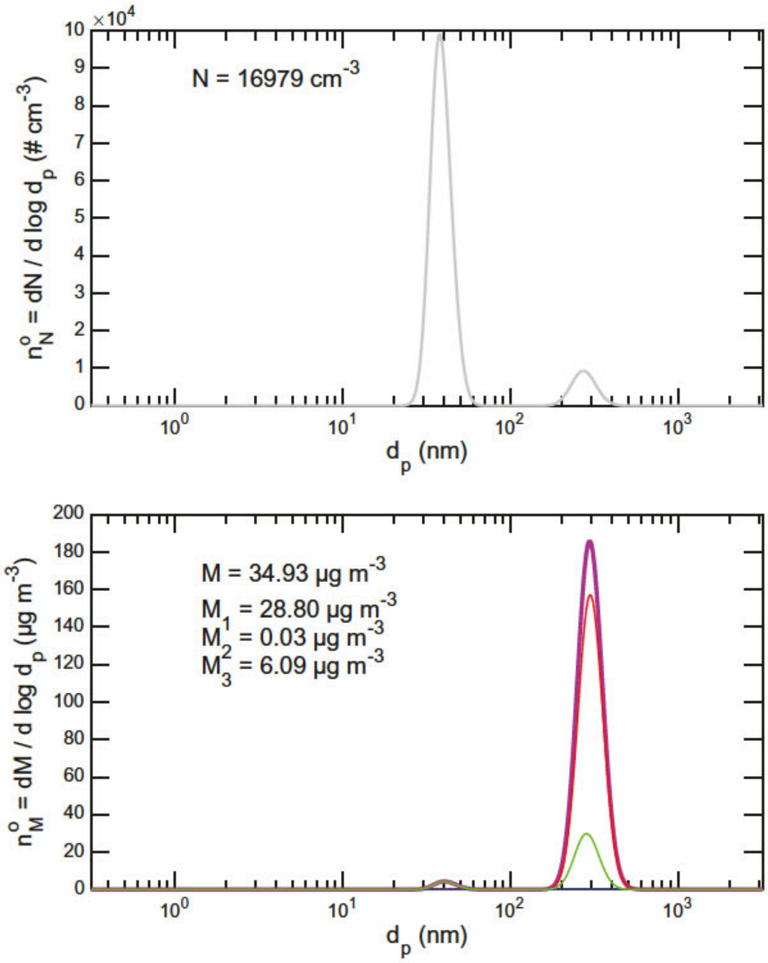

Fig. 4.44 Number and mass distributions for 10 nm ammonium nitrate and 250 nm ammonium sulfate particles, after 2 h of condensational growth driven by organic vapors. Mass composition includes three constituents, nominally sulfate, nitrate, and organics in that order.

total mass has increased slightly from $33.4\,\mu\mathrm{g\,m}^{-3}$ to $34.9\,\mu\mathrm{g\,m}^{-3}$, with $6.1\,\mu\mathrm{g\,m}^{-3}$ of new organic mass.

In Fig. 4.45, we show the composition as a function of size. The very smallest particles are pure nitrate and the very largest particles are pure sulfate because the size distributions at those limits are

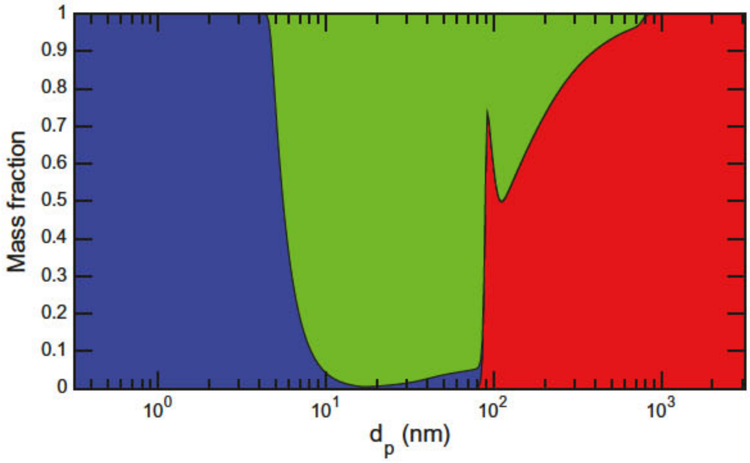

Fig. 4.45 Mass composition vs. size for two seed types (nitrate in blue, sulfate in red) after 2 h of condensational growth by organics (green).

vanishingly small, and the simulation retains the initial composition. For $5 \leq d_p \leq 800$ nm, there was significant organic condensation. The smaller particles are almost entirely organic, while the larger particles are still mostly sulfate; for both modes, the organic mass fraction is higher for smaller sizes, consistent with the collision frequency. Finally, on a mass basis essentially no nitrate is in the larger particles, as the coagulation number loss of smaller particles added very little mass to the larger particles.

In Fig. 4.46, we show the (time) integrated rates of number and mass change across the 2-h simulation. The smaller (nitrate) mode overwhelms the number distribution, while the larger (sulfate) mode dominates the mass distribution. In the smaller mode, wall losses slightly exceeded coagulation losses for the smaller mode, whereas condensation shifted the size, causing loss at the initial size and production at the final size. Because the relatively narrow small mode moved from 10 to 40 nm, the total change in number between 15 and about 30 nm is zero, with production from condensational growth balanced by wall and coagulation loss. For the larger particles, the growth was more of a shift than a transformation, and so the effect of condensation appears as a derivative shape, while coagulation has

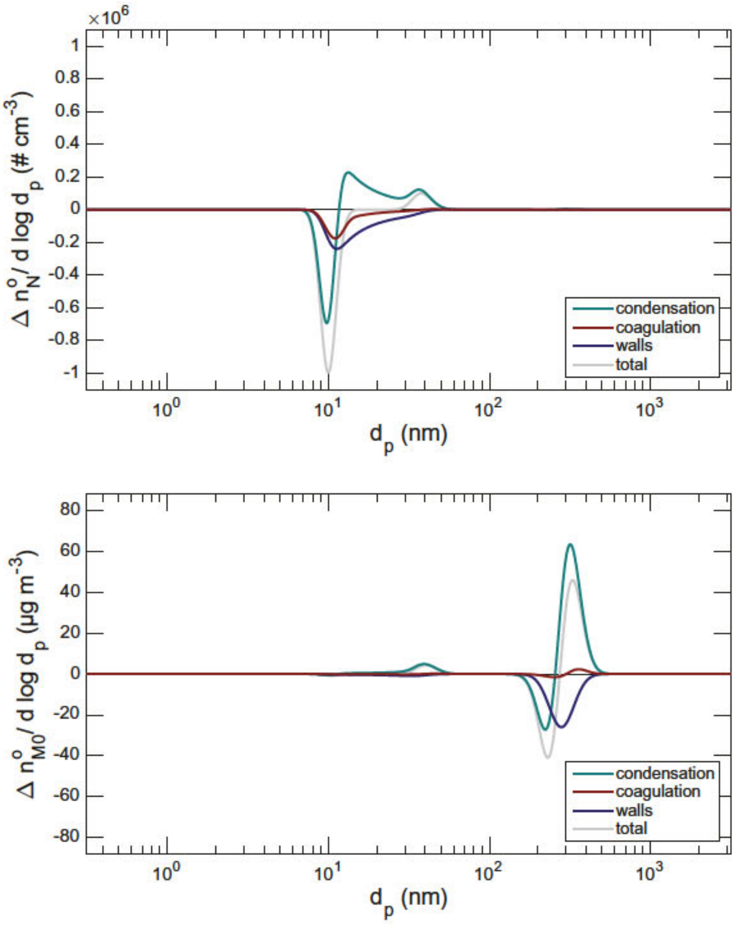

Fig. 4.46 Rate of change due to all causes of the number distribution (top) and mass distribution (bottom) for a bimodal lognormal number size distribution of 1.51 g cm^{-3} particles centered at 10 nm and 1.77 g cm^{-3} particles centered at 250 nm.

a small net contribution to the mass (balanced by a small loss in the smaller mode).

4.4.6.2. *Monodisperse Nucleation*

Finally, we shall consider two cases involving nucleation: one trivial case with nucleation but essentially no growth, and a second case with relatively fast growth. As a first test, we shall simulate a system with new-particle formation of sulfuric acid occurring for $d_p = 0.4\,\mathrm{nm}$, with $J_{0.4} = 10\,\mathrm{cm}^{-3}\mathrm{s}^{-1}$. For the first simulation, we include only a minimal condensational driving force, with $F^{v,h}_{i,p} = 10^{-5}\mu\mathrm{g\,m}^{-3}$; this is enough to drive about 0.015 nm h^{-1} of growth (less than 1 bin per hour), but the particle wall loss term at 0.4 nm is $\nu_{\mathrm{wall}} \simeq 0.01\,\mathrm{s}^{-1}$. In this situation, wall loss will thus completely dominate the dynamics, and we expect nucleation and wall losses to balance each other in a steady state with $\nu_{\mathrm{wall}}\,N \simeq J$, so $N^{\mathrm{ss}} \simeq J/\nu_{\mathrm{wall}} \simeq 1000\,\mathrm{cm}^{-3}$. In this case, we run a simulation for $0.3 \leq d_p \leq 30\,\mathrm{nm}$ because larger particles are irrelevant; the expected output is shown in Fig. 4.47. The rise timescale for the total particle number is also consistent with the 0.03 h particle lifetime against wall loss.

With the very small steady-state number concentration, there will also be no significant coagulation, but the near monodisperse distribution also serves as a test of the numerics, especially at the nearly gas-phase sizes. Specifically, the coagulation rate constant for 0.4 nm particles is $K_{\mathrm{coag}} = 3 \times 10^{-10}\,\mathrm{cm}^3\,\mathrm{s}^{-1}$, the well known hard-sphere collisional rate constant for gas kinetics. The expected first-order coagulation rate constant is thus $k^I_{\mathrm{coag}} = 10^3 \times 3 \times 10^{-10} = 3 \times 10^{-7}\,\mathrm{s}^{-1}$, and the coagulation rate is $R_{\mathrm{coag}} = 0.5 \times k^I_{\mathrm{coag}} \times N = 1.5 \times 10^{-4}\,\mathrm{cm}^{-3}\,\mathrm{s}^{-1}$ (the factor of 0.5 applies to identical objects, including particles of the same size). Both the wall loss balance and the effect of coagulation can be seen in Fig. 4.48. The integrated wall loss rate is slightly less than the nucleation rate due to our crude first-order numerical scheme, but the visual integral of the coagulation rates is the expected value (remembering that $\delta \log d_p = 0.01$).

4.4.6.3. *Homogeneous Nucleation and Growth*

As a second simulation, we shall still consider new-particle formation of sulfuric acid occurring for $d_p = 0.4\,\mathrm{nm}$, with $J_{0.4} = 10\,\mathrm{cm}^{-3}\,\mathrm{s}^{-1}$, but now with a sufficient condensation driving force for growth at about 10 nm h^{-1} (for 10 nm particles). These conditions are at the high end of the relatively clean atmospheric range. Here, we simulate a size distribution with $0.3 \leq d_p \leq 100\,\mathrm{nm}$ because the particles will

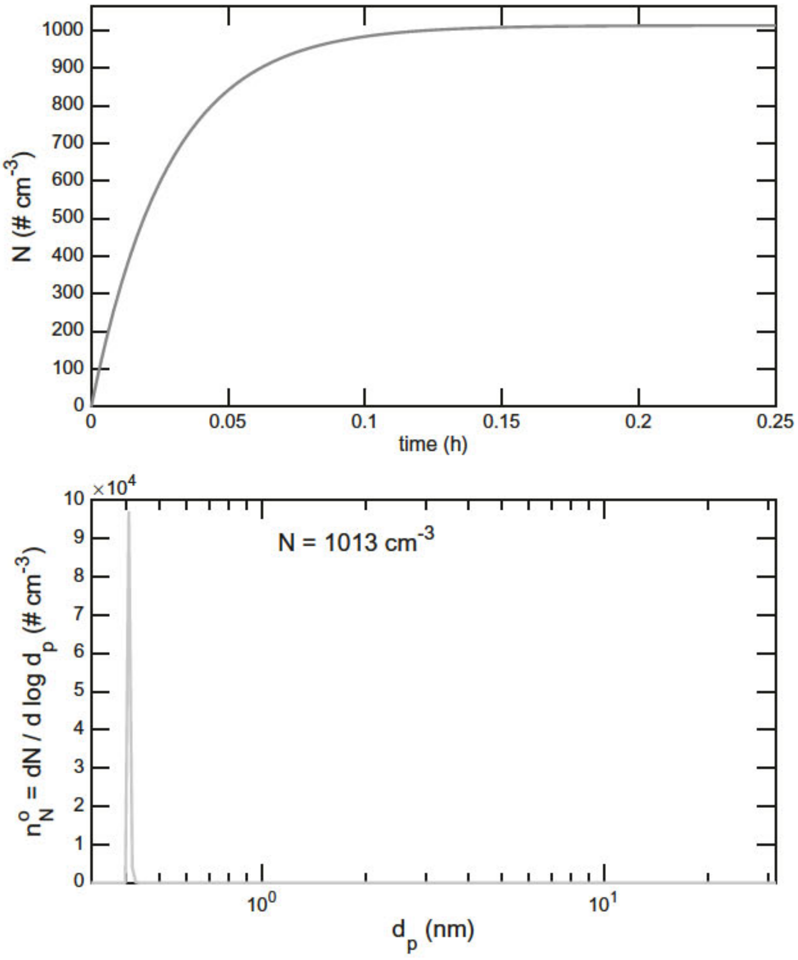

Fig. 4.47 Total particle number vs. time and the final size distribution for nucleation $J = 10\ \mathrm{cm}^{-3}\,\mathrm{s}^{-1}$ at $d_p = 0.4$ nm. There is almost no growth so the distribution remains monodisperse.

grow significantly over 4 h. In this case, $F_{i,p}^{v,h} = 0.04\,\mu\mathrm{g\,m}^{-3}$. The loss conditions simulate the CLOUD experiment at CERN,[90] with a turbulence parameter $k_e = 0.07\,\mathrm{s}^{-1}$ giving a first-order wall loss rate constant of just over $10^{-3}\,\mathrm{s}^{-1}$ for 1 nm particles and ventilation rate constant of $\nu_{\mathrm{vent}} = 1.4 \times 10^{-3}\,\mathrm{s}^{-1}$ (2 h). We show a time dependent diagnostic panel at the end of the 4-h simulation in Fig. 4.49.

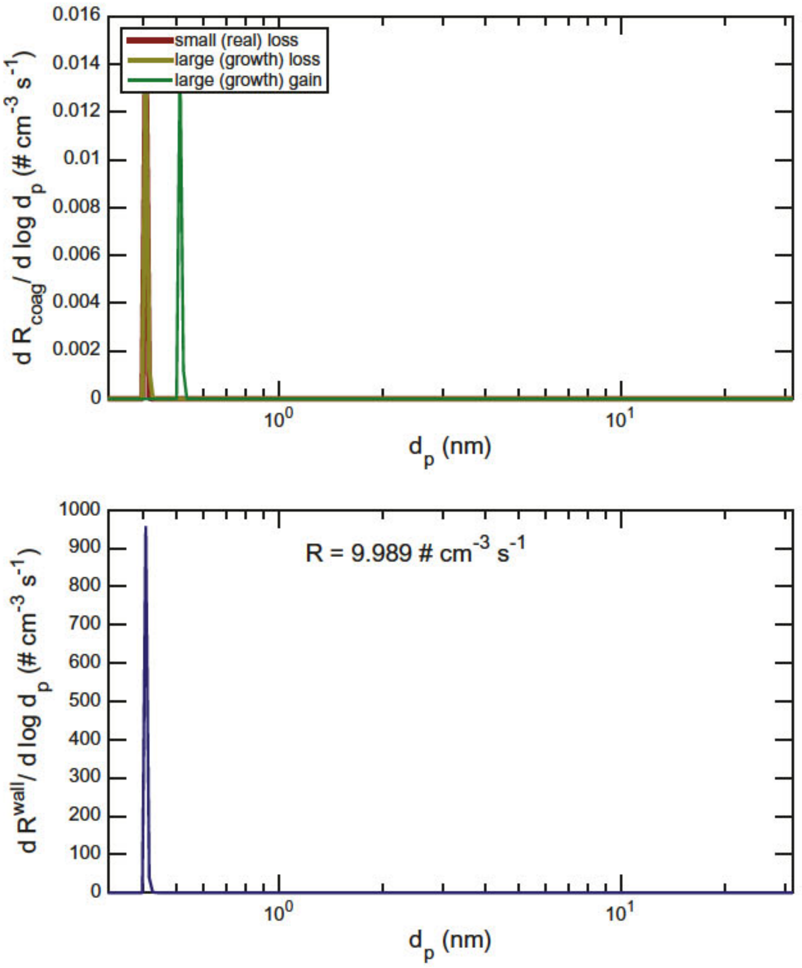

Fig. 4.48 Rates of coagulation and wall loss for nucleation at $J = 10$ cm^{-3} s^{-1} at $d_p = 0.4$ nm. Coagulation is negligible but leapfrogs multiple bins, while wall loss almost completely balances nucleation.

Several aspects of Fig. 4.49 warrant discussion. First, the number distribution is in a near steady state, as indicated in the lower left-hand panel. Because of this, the effective formation rate at any given size, J', will be given by a rough balance between production (condensational growth) and loss (wall losses and ventilation in this case). Later in the simulation, a sufficient particle surface area

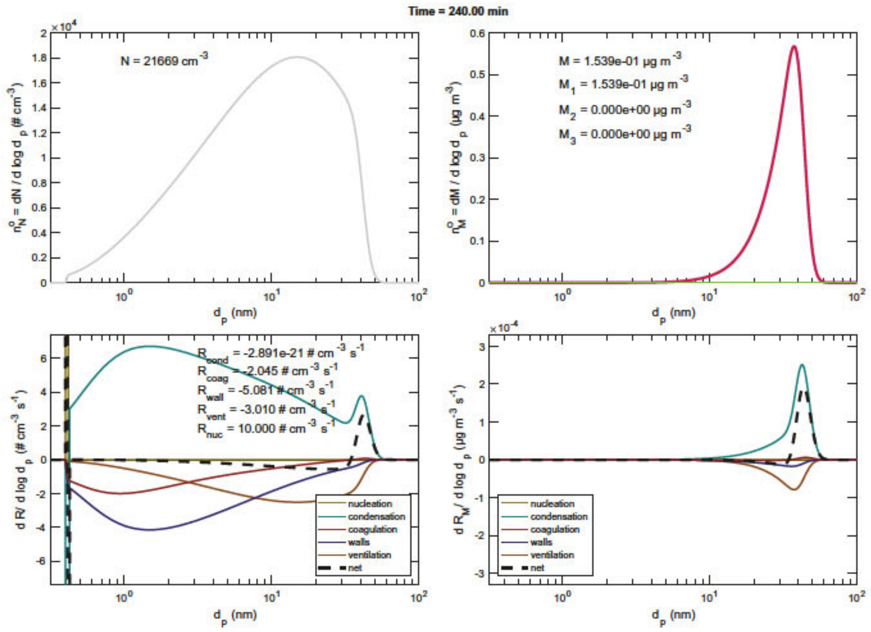

Fig. 4.49 Particle size distributions and rates for nucleation after 4 h at $J = 10\ \text{cm}^{-3}\,\text{s}^{-1}$ at $d_p = 0.4$ nm with significant condensational driving force (40 ng m^{-3} H_2SO_4). Growth averages about 10 nm h^{-1} and the mode front is at roughly 40 nm after 4 h. Left-hand panels are particle number, right hand panels are particle mass. Integrated condensation has no effect on number but a large effect on mass; condensation is a sink of particles at the nucleation diameter and a source elsewhere, with a substantial production front at the high limit of the number (and mass) mode.

has built up for coagulation to become a secondary sink, and as a consequence, the overall time derivative is slightly negative. As expected from the relative size dependence, wall loss is the dominant sink for the smallest particles while ventilation becomes dominant above 10 nm. Condensation cannot be a net source of number, and so it integrates to zero within error; however, condensation is a strong sink offsetting the nucleation source at the smallest size and becomes a source for most of the rest of the size range. That source consists of a broad region of net production by growth that is well balanced by the three loss terms and a formation front at the largest size reached (roughly 40 nm in this case). During the simulation that front advances with the growing distribution and gradually shrinks as the overall net production relaxes toward a steady state; again because of the emerging coagulation sink, by 4 h, the broad region of net loss has a slightly larger area than the formation front, and the net is $R \simeq -0.13$ # $\mathrm{cm}^{-3}\ \mathrm{s}^{-1}$. The balance between production and loss means in turn that the observed formation rates will be extremely sensitive to (carefully calibrated) wall loss rate constants; the loss terms in Eq. (4.75) are not corrections but rather the dominant terms.

Second, the near steady-state size distribution is very broad, with a maximum near 20 nm, in spite of the fact that condensation is the only significant source of number (after the nucleation impulse at 0.4 nm) and wall losses are the only significant sink. The maximum occurs because the intrinsic growth rate from condensation decelerates quickly with increasing size, as shown in Figs. 4.9 and 4.28. Consequently, for the distribution to be in steady state, the decreasing growth rate must be counterbalanced by an increasing distribution function, as observed. However, because the true growth rates for $d_p \lesssim 2\,\mathrm{nm}$ may be either strongly decreasing with size (for nonvolatile condensation) or strongly increasing with size (if a Kelvin term dominates), interpretation of data when instruments only sample particles larger than this can be fraught; explicit or implicit assumptions about the shape of the size dependence (increasing, constant, or decreasing) should be made with great care and met with skepticism.

Finally, the mass distribution function is much cleaner than the number distribution and also shows a very strong growth front, with a peak near 40 nm that is quite consistent with the 10 nm h^{-1} growth rate. Typical of nucleation experiments conducted under atmospheric conditions, the mass concentration even after 4 h is very low. This mass formation front may be the best experimental measure of the integrated growth rate at any given time, as it represents the mass weighted growth rate and thus is strongly localized toward the large end of the distribution. For the conditions simulated here, by the time the distribution reaches 40 nm, ventilation is also the dominant sink, making the necessary loss measurement far more accurate.

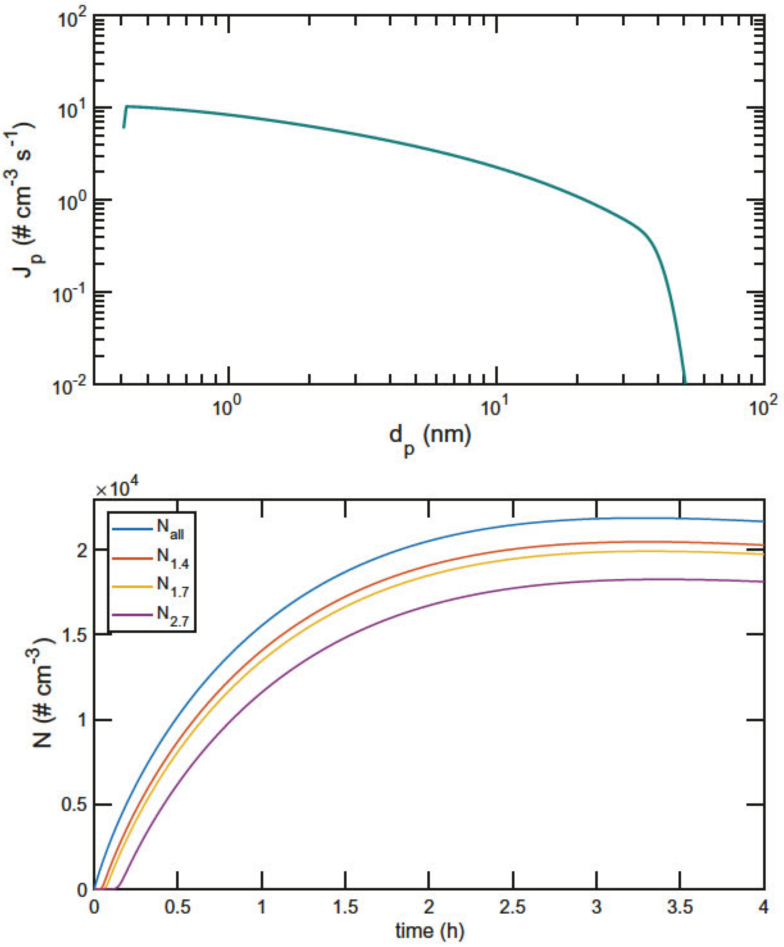

Fig. 4.50 Size dependent production rates and number vs. time for nucleation at $J = 10$ cm^{-3} s^{-1} at $d_p = 0.4$ nm.

The conditions of this simulation mean that condensational growth is the major loss out of the original 0.4 nm bin, so the production term J'_p at 0.4 nm from condensational growth should be 10 cm^{-3}s^{-1}. We show the production rate as well as integrated total number at four cut sizes in Fig. 4.50 (these are geometric sizes, so the mobility size is approximately $d_p + 0.3$ nm).[68] As expected, the maximum value of $J'_{0.4} \simeq 10\,\text{cm}^{-3}\,\text{s}^{-1}$, consistent with the nucleation rate. The nominal response curves of four condensation particle counters show sharp increases for the first hour or so, and then fall off toward a steady state. Often, particle formation and growth-rate determinations are based on particle counter data such as these.[91] Especially for the smallest sizes where coagulation and wall losses have very significant size dependencies, this analysis is not straightforward, and simulations such as these to ensure a self-consistent "story" regarding the particle size distribution are an important element of a complete analysis.

4.5. Discussion

This work consists of vignettes illustrating elements of an emerging, comprehensive framework describing the coupled interactions of organic oxidation chemistry and particle microphysics in the atmosphere. Each element can serve at least three roles: conceptual, diagnostic, and prognostic.

The conceptual role acts as an aide to intuition. With the 1D- and 2D-VBS, the oxidation kernels inform how organic material will move through the volatility and composition space while in the strongly oxidizing environment of the atmosphere. With the monodisperse condensation module, the framework enables consideration of nonequilibrium dynamics with a range of organic volatilities, e.g., focusing on the steady-state concentrations of condensible vapors during various stages of idealized experiments. Finally, the full microphysical sectional treatment helps experimental design by quantifying the various processes contributing to the evolution of the number size distribution, helping to ensure that experiments are actually sensitive to the specific process under investigation.

The diagnostic roles spring from the conceptual roles. VBS diagnostics inform interpretation of oxidation experiments and the bulk changes in composition driven during aerosol formation and aging. The monodisperse condensation module informs the dilution and mixing experiments illustrated in Section 4.3.3 and allows straightforward assessment of whether interpretation based on equilibrium assumptions is appropriate to a given setup. The full sectional algorithm is built around diagnostics, allowing calculation and visualization of individual partial derivatives to the evolving size distribution for any set of observations. The diagnostic panel in Fig. 4.49 is an example of the sort of output that should be ubiquitous during execution and interpretation of aerosol experiments.

Finally, as each element quantitatively relates to process rates, implementation of prognostic models is conceptually straightforward. In this work, we have kept the numerical simulations separate because the coupling between the elements can be numerically challenging and can also obscure the key features of the different phenomena. For example, condensation dynamics become numerically stiff with a wide range of organic volatilities, and so a submodule in the full sectional algorithm containing a wide-ranging VBS significantly increases the computational requirements. However, a complete coupling of these elements is the next step, along with inverse formulations connecting the diagnostic and prognostic modes to permit quantitative assessments of process rates from observations.[92]

The elements presented here are not complete. To implement the VBS oxidation kernels, the dynamical VBS needs to be combined with a gas-phase photochemical module including both photolysis rates and radical concentrations (so that the RO_2 branching chemistry and be properly constrained). Also, in the formulations presented here, the condensed-phase activity is a single value for each constituent, without radial gradients or chemical production and loss. As particle viscosity rises, it may become necessary to, at a minimum, separate the surface and bulk activities in particles.[47,51,93] In addition, it is clear that condensed-phase chemistry is important in both the organic and aqueous phases, but constraints remain incomplete on overall kinetics and mechanisms in realistic organic mixtures. Therefore, while we have shown that simplified condensed-phase chemistry schemes can reproduce observed aerosol behavior,[26,94] it remains unclear how best to describe overall condensed-phase chemistry in the VBS. A plausible hypothesis is that the highly oxidized compounds occupying the high O:C range of the 2D-VBS contain on average a rich mixture of oxygenated functional groups and so, in practice, rate constants for cross reactions in the condensed phase may be in some way a function of O:C. Finally, while we have acknowledged the important role that experimental surfaces (walls) can have on aerosol behavior,[22,57–59] the examples presented here do not couple wall interactions to the aerosol dynamics.

The atmospheric chemistry associated with organic aerosols continues to amaze. With dramatic improvements in aerosol instrumentation over the past decade, new observations have repeatedly demanded major revisions in the canonical picture of organic aerosols. Examples include the relative contribution of primary and secondary organics to overall burdens,[25,82] the role of condensed-phase association chemistry (oligomerization),[95,96] the importance of hard-to-measure IVOCs,[12] the relative role of first vs. later generation processes during the full life cycle of organics in the atmosphere,[15] and most recently the role of autooxidation chemistry to production of highly oxidized and extremely low volatility gas-phase compounds capable of driving new-particle formation.[7,23,28]

References

1. IPCC. *Climate Change 2013: The Physical Science Basis* (Cambridge University Press, New York, NY, 2013).
2. J. S. Apte, J. D. Marshall, A. J. Cohen and M. Brauer. Addressing global mortality from ambient $PM_{2.5}$. *Environ. Sci. Technol.* **49**(13), 8057–8066 (2015), doi:10.1021/acs.est.5b01236, pMID: 26077815.
3. J. L. Jimenez *et al.* Evolution of organic aerosols in the atmosphere. *Science* **326**, 1525–1529 (2009), doi:10.1126/science.1180353, http://www.sciencemag.org/cgi/content/abstract/326/5959/1525.
4. M. Canagaratna, J. L. Jimenez, J. Kroll, Q. Chen, S. Kessler, P. Massoli, L. Hildebrandt Ruiz, E. Fortner, L. Williams, K. Wilson, J. Surratt, N. M. Donahue, J. Jayne and D. Worsnop. Elemental ratio measurements of organic compounds using aerosol mass spectrometry: Characterization, improved calibration, and implications. *Atmos. Chem. Phys.* **15**, 253–272 (2015), doi:10.5194/acp-15-253-2015, http://www.atmos-chem-phys.net/15/253/2015/.
5. M. Ehn, E. Kleist, H. Junninen, T. Petäjä, G. Lönn, S. Schobesberger, M. Dal Maso, A. Trimborn, M. Kulmala, D. R. Worsnop, A. Wahner, J. Wildt and T. F. Mentel. Gas phase formation of extremely oxidized pinene reaction products in chamber and ambient air. *Atmos. Chem. Phys.* **12**(11), 5113–5127 (2012), doi:10.5194/acp-12-5113-2012, http://www.atmos-chem-phys.net/12/5113/2012/.

6. J. D. Crounse, L. B. Nielsen, S. Jørgensen, H. G. Kjaergaard and P. O. Wennberg. Autoxidation of organic compounds in the atmosphere. *J. Phys. Chem. Lett.* 4(20), 3513–3520 (2013), doi:10.1021/jz4019207.
7. M. Ehn *et al.* A large source of low-volatility secondary organic aerosol. *Nature* **506**, 476–479 (2014).
8. A. H. Goldstein and I. E. Galbally. Known and unexplored organic constituents in the Earth's atmosphere. *Environ. Sci. Technol.* **41**, 1515–1521 (2007).
9. J. H. Kroll, N. M. Donahue, J. L. Jimenez, S. Kessler, M. R. Canagaratna, K. Wilson, K. E. Alteri, L. R. Mazzoleni, A. S. Wozniak, H. Bluhm, E. R. Mysak, J. D. Smith, C. E. Kolb and D. R. Worsnop. Carbon oxidation state as a metric for describing the chemistry of atmospheric organic aerosol. *Nat. Chem.* **3**, 133–139 (2011), doi:10.1038/nchem.948, http://www.nature.com/nchem/journal/vaop/ncurrent/full/nchem.948.html.
10. N. M. Donahue, K. E. Huff Hartz, B. Chuong, A. A. Presto, C. O. Stanier, T. Rosenørn, A. L. Robinson and S. N. Pandis. Critical factors determining the variation in SOA yields from terpene ozonolysis: A combined experimental and computational study. *Faraday Discuss.* **130**, 295–309 (2005a), http://www.rsc.org/Publishing/Journals/FD/article.asp?doi=b417369d.
11. N. M. Donahue, A. L. Robinson, C. O. Stanier and S. N. Pandis. Coupled partitioning, dilution, and chemical aging of semivolatile organics. *Environ. Sci. Technol.* **40**, 2635–2643 (2006), doi:10.1021/es052297c.
12. A. L. Robinson, N. M. Donahue, M. K. Shrivastava, A. M. Sage, E. A. Weitkamp, A. P. Grieshop, T. E. Lane, J. R. Pierce and S. N. Pandis. Rethinking organic aerosols: Semivolatile emissions and photochemical aging. *Science* **315**, 1259–1263 (2007), doi:10.1126/science.1133061, http://www.sciencemag.org/cgi/content/full/315/5816/1259.
13. N. M. Donahue, S. A. Epstein, S. N. Pandis and A. L. Robinson. A two-dimensional volatility basis set: 1. Organic mixing thermodynamics. *Atmos. Chem. Phys.* **11**, 3303–3318 (2011b), doi:10.5194/acp-11-3303-2011, http://www.atmos-chem-phys.net/11/3303/2011/.
14. N. M. Donahue, J. H. Kroll, A. L. Robinson and S. N. Pandis. A two-dimensional volatility basis set — part 2: Diagnostics of organic-aerosol evolution. *Atmos. Chem. Phys.* **12**, 615–634 (2012b), doi:10.5194/acp-12-615-2012, http://www.atmos-chem-phys.net/12/615/2012/.
15. N. M. Donahue *et al.* Aging of biogenic secondary organic aerosol via gas-phase OH radical reactions. *Proc. Nat. Acad. Sci. USA.* **109**, 13503–13508 (2012a), doi:10.1073/pnas.1115186109, http://www.pnas.org/content/109/34/13503.abstract.
16. N. M. Donahue, W. K. Chuang, S. A. Epstein, J. H. Kroll, D. R. Worsnop, A. L. Robinson, P. J. Adams and S. N. Pandis. Why do organic aerosols exist? Understanding aerosol lifetimes using the two-dimensional volatility basis set. *Environ. Chem.* **10**, 151–157 (2013a), doi:10.1071/EN13022.
17. W. K. Chuang and N. M. Donahue. A 2-dimensional volatility basis set — part 3: Prognostic modeling and NO_x dependence. *Atmos. Chem. Phys.*

16, 123–134 (2016), doi:10.5194/acp-16-123-2016, http://www.atmos-chem-phys.net/16/123/2016/.

18. H. J. Chacon-Madrid, B. N. Murphy, S. N. Pandis and N. M. Donahue. Simulations of smog-chamber experiments using the two-dimensional-volatility basis set: Linear oxygenated precursors. *Environ. Sci. Technol.* **46**, 11179–11186 (2012), doi:10.1021/es3017232, http://pubs.acs.org/doi/abs/10.1021/es3017232.
19. A. A. Presto and N. M. Donahue. Investigation of α-pinene + ozone secondary organic aerosol formation at low total aerosol mass. *Environ. Sci. Technol.* **40**, 3536–3543 (2006), doi:10.1021/es052203z.
20. K. M. Henry and N. M. Donahue. Effect of the OH radical scavenger hydrogen peroxide on secondary organic aerosol formation from α-pinene ozonolysis. *Aerosol Sci. Technol.* **45**, 686–690 (2011), doi:10.1080/02786826.2011.552926, http://www.informaworld.com/smpp/content~db=all~content=a933399706~frm=titlelink.
21. E. R. Trump, I. Riipinen and N. M. Donahue. Modeling the condensational growth of nanoparticles in the atmosphere. *Boreal Environ. Res.* **19**, 352–362 (2014), http://www.borenv.net/BER/pdfs/ber19/ber19-352.pdf.
22. E. R. Trump, S. A. Epstein, I. Riipinen and N. M. Donahue. Wall effects in smog chamber experiments: A model study. *Aerosol Sci. Technol.* **50**(11), 1180–1200 (2016), doi:10.1080/02786826.2016.1232858.
23. J. Tröstl *et al.* The role of low-volatility organic compounds in initial particle growth in the atmosphere. *Nature* **530**, 527–531 (2016), doi:10.1038/nature18271.
24. S. A. Epstein, I. Riipinen and N. M. Donahue. A semiempirical correlation between enthalpy of vaporization and saturation concentration for organic aerosol. *Environ. Sci. Technol.* **44**, 743–748 (2010), doi:10.1021/es902497z, http://pubs.acs.org/doi/abs/10.1021/es902497z.
25. N. M. Donahue, A. L. Robinson and S. N. Pandis. Atmospheric organic particulate matter: From smoke to secondary organic aerosol. *Atmos. Environ.* **43**, 94–106 (2009), doi:10.1016/j.atmosenv.2008.09.055.
26. W. K. Chuang and N. M. Donahue. Extremely Low Volatility Organic Compounds (ELVOCs), dynamics, and smog-chamber secondary organic aerosol formation. *Atmos. Chem. Phys.* **17**, 10019–10036 (2017), doi:10.5194/acp-17-10019-2017.
27. N. M. Donahue, E. R. Trump, I. Riipinen and J. R. Pierce. Theoretical constraints on pure vapor-pressure driven condensation of organics to ultrafine particles. *Geophys. Res. Lett.* **38**, L16801 (2011c), doi:10.1029/2011GL048115, http://www.agu.org/pubs/crossref/2011/2011GL048115.shtml.
28. J. Kirkby *et al.* Ion-induced nucleation of pure biogenic particles, *Nature* **530**, 521–526 (2016), doi:10.1038/nature17953.
29. C. Frege *et al.* Influence of temperature on the molecular composition of ions and charged clusters during pure biogenic nucleation. *Atmos. Chem. Phys.* **18**, 65–79, doi:10.5194/acp-2017-426, http://www.atmos-chem-phys-discuss.net/acp-2017-426/.

30. R. Atkinson and J. Arey. Atmospheric degradation of volatile organic compounds. *Chem. Rev.* **103**(12), 4605–4638 (2003), doi:10.1021/cr0206420.
31. N. M. Donahue, G. T. Drozd, S. A. Epstein, A. A. Presto and J. H. Kroll. Adventures in ozoneland: Down the rabbit-hole. *Phys. Chem. Chem. Phys.* **13**, 10848–10857 (2011a), doi:10.1039/c0cp02564j, http://pubs.rsc.org/en/Content/ArticleLanding/2011/CP/c0cp02564j.
32. J. Hakala and N. M. Donahue. Pressure dependent Criegee Intermediate stabilization from alkene ozonolysis. *J. Phys. Chem. A* **120**, 2173–2178 (2016), doi:10.1021/acs.jpca.6b01538.
33. M. P. Rissanen *et al.* The formation of highly oxidized multifunctional products in the ozonolysis of cyclohexene. *J. Am. Chem. Soc.* **136**(44), 15596–15606 (2014), doi:10.1021/ja507146s, pMID: 25283472.
34. J. R. Odum, T. Hoffmann, F. Bowman, D. Collins, R. C. Flagan and J. H. Seinfeld. Gas/particle partitioning and secondary organic aerosol yields. *Environ. Sci. Technol.* **30**(8), 2580–2585 (1996).
35. R. Griffin, D. Cocker, R. Flagan and J. Seinfeld. Organic aerosol formation from the oxidation of biogenic hydrocarbons. *J. Geophys. Res. Atmos.* **104**, 3555 (1999).
36. M. Bilde *et al.* Saturation vapor pressures and transition enthalpies of low-volatility organic molecules of atmospheric relevance: From dicarboxylic acids to complex mixtures. *Chem. Rev.* **115**, 4115–4156 (2015), doi:10.1021/cr5005502, https://pubs.acs.org/doi/abs/10.1021/cr5005502.
37. J. F. Pankow and W. E. Asher. SIMPOL.1: A simple group contribution method for predicting vapor pressures and enthalpies of vaporization of multifunctional organic compounds. *Atmos. Chem. Phys.* **8**(10), 2773–2796 (2008).
38. T. Kurtén, K. Tiusanen, P. Roldin, M. Rissanen, J.-N. Luy and N. M. Donahue. Saturation vapor pressures of α -pinene autoxidation products may be severely underpredicted by group contribution methods, *J. Phys. Chem. A* **120**, 2569–2582 (2016), doi:10.1021/acs.jpca.6b02196.
39. D. M. Westervelt, J. R. Pierce, I. Riipinen, W. Trivitayanurak, A. Hamed, M. Kulmala, A. Laaksonen, S. Decesari and P. J. Adams. Formation and growth of nucleated particles into cloud condensation nuclei: Model–measurement comparison. *Atmos. Chem. Phys.* **13**(15), 7645–7663 (2013), doi:10.5194/acp-13-7645-2013, http://www.atmos-chem-phys.net/13/7645/2013/.
40. S. Madronich and J. G. Calvert. Atmospheric chemistry of small organic peroxy radicals. *J. Geophys. Res. Atmos.* **95**, 5697 (1990).
41. P. D. Lightfoot, R. A. Cox, J. N. Crowley, M. Destriau, G. D. Hayman, M. E. Jenken, G. K. Moortgat and F. Zabel. Organic peroxy radicals: Kinetics, spectroscopy, and atmospheric chemistry. *Atmos. Environ.* **26**, 1805–1961 (1992).
42. G. S. Tyndall, R. A. Cox, C. Granier, R. Lesclaux, G. K. Moortgat, M. J. Pilling, A. R. Ravishankara and T. J. Wallington. Atmospheric chemistry of small organic peroxy radicals. *J. Geophys. Res. Atmos.* **106**, 12157 (2001).

43. J. H. Kroll, J. D. Smith, D. L. Che, S. H. Kessler, D. R. Worsnop and K. R. Wilson. Measurement of fragmentation and functionalization pathways in the heterogeneous oxidation of oxidized organic aerosol. *Phys. Chem. Chem. Phys.* **11**(36), 8005–8014 (2009), doi:10.1039/b905289e.
44. M. Kulmala *et al.* Direct observations of atmospheric aerosol nucleation. *Science* **339**(6122), 943–946 (2013), doi:10.1126/science.1227385, http://www.sciencemag.org/content/339/6122/943.full.pdf, http://www.sciencemag.org/content/339/6122/943.abstract.
45. J. R. Pierce and P. J. Adams. Efficiency of cloud condensation nuclei formation from ultrafine particles. *Atmos. Chem. Phys.* **7**, 1367–1379 (2007).
46. D. R. Worsnop, J. W. Morris, Q. Shi, P. Davidovits and C. E. Kolb. A chemical kinetic model for reactive transformations of aerosol particles. *Geophys. Res. Lett.* **29**, 57 (2002).
47. N. M. Donahue, A. L. Robinson, K. E. Huff Hartz, A. M. Sage and E. A. Weitkamp. Competitive oxidation in atmospheric aerosols: The case for relative kinetics. *Geophys. Res. Lett.* **32**, L16805 (2005b), doi:10.1029/2005GL 022893, http://www.agu.org/pubs/crossref/2005.../2005GL022893. shtml.
48. A. Virtanen, J. Joutsensaari, T. Koop, J. Kannosto, P. Yli-Pirila, J. Leskinen, J. M. Makela, J. K. Holopainen, U. Poeschl, M. Kulmala, D. R. Worsnop and A. Laaksonen. An amorphous solid state of biogenic secondary organic aerosol particles. *Nature* **467**(7317), 824–827 (2010), doi:10.1038/nature09455.
49. T. D. Vaden, C. Song, R. A. Zaveri, D. Imre and A. Zelenyuk. Morphology of mixed primary and secondary organic particles and the adsorption of spectator organic gases during aerosol formation. *Proc. Nat. Acad. Sci. USA.* **107**(15), 6658–6663 (2010), doi:10.1073/pnas.0911206107.
50. T. Koop, J. Bookhold, M. Shiraiwa and U. Poeschl. Glass transition and phase state of organic compounds: Dependency on molecular properties and implications for secondary organic aerosols in the atmosphere. *Phys. Chem. Chem. Phys.* **13**(43), 19238–19255 (2011), doi:10.1039/c1cp22617g.
51. M. Shiraiwa, M. Ammann, T. Koop and U. Poeschl. Gas uptake and chemical aging of semisolid organic aerosol particles. *Proc. Nat. Acad. Sci. USA.* **108**(27), 11003–11008 (2011), doi:10.1073/pnas.1103045108.
52. M. Shiraiwa, L. D. Yee, K. A. Schilling, C. L. Loza, J. S. Craven, A. Zuend, P. J. Ziemann and J. H. Seinfeld. Size distribution dynamics reveal particle-phase chemistry in organic aerosol formation. *Proc. Nat. Acad. Sci. USA.* **110**, 11746–11750 (2013), doi:10.1073/pnas.1307501110.
53. S. Schobesberger *et al.* Molecular understanding of atmospheric particle formation from sulfuric acid and large oxidized organic molecules. *Proc. Nat. Acad. Sci. USA.* **110**, 17223–17228 (2013), doi:10.1073/pnas.1306973110, http://www.pnas.org/cgi/doi/10.1073/pnas.1306973110.
54. F. Riccobono *et al.* Oxidation products of biogenic emissions contribute to nucleation of atmospheric particles. *Science* **344**, 717–721 (2014), doi:10.1126/science.1243527, http://www.sciencemag.org/content/344/6185/717.abstract.

55. P. Ye, W. K. Chuang, Y. Zhao and N. M. Donahue. Secondary organic aerosol formation from oxidation of pinanediol. *Atmos. Chem. Phys. Discuss.*, (2018a), web.
56. J. H. Kroll, A. W. H. Chan, N. L. Ng, R. C. Flagan and J. H. Seinfeld. Reactions of semivolatile organics and their effects on secondary organic aerosol formation. *Environ. Sci. Technol.* **41**(10), 3545–3550 (2007), doi:10.1021/es062059x.
57. A. Matsunaga and P. J. Ziemann. Gas-wall partitioning of organic compounds in a teflon film chamber and potential effects on reaction product and aerosol yield measurements. *Aerosol Sci. Technol.* **44**(10), 881–892 (2010), doi:10.1080/02786826.2010.501044.
58. P. Ye, X. Ding, J. Hakala, V. Hofbauer, E. S. Robinson and N. M. Donahue. Vapor wall loss of semi-volatile organic compounds in a teflon chamber. *Aerosol Sci. Technol.* **50**, 822–834 (2016a), doi:10.1080/02786826.2016.1195905.
59. J. E. Krechmer, D. Pagonis, P. J. Ziemann and J. L. Jimenez. Quantification of gas-wall partitioning in teflon environmental chambers using rapid bursts of low-volatility oxidized species generated in situ. *Environ. Sci. Technol.* **50**(11), 5757–5765 (2016), doi:10.1021/acs.est.6b00606, pMID: 27138683.
60. T. Yli-Juuti, K. Barsanti, L. Hildebrandt Ruiz, A.-J. Kieloaho, U. Makkonen, T. Petäjä, T. Ruuskanen, M. Kulmala and I. Riipinen. Model for acid-base chemistry in nanoparticle growth (MABNAG). *Atmos. Chem. Phys.* **13**(24), 12507–12524 (2013), doi:10.5194/acp-13-12507-2013, https://www.atmos-chem-phys.net/13/12507/2013/.
61. L. Ahlm *et al.* Modeling the thermodynamics and kinetics of sulfuric acid-dimethylamine-water nanoparticle growth in the CLOUD chamber. *Aerosol Sci. Technol.* **50**, 1017–1032 (2016), doi:10.1080/02786826.2016.1223268.
62. Y. Zhang, C. Seigneur, J. H. Seinfeld, M. Z. Jacobson and F. S. Binkowski. Simulation of aerosol dynamics: A comparative review of algorithms used in air quality models. *Aerosol Sci. Technol.* **31**(6), 487–514 (1999), doi:10.1080/027868299304039.
63. J. H. Seinfeld, L. E. Nohl and S. N. Pandis. *Atmospheric Chemistry and Physics from Air Pollution to Climate Change*, 3rd edn. (Wiley), doi:isbnvs.
64. T. Nieminen, K. E. J. Lehtinen and M. Kulmala. Sub-10 nm particle growth by vapor condensation-effects of vapor molecule size and particle thermal speed. *Atmos. Chem. Phys.* **10**(20), 9773–9779 (2010), doi:10.5194/acp-10-9773-2010.
65. N. A. Fuchs and A. G. Sutugin, A. G. (1971). *Topics in Current Aerosol Research (Part 2)*, chap. High dispersed aerosols (Pergamon), pp. 1–200.
66. P. H. McMurry and D. Grosjean. Gas and aerosol wall losses in Teflon film smog chambers. *Environ. Sci. Technol.* **19**, 1176–1181 (1985).
67. T. R. Marrero and E. A. Mason. Gaseous diffusion coefficients. *J. Phys. Chem. Ref. Data* **1**(1), 3–118 (1972), doi:10.1063/1.3253094.
68. C. Larriba, C. J. Hogan Jr., M. Attoui, R. Borrajo, J. F. Garcia and J. F. de la Mora. The mobility–volume relationship below 3.0 nm examined by

tandem mobility–mass measurement. *Aerosol Sci. Technol.* **45**(4), 453–467 (2011), doi:10.1080/02786826.2010.546820, http://www.tandfonline.com/doi/pdf/10.1080/02786826.2010.546820.

69. K. E. Gustafson and R. M. Dickhut. Molecular diffusivity of polycyclic aromatic hydrocarbons in aqueous solution. *J. Chem. Eng. Data* **39**(2), 281–285 (1994), doi:10.1021/je00014a019.
70. N. M. Donahue, I. K. Ortega, W. Chuang, I. Riipinen, F. Riccobono, S. Schobesberger, J. Dommen, U. Baltensperger, M. Kulmala, D. R. Worsnop and H. Vehkamaki. How do organic vapors contribute to new-particle formation? *Faraday Discuss.* **16**, 91–104 (2013b), doi:10.1039/C3FD00046J, http://pubs.rsc.org/en/content/articlelanding/2013/fd/c3fd00046j.
71. R. Saleh, N. M. Donahue and A. L. Robinson. Time scales for gas-particle partitioning equilibration of secondary organic aerosol formed from alpha-pinene ozonolysis. *Environ. Sci. Technol.* **47**, 5588–5594 (2013), doi:10.1021/es400078d.
72. A. Sinha, R. Saleh, E. S. Robinson, A. T. Ahern, D. S. Tkacik, A. A. Presto, R. C. Sullivan, A. L. Robinson and N. M. Donahue. Mass accommodation coefficient of fresh and aged biomass burning emissions. *Aerosol Sci. Technol.* **52**, 300–309, doi:10.1080/02786826.2017.1413488.
73. N. M. Donahue, A. L. Robinson, E. R. Trump, I. Riipinen and J. H. Kroll, J. H. (2014). *Atmospheric and Aerosol Chemistry, Topics in Current Chemistry*, Vol. 339, chap. Volatility and Aging of Atmospheric Organic Aerosols (Springer), pp. 97–144, doi:10.1007/128_2012_355, http://www.springerlink.com/content/n53082n87324462r/.
74. R. Saleh and A. Khlystov. Determination of activity coefficients of semi-volatile organic aerosols using the integrated volume method. *Aerosol Sci. Technol.* **43**(8), 838–846 (2009).
75. J. Julin, P. M. Winkler, N. M. Donahue, P. E. Wagner and I. Riipinen. Surface and bulk accommodation of organic molecules of varying structure. *Environ. Sci. Technol.* **48**, 12083–12089 (2014), doi:10.1021/es501816h, http://pubs.acs.org/doi/pdf/10.1021/es501816h.
76. F. D. Lopez-Hilfiker, C. Mohr, M. Ehn, F. Rubach, E. Kleist, J. Wildt, T. F. Mentel, A. Lutz, M. Hallquist, D. Worsnop and J. A. Thornton. A novel method for online analysis of gas and particle composition: Description and evaluation of a filter inlet for gases and aerosols (FIGAERO). *Atmos. Meas. Tech.* **7**(4), 983–1001 (2014), doi:10.5194/amt-7-983-2014, http://www.atmos-meas-tech.net/7/983/2014/.
77. L. Hildebrandt, E. Kostenidou, V. A. Lanz, A. S. H. Prévôt, U. Baltensperger, N. Mihalopoulos, A. Laaksonen, N. M. Donahue and S. N. Pandis. Sources and atmospheric processing of organic aerosol in the Mediterranean: Insights from aerosol mass spectrometer factor analysis. *Atmos. Chem. Phys.* **11**, 12499–12515 (2011b), doi:10.5194/acp-11-12499-2011, http://www.atmos-chem-phys.net/11/12499/2011/.
78. E. S. Robinson, T. J. Onasch, D. Worsnop and N. M. Donahue. Collection efficiency of α-pinene secondary organic aerosol particles explored

via light-scattering single-particle aerosol mass spectrometry. *Atmos. Meas. Tech.* **10**, 1139–1154 (2017), doi:10.5194/amt-10-1139-2017, http://www.atmos-meas-tech.net/10/1139/2017/.

79. L. Hildebrandt, N. M. Donahue and S. N. Pandis. High formation of secondary organic aerosol from the photo-oxidation of toluene. *Atmos. Chem. Phys.* **9**, 2973–2986 (2009), http://www.atmos-chem-phys.net/9/2973/2009/.
80. E. S. Cross, J. G. Slowik, P. Davidovits, J. D. Allan, D. R. Worsnop, J. T. Jayne, D. K. Lewis, M. Canagaratna and T. B. Onasch. Laboratory and ambient particle density determinations using light scattering in conjunction with aerosol mass spectrometry. *Aerosol Sci. Technol.* **41**(4), 343–359 (2007), doi:10.1080/02786820701199736.
81. N. L. Ng, P. S. Chhabra, A. W. H. Chan, J. D. Surratt, J. H. Kroll, A. J. Kwan, D. C. McCabe, P. O. Wennberg, A. Sorooshian, S. M. Murphy, N. F. Dalleska, R. C. Flagan and J. H. Seinfeld. Effect of nox level on secondary organic aerosol (soa) formation from the photooxidation of terpenes. *Atmos. Chem. Phys.* **7**(19), 5159–5174 (2007).
82. J. Zhang, K. E. Huff Hartz, S. N. Pandis and N. M. Donahue. Secondary organic aerosol formation from limonene ozonolysis: Homogeneous and heterogeneous influences as a function of NO_x. *J. Phys. Chem. A* **110**, 11053–11063 (2006), doi:10.1021/jp062836f.
83. E. S. Robinson, R. Saleh and N. M. Donahue. Mixing of individual organic aerosol particles via gas-phase exchange. *J. Phys. Chem. A* **117**, 13935–13945 (2013), doi:10.1021/jp405789t, http://pubs.acs.org/doi/pdf/10.1021/jp405789t.
84. Q. Ye, E. S. Robinson, P. Ye, X. Ding, R. C. Sullivan and N. M. Donahue. Single-particle measurements of semi-volatile secondary organic aerosol mixing versus relative humidity. *Proc. Nat. Acad. Sci. USA.* **113**, 12649–12654 (2016b), doi:10.1073/pnas.1604536113, http://www.pnas.org/content/early/2016/10/21/1604536113.abstract.
85. E. S. Robinson, N. M. Donahue, Q. Ye, A. T. Ahern and E. M. Lipsky. Single-particle measurements of phase partitioning between primary and secondary organic aerosols. *Faraday Discuss.* **189**, 31–49 (2016), doi:10.1039/C5FD00214A, http://pubs.rsc.org/en/content/article landing/2016/fd/c5fd00214a.
86. L. Hildebrandt, K. M. Henry, J. H. Kroll, D. R. Worsnop, S. N. Pandis and N. M. Donahue. Evaluating the mixing of organic aerosol components using high-resolution aerosol mass spectrometry. *Environ. Sci. Technol.* **45**, 6329–6335 (2011a), doi:10.1021/es200825g.
87. E. S. Robinson, R. Saleh and N. M. Donahue. Probing the evaporation dynamics of mixed SOA/squalane particles using size-resolved composition and single-particle measurements. *Environ. Sci. Technol.* **49**, 9724–9732 (2015), doi:10.1021/acs.est.5b01692, http://pubs.acs.org/doi/abs/10.1021/acs.est.5b01692.

88. Q. Ye, M. A. Upshur, E. S. Robinson, R. J. Thomson, R. C. Sullivan, F. M. Geiger and N. M. Donahue. Probing semi-volatile mixing of atmospheric secondary organic aerosols from terpenes using isotopically labeled reagents and single-particle mass spectrometers. *Chem* **4**, in press (2018b).
89. P. J. Adams and J. H. Seifeld. Predicting global aerosol size distributions in general circulation models. *J. Geophys. Res. Atmos.* **107**, 4370 (2002).
90. J. Duplissy *et al.* Effect of ions on sulfuric acid-water binary particle formation II: Experimental data and comparison with QC-normalized classical nucleation theory. *J. Geophys. Res. Atmos.* **212**, 1752–1775 (2016), doi:10.1002/2015JD023539.
91. K. Lehtipalo, J. Leppä, J. Kontkanen, J. Kangasluoma, A. Franchin, D. Wimmer, S. Schobesberger, H. Junninen, T. Petäjä, M. Sipilä, J. Mikkilä, J. Vanhanen, D. R. Worsnop and M. Kulmala. Methods for determining particle size distribution and growth rates between 1 and 3 nm using the particle size magnifier. *Boreal Environ. Res.* **19**, 215–236 (2014), http://www.borenv.net/BER/pdfs/ber19/ber19B-215.pdf.
92. J. R. Pierce, G. J. Engelhart, L. Hildebrandt, E. A. Weitkamp, R. K. Pathak, S. N. Pandis, N. M. Donahue, A. L. Robinson and P. J. Adams. Constraining particle evolution from wall losses, coagulation, and condensation-evaporation in smog-chamber experiments: Optimal estimation based on size distribution measurements. *Aerosol Sci. Technol.* **42**, 1001–1015 (2008), doi:10.1080/02786820802389251, http://www.informaworld.com/smpp/content~content=a903054832~db=all~order=page.
93. U. Pöschl, Y. Rudich and M. Ammann. Kinetic model framework for aerosol and cloud surface chemistry and gas-particle interactions — part 1: General equations, parameters, and terminology. *Atmos. Chem. Phys.* **7**(23), 5989–6023 (2007), doi:10.5194/acp-7-5989-2007, http://www.atmos-chem-phys.net/7/5989/2007/.
94. E. R. Trump and N. M. Donahue. Oligomer formation within secondary organic aerosol: Equilibrium and dynamic considerations. *Atmos. Chem. Phys.* **14**, 3691–3701 (2014), doi:10.5194/acp-14-3691-2014, http://www.atmos-chem-phys.net/14/3691/2014/.
95. M. Kalberer, D. Paulsen, M. Sax, M. Steinbacher, J. Dommen, A. S. H. Prevot, R. Fisseha, E. Weingartner, V. Frankevic, R. Zenobi and U. Baltensperger. Identification of polymers as major components of atmospheric organic aerosols. *Science* **303**, 1659 (2004).
96. M. P. Tolocka, M. Jang, J. M. Ginter, F. J. Cox, R. M. Kamens and M. V. Johnston. Formation of oligomers in secondary organic aerosol. *Environ. Sci. Technol.* **38**(5), 1428–1434 (2004), doi:10.1021/es035030r.